ORIENTATION DISTRIBUTION AND TRANSITIONS IN POLYMER-DISPERSED LIQUID CRYSTALLINE DROPLETS

by

RAJESH KUMAR GOYAL

A dissertation submitted to the Graduate Faculty in Engineering in partial fulfillment of the requirements for the degree of Doctor of Philosophy,
The City University of New York

2008

This manuscript has been read and accepted for the Graduate Faculty in Engineering in satisfaction of the dissertation requirement for the degree of Doctor of Philosophy.

Jan. 25, 2008	Morton M. Denn
Date	Chair of Examining Committee
Jan. 25, 2008	Mumtaz K. Kassir
Date	Executive Officer
	Charles Maldarelli
	Alexander Couzis
	Joel Koplik
	Raymond Tu
	Supervisory Committee

THE CITY UNIVERSITY OF NEW YORK

Abstract

ORIENTATION DISTRIBUTION AND TRANSITIONS IN POLYMER-DISPERSED LIQUID CRYSTALLINE DROPLETS

by

Rajesh K. Goyal

Adviser: Professor Morton M. Denn

Dispersions of liquid crystalline droplets in a polymeric matrix are of interest in a variety of applications, including display technology and the fabrication of self-reinforced composite materials. The material properties, which are affected by the liquid crystalline orientation distribution in the droplet, appear to depend sensitively on the nature of the interface between the liquid crystalline dispersed phase and the isotropic matrix material. The orientation distribution satisfies a minimum free energy condition in a quiescent droplet.

Orientation distributions in droplets of liquid crystals with homeotropic anchoring are computed with a simulated annealing algorithm that minimizes the free energy of the Oseen-Frank continuum theory. A first-order transition between axial and radial conformations at a critical value of a parameter that represents the effect of droplet size and surface and bulk potentials is observed in spherical droplets. A similar transition occurs in a deformed droplet at a critical extension.

The droplets exhibit multiple orientational steady states that are separated by finite energy barriers over the entire range of the dimensionless ratio of

surface to elastic forces, with maximum transition energy densities of the order of 2,000 Pa for a typical liquid crystalline droplet with a spherical radius of 1 micron. The transition energy densities decrease with elongation to spheroidal droplets with aspect ratios of four or more, indicating that droplet elongation is favored to drive surface-induced transitions.

We also compute the surface-induced droplet morphology and the free energy pathway as a cylindrical liquid crystalline filament with preferred homeotropic interface orientation passes through a sequence of sinusoidal perturbations and breaks up into droplets. A first-order morphological transition with a finite energy barrier of the order of 2,400 J/m^3 (Pa) for an equivalent droplet with a radius of 1μm is required when the perturbation amplitude exceeds a critical value. This result is consistent with a kinetic trapping explanation proposed by Inn and Denn [J. Rheology, 49, 887-895 (2005)] for a delayed transition from a gel to a dispersed droplet morphology in blends of 4'-octyl-4-biphenylcarbonitrile (*8CB*) and poly(dimethyl siloxane).

To

Maa Saraswati

Acknowledgments

My PhD in the City University of New York has been a long journey and there were many people who helped me, inspired me and provided support throughout this journey. Here, I take this opportunity to thank all those people to make my thesis work productive and successful. First, I would like to express my sincere appreciation and gratitude to my mentor Prof. Morton Denn for his continuous guidance, support and motivation. His immense knowledge of the subject, excellent scientific approach to problems, great work ethics and patience has inspired me becoming a true researcher. Once in a research conference a very well known scientist approached me and said, “Oh, so you work with Mort, tell me about your project.” Now and then I hear those things about him and it makes me very proud of being his student. I wish I also made him proud of being my mentor.

I gratefully acknowledge help from Dr. Xianfeng Li in the initial phase of my thesis. His efficient and user-friendly Monte Carlo Code helped me enormously in continuing my thesis work in a very smooth fashion.

I am indebted to Profs. Charles Maldarelli and Joel Koplik for their invaluable suggestions and guidance many times during my thesis. I am also grateful to them along with Profs. Alexander Couzis and Raymond Tu for accepting my request to be members of the examining committee and for providing suggestions and improvements to my thesis.

The role of Chemical Engineering and Levich Institute members has been extraordinary. I thank them for letting me use their facilities and for fruitful discussions

and suggestions. Special thanks to Andy, Xu, Igor, Junjun, Mary, and Lisa, without them this work would have not been possible.

I would like to thank National Science of Foundation and Petroleum Engineering fund for sponsoring this project.

I gratefully acknowledge support from my group members John, Fang, Pradeep, Yangwoo, and Phillip. I owe them a lot, especially to John who was also my roommate for about two years. I am also indebted to Ashish, Nikhil, and Vivek for being my roommates and supporting me during my PhD. Special thanks to Sandeep, Amar, Pandurang and Vikas for giving me a place to stay when I needed it the most. Help from Anil Kumar is greatly appreciated; there were times when he spent hours to find solutions to my personal and research problems. Raxit, Ravi and Athar thanks a lot for being there whenever I needed you the most; you helped me making my dreams true.

What can I be without support from my family? It is impossible for me to describe in words what my family has done for me throughout my life. Whatever I am, I am because of my parents' unconditional love, faith and sacrifice and my siblings' understanding and support. Words fail to express my appreciation to Ishu who gave me a new motivation to life and whose endless love never let me give up and encouraged me facing the very challenging problems of life.

Preface

Multiphase systems containing liquid crystalline dispersed phases are of interest for a variety of technological applications. Low molar mass liquid crystals are essential components in display technology. Dispersed polymeric liquid crystals are employed in barrier films and self-reinforced composites, and they are effective in very small concentrations as processing aids for flexible thermoplastics. Blends in which the dispersed phase is a polymer with side-chain liquid crystallinity are of interest for electrorheological applications. The functional properties of these multiphase systems often depend on the liquid crystalline orientation distribution in the droplet, which is determined by a balance between the bulk nematic potential, which favors alignment, and the surface potential, which often favors a homeotropic orientation. The orientation distribution satisfies a minimum free energy condition in a quiescent droplet.

Multiple locally stable states can exist in liquid crystalline dispersions. Inn and Denn [J. Rheology, 49, 887-895 (2005)] recently observed bistability in a dispersion of the biphenylcarbonitrile 8CB in polydimethylsiloxane, for example, where a bicontinuous gel-like morphology and dispersed droplets with a radial conformation can both exist within the nematic temperature regime. The dispersed droplet morphology appears to be the lower energy state for the nematic, but the gel breaks up into a low-viscosity dispersed droplet system only when the temperature is raised above the nematic-isotropic transition. Inn and Denn have speculated that an extended liquid crystalline structure that creates the gel is kinetically trapped because of a large energy barrier between the extended and spherical states, both with homeotropic orientation. In this thesis, we explore the orientational morphologies of spherical and spheroidal droplets of low molar-

mass liquid crystals using a simulated annealing approach, with particular attention to bistability and the transitions between locally stable states, and the energy barriers for such transitions. Further, we extend this approach to liquid crystalline cylinders and to the development of pathways by which a liquid crystalline cylinder might break up into droplets.

This thesis is organized into four chapters: Chapter 1 provides an introduction to the fundamental properties of liquid crystals and their applications in industry. We focus on nematic liquid crystals in this thesis: We review the theory of the order parameter and the free energy associated with the defects in nematics. We consider the bulk free energy of Frank type, which depends on four elastic constants (splay, k_{11}; twist, k_{22}; bend, k_{33}; and saddle-splay, k_{24}) and surface anchoring energy of Rapini/Papoular type, which depends on the surface anchoring strength W. These parameters, along with the geometry of the nematic droplets, produce different director orientations; a few nematic configurations reported in the literature are discussed later in the chapter. Finally, orientational transitions and bistability in liquid crystalline droplets are reviewed. We analytically calculate the transitions between radial and parallel orientation in spherical droplets and planar-polar and escaped-radial orientations in cylindrical droplets.

In this thesis, we have implemented a simulated annealing technique utilizing the Metropolis algorithm over a spatial discretization of the droplet to calculate the minimum free energy configuration for the director orientation of a nematic liquid crystal subject to variable surface anchoring. Chapter 2 describes our simulation model, discretization scheme, and algorithm. First, we propose a method that allows free choice of the elastic constants in the Frank free energy expression, as well as the surface anchoring strength in

the Rapini/Papoular surface anchoring energy. To conserve the nematic symmetry in the calculations, an algebraically equivalent tensorial expression for the Frank elastic energy is discussed to incorporate the surface constant k_{24}. Then, we discuss our discretization scheme: We implement both forward and backward differences to approximate derivatives and average over two nearest neighbor terms. Finally, our algorithm, observed quantities such as order parameters and energy, and a simulation method to calculate the integrated optical images, are discussed.

We discuss our results in Chapters 3 and 4. In Chapter 3, we discuss the orietational morphologies in spherical and spheroidal droplets with particular attention to bistability and the transitions between locally stable states, and the energy barriers for such transitions. There is convergence of the algorithm with respect to the number of computational cells. A first-order transition from an axial conformation to a radial conformation is observed in a spherical droplet of radius R for equal bulk constants (k_{11}= k_{22}= k_{33}), when the dimensionless anchoring strength parameter $WR/(2k_{11}- k_{24})$ exceeds a value of 5.9. The transition is broader if the Frank elastic coefficients are unequal, and the parallel and radial order before and after the transition is less perfect because of the presence of twist distortions when $k_{22}/k_{11} < 1$. We also discuss results for spheroidal droplets in the same chapter. The transition is sharp for small values of the deformation parameter, D, but it becomes gradual for large extensions. This is because the orientation distribution in a highly elongated droplet with strong homeotropic anchoring is nearly parallel over a large fraction of the droplet volume. Multiple steady states that are separated by finite energy barriers exist for spherical and spheroidal droplets over the entire range of the dimensionless ratio of surface to elastic forces, with maximum

transition energy densities of the order of 2,000 J/m^3 (Pa) for a typical liquid crystalline droplet with a spherical radius of 1μm. The transition energy density decreases with elongation to aspect ratios of four or more.

In Chapter 4, we first discuss orientational distribution and transition results for nematic cylinders. We also discuss the development of pathways by which a liquid crystalline cylinder might break up into droplets. There is a first order transformation in circular cylinders between planar-polar and escaped-radial conformations at a critical value of the parameter WR/K (R is the radius of cylinder and $k_{11}= k_{22}= k_{33}= k_{24}=K$). Different configurations are obtained inside cylinders, depending on the wavelength of perturbation, λ, the perturbation amplitude, b, the elastic constants and the surface parameter. Later in Chapter 4, we compute the free energy pathway as a cylindrical filament passes through a sequence of sinusoidal perturbations and breaks up into droplets. We find that the energy of cylinders with long wavelength disturbances decreases with increasing perturbation amplitude, b and is lowest for the equivalent sphere. Hence, disturbances for large wavelength cylinders should grow, and this quasi-equilibrium pathway is a feasible one for nematic filaments to break up into droplets. It is necessary for the system to undergo a morphological transition to follow this pathway, however, and a first-order transition with a finite energy barrier of the order of 2,400 J/m^3 (Pa) for an equivalent droplet with a radius of 1μm is required when the perturbation amplitude exceeds a critical value.

Contents

List of Tables

List of Figures

Chapter 1
Introduction

1.1 Introduction to the Liquid Crystalline Phase

Matter can exist in different stable phases (typically solid phase, liquid phase and gas phase) under different thermodynamic conditions [1-4]. These phases differ from each other by their molecular arrangement. The molecular interactions determine the possible configurations of the given system, and a material state is described with two parameters, orientational order and positional order. In crystalline solids, molecules are located in fixed positions relative to each other, and usually adopt a fixed orientation and position. Thus, the crystalline solid phase has well-defined positional and orientational order. The physical properties observed in different directions may differ in solids and, thus, crystalline solids may be anisotropic. In a liquid or gas phase, molecules are neither oriented in a specific direction nor occupy a specific position. Thus, these phases do not have any positional order or orientational order. Also the physical properties in a liquid or gas phase are independent of the directions of the observation, hence the gaseous or liquid states are isotropic or disordered states.

Most compounds exhibit a solid, liquid or gas state under different thermodynamic conditions. There are compounds that also exhibit an intermediate state

between solid and liquid. These intermediate states may have both isotropic properties of liquids and anisotropic properties of solids. Liquid crystals [1-7] have such intermediate order. The molecules in the liquid crystal phase are free to move in random fashion but they tend to remain directionally oriented. Thus, this phase may have both partial positional and orientational order. Fig 1.1 illustrates the order present in the crystalline solid, liquid crystal and liquid phase. Liquid crystals have some properties similar to isotropic liquids, such as flow properties and densities, and some properties similar to solids, such as x-ray diffraction, long-range order, and scattering of visible light.

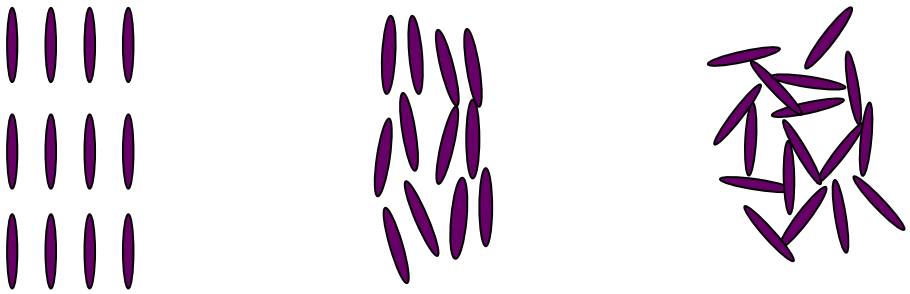

(a) (b) (c)

Fig 1.1: Arrangement of molecules in various phases: Crystalline solid (a), liquid crystal (b), and liquid (c).

Liquid crystalline phases are generally formed by rigid rod-like or disc-like organic molecules (also called mesogens). Rigidity is accomplished by the interconnection of two rigid cyclic units with connection at the para position or by linking units containing multiple bonds, such as -(CH=N)-, -N=N-, -(CH=CH)-, -CH=N-N=CH-. A typical example of a rod-like low molecular mass liquid crystal, *p*-azoxynisole (PAA), is shown in Fig 1.2.

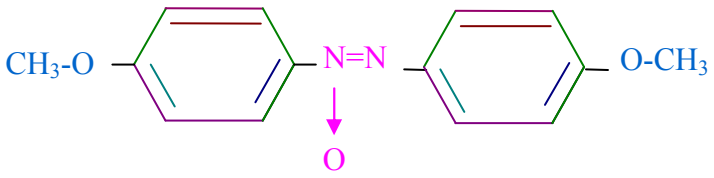

Fig 1.2: Structure of a low molar mass liquid crystal, *p*-azoxyanisole (PAA).

A liquid crystal phase may be obtained by purely thermal processes or by the influence of solvents. Thermotropic liquid crystal phases are induced by changing the temperature; PAA is a typical thermotropic liquid crystal. When liquid crystal phases are obtained by dissolving a sufficient number of molecules in a solvent, the substances are referred to as lyotropic liquid crystals. These phases are formed by amphiphilic molecules. In this thesis, we limit our discussion to thermotropic liquid crystals only.

1.1.1 Classification of liquid crystals

Depending on the molecular structure, a compound may exhibit one or more liquid crystalline phases. Friedel [8] classified liquid crystalline phases in 1922 based on their symmetry and order, as follows:

Nematic phases

The nematic phase is the simplest liquid crystalline phase. The word *nematic* comes from the Greek *νημα*, meaning thread [4], because thread-like defects are typically observed in nematics. Fig. 1.3 shows two different kinds of nematic phases (uniaxial and biaxial).

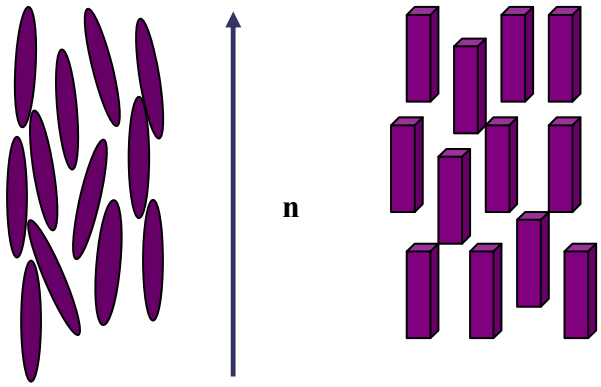

Fig 1.3: Nematic liquid crystal phases: Uniaxial (a) and biaxial.

The nematic phase has the following main features:

- There is no positional order, since the centers of gravity of the molecules do not have any long-range order.
- There is directional order, and the molecules prefer to be parallel to some common axis, called the *director* and denoted by a unit vector **n**. In a uniaxial nematic phase, there is a complete rotational symmetry around the axis **n**.
- The states of the director **n** and **-n** are indistinguishable. Thus, there is no polarity in the system, though individual molecules can be polar.
- Nematic phases can occur only with achiral compounds, or with a racemic mixture of left-handed and right-handed chiral species.

Smectic phases

Smectic liquid crystals are layered structures with a well-defined spacing, and therefore have partial orientational order as well as partial positional order. The word smectic comes from the Greek $\sigma\mu\eta\gamma\mu\alpha$, which means soap. If a compound shows

smectic and nematic phases, then the smectic always occurs at temperature below the nematic domain. Depending on the manner of layer formation and the existing order insider the layers, smectic phase can be further classified; a schematic representation of smectic A and smectic C phases is shown in Fig 1.4.

(a) (b)

Fig 1.4: Two types of smectic phases: Smectic A (a) and smectic C (b).

Cholestric or helical liquid crystal phases

The cholestric (or chiral nematic, or helical) liquid crystal phase is typically composed of nematic mesogenic molecules containing a chiral center. Locally, a cholestric is very much like a nematic**;** on a larger scale, however, the cholestric director **n** follows a helical form. A typical representation of the cholestric phase is shown in Fig 1.5.

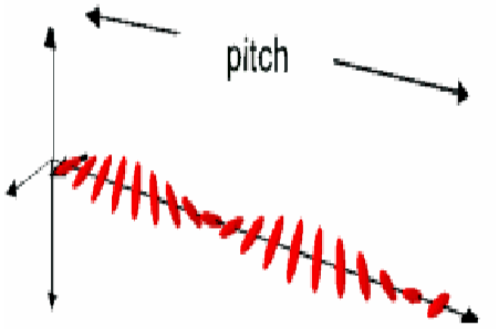

Fig 1.5: The arrangement of molecules in the cholestric phase. Image adapted from http://plc.cwru.edu/tutorial/enhanced/files/textbook.htm.

Liquid crystalline polymers (LCPs)

Polymer liquid crystals [7] are a class of materials that combine properties of polymers with liquid crystals. In LCPs, rod-like or disc-like elements (mesogens) are incorporated into polymeric chains. Depending on the structure of the polymeric compound, they are classified into two categories. Main-chain polymer liquid crystals are formed when the mesogens are themselves part of the main chain of a polymer. If mesogens are connected as side chains to the polymer by a flexible bridge, a side chain polymer liquid crystal is formed. The type of LCP is determined by the mesogen attached to the chain.

1.1.2 Liquid crystal applications

Today, liquid crystals have variety of applications. A few liquid crystal applications are discussed below:

LC displays

The most common application of liquid crystal technology is in liquid crystal displays (LCDs) [5,9]. In a typical device, a layer of a helical liquid crystalline material is placed between two crossed-polarizers. In the absence of an electric field, this helical phase reorients light that has passed through the first polarizer, allowing it to be transmitted through the second polarizer and reflected back to the observer. The device thus appears clear. When an electric field is applied to the LC layer, the aligning stress is sufficient to remove the twist and all the molecules come to the aligned state. In this aligned state, the molecules do not reorient light, so the light polarized at the first polarizer is absorbed at the second polarizer and the entire device appears dark. Hence, the electric field can be used to make a pixel switch between clear or dark on command. The same technique is used to make color LCD systems, with color filters used to generate pixels of different color. Similar principles can be used to make other liquid crystal-based optical devices.

High strength fibers

Polymer liquid crystals are used in variety of technological applications because of their unique properties. In particular, they are chemically highly inert and highly resistant to heat. Typically, they are used in manufacturing of food containers, appliances, automotive applications, electronics etc. Kevlar, a high strength fiber, is one example of the use of polymer liquid crystals; it is used in helmets and bulletproof vests. Dispersed polymeric liquid crystals are employed in barrier films and self-reinforced composites,

and they are effective in very small concentrations as processing aids for flexible thermoplastics.

Liquid crystals have a multitude of other uses. They are used in optical imaging and recording. They are also used for nondestructive mechanical testing of materials under stress and in various medical applications. The pitch of a cholestric depends on the temperature. Since color of the material changes with pitch, changing temperature will produce different colors. This leads to a number of applications, including liquid crystal thermometers, detection of hot points in microcircuits, localization of fractures and tumors in humans, conversion of infrared images, etc. Blends in which the dispersed phase is a polymer with side-chain liquid crystallinity are of interest for electrorheological applications.

1.1.3 Birefringence in liquid crystals

Liquid crystals are birefringent due to their anisotropic nature [1]. Light polarized parallel to the director travels at a different velocity than light polarized perpendicular to the director; i.e. the index of refraction is different in the two directions.

1.2 Fundamental Parameters in Liquid Crystalline Phases

1.2.1 Order parameter

An order parameter is defined to measure the order in a liquid crystal [1,2,4,5]; the order parameter is non-zero in an anisotropic phase and vanishes in an isotropic fluid because of symmetry. This section describes the orientational order parameter of the nematic phase.

Anisotropic properties of a liquid crystal phase are characterized by means of a second-order tensor Q [4]. The tensor Q is real, symmetric and traceless. If the nematic phase is biaxial then all three eigenvalues of the order tensor are different, while if it is uniaxial then two eigenvalues are the same. For a uniaxial nematic, Q can be written as

$$Q_{\alpha\beta} = S[n_\alpha n_\beta - \frac{1}{3}\delta_{\alpha\beta}] \tag{1.1}$$

where the unit vector **n** is the director, $\alpha, \beta = x, y, z$ and $\delta_{\alpha\beta}$ is Kronecker's delta. The scalar order parameter S of the system is defined as

$$S = < P_2(\mathbf{n}.\mathbf{u}) > \tag{1.2}$$

or, $$S = \frac{1}{2} < (3\cos^2\theta - 1) > \tag{1.3}$$

where **u** is the molecular axis and θ is the angle between the molecular axis and the director **n**. $P_2(x)$ is the second order Legendre Polynomial. The angular brackets $<>$ denote the average over all molecules. The order parameter S is defined in a way that its value is unity when the phase is perfectly ordered. In the isotropic phase molecular orientations are disordered, so $\cos^2\theta = 1/3$ and S=0. At the low temperature end of the nematic range, S generally takes a value of about 0.7-0.8. As the temperature is raised it falls to a value of about 0.3-0.4 just above the nematic-isotropic (*N-I*) transition. It then drops discontinuously to zero at the transition. A typical plot of order parameter with temperature is shown in Fig 1.6.

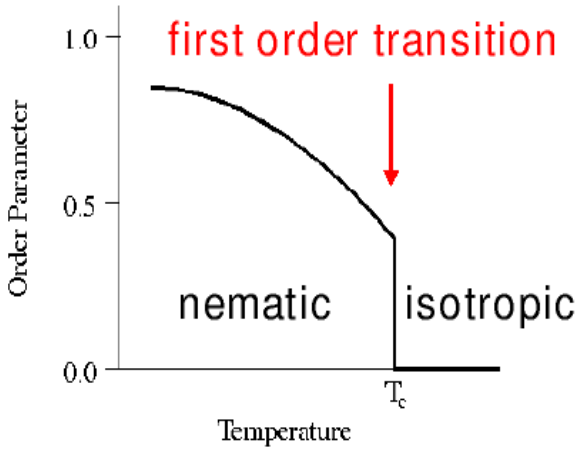

Fig 1.6: Typical temperature dependence of the nematic order parameter.

1.2.2 Elastic properties of nematics

In an ideal nematic phase, molecules are aligned on average along the orientation of the director and the order parameter is uniform in space. However, when external fields are applied or the surface of the sample is given a special treatment, multiple distortions are introduced and the order parameter no longer remains spatially invariant. Oseen [10] and Zocher [11] proposed a theory to calculate the free energy associated with the deformation. They considered the variations of the director orientation to be on a scale much larger than the molecular dimension and treated the nematic medium as a continuum. This way, the deformation can be described by continuum theory, disregarding the details of the structure on the molecular scale. The distorted state may then be described entirely in terms of the director field $\mathbf{n}(\mathbf{r})$. The local director $\mathbf{n}(\mathbf{r})$ is of unit length but of variable orientation. Due to variations in the director field, the nematic phase gains free energy relative to a uniform phase, which is characterized by a uniform

director field, or $\nabla \mathbf{n} = 0$. Oseen and Zocher considered the free energy density of the distorted state at any point as functions of the director and its gradient at that point. Later, Frank [12] modified the expression for free energy associated with the distortion by taking the free energy function to be quadratic in the gradients of the director.

The general expression for the Frank elastic energy density (energy per unit volume) is given by:

$$f = \frac{1}{2}\left[k_{11}(\nabla.\mathbf{n})^2 + k_{22}(\mathbf{n}.\nabla\times\mathbf{n})^2 + k_{33}(\mathbf{n}\times\nabla\times\mathbf{n})^2 - k_{24}\nabla.(\mathbf{n}\times\nabla\times\mathbf{n} - \mathbf{n}(\nabla.\mathbf{n}))\right] \qquad (1.4)$$

Here, parameters k_{11}, k_{22}, k_{33}, and k_{24} are called Frank constants and known as splay, twist, bend and saddle-splay constants, respectively. A mixed-splay-bend term with an elastic coefficient k_{13} is usually neglected because it involves higher-order derivatives of the director field. Each of the terms in the energy expression has its own physical significance. Fig 1.7 shows the characteristic deformations of the director field corresponding to each constant separately. The splay and bend distortions can be viewed, as part of a source or vortex field, respectively. In the twist deformation the director rotates about an axis perpendicular to itself. Since a uniform director field configuration represents a state of minimum energy, and since it is possible to generate deformations that are pure splay, pure twist, or pure band, the corresponding elastic constants must always be positive. For low molar mass nematics, the constants are in the order $k_{33} \geq k_{11} > k_{22}$ [4,13-16]. In liquid crystal polymers, the splay constant k_{11} is much larger than the other two constants [17].

The constant k_{24} is also known as the surface elastic constant. Since the term associated with k_{24} is a pure divergence term, it can be transformed into a surface integral over all surfaces of the system:

$$E_{24} = -\frac{1}{2} k_{24} \int_A d\mathbf{A}.(\mathbf{n} \times \nabla \times \mathbf{n} - \mathbf{n}(\nabla.\mathbf{n})) \tag{1.5}$$

The contribution from the saddle-splay term is zero if **n** is either constant in a plane or parallel to a plane. This term is often neglected in calculating the director configuration. While the term affects the stability of different director configurations relative to each other, it is generally assumed that it does not significantly influence the director pattern. Saddle-splay effects have been discussed broadly in Crawford and Žumer [18].

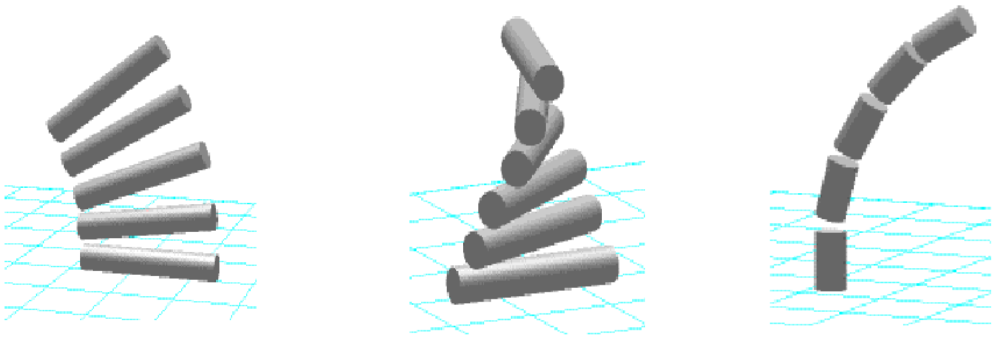

(a) (b) (c)

Fig 1.7: Illustration of characteristic deformations in a liquid crystal: Splay (a), twist (b), and bend deformation (c).

The elastic constants are strong functions of temperature, and their values decrease when temperature is increased, although the ratios are insensitive to temperature [19]. Both experimental [13,14,20] and theoretical methods [4,21] have been employed to determine elastic constants. With the Frederiks transition method [20], a liquid crystal sample is placed between two parallel plates having different surface alignment properties and a magnetic field is applied normal to the preferred orientation. Measurement of the critical magnetic field strength required for transition and its comparison with the theoretical values for different cases provided a method to measure

the elastic constants. For 5CB (4'-pentyl-4-biphenylcarbonitrile), for example, values of $k_{33}/k_{11} = 1.4$ and $k_{22}/k_{11} = 0.66$ [13], $k_{33}/k_{11} = 1.31$ and $k_{22}/k_{11} = 0.51$ [15], and $k_{33}/k_{11} = 1.6$ and $k_{22}/k_{11} = 0.48$ [16] have been reported.

Data for k_{24} are quite limited: Polak and co-workers [13] estimate $k_{24}/k_{11} \sim 3.1$ for 5CB using an optical method, but various bounding estimates would result in $1.2 > k_{24}/k_{11} > 0.9$. The upper bound is derived from an inequality by Ericksen [22] that requires that k_{24} be less than twice the smaller of k_{11} or k_{22}. The Ericksen inequality is violated by the result obtained from the optical measurements in [13]. The Cauchy relation $k_{24} = \frac{1}{2}(k_{11} + k_{22})$ [23] is often assumed, and this relation is roughly consistent with ^{2}H-NMR measurements summarized by Crawford and Žumer [18] for a deuterated 5CB.

In the one constant approximation, $k_{11} = k_{22} = k_{33} = k_{24} \equiv K$, the Frank elastic energy (Eq. 1.4) takes the following form:

$$f = \tfrac{1}{2} K (\nabla \mathbf{n}) : (\nabla \mathbf{n})^{\mathrm{T}} \tag{1.6}$$

This expression is often used to obtain a basic understanding of a system without dealing with effects of unequal elastic constants.

1.2.3 Surface anchoring energy

When a liquid crystal is confined to small cavities, for example when a liquid crystal compound is dispersed into any isotropic or anisotropic material, the orientation of the liquid crystal changes near the surface. The knowledge of these orientation changes is of interest both from a fundamental point of view and for technological applications [24]. Depending on the nature of the surface, the liquid crystal director typically possesses a preferred orientation with respect to the surface, and this effect is called

surface anchoring. The special cases where the director **n** is perpendicular and parallel to the surface are called *homeotropic* and *planar* anchoring, respectively. The angle made by the director with the surface is variously called the tilt angle, the pre-tilt angle, the tilt bias angle and the easy angle. Rapini and Papoular [25] first discussed the energy density for anchoring. They treated the surface free energy density of a nematic at an interface with a preferred radial orientation in the following way:

$$f_s = \frac{1}{2} W \sin^2 \varphi \tag{1.7}$$

$$\text{or,} \quad f_s = \frac{1}{2} W [1 - (\mathbf{n}.\mathbf{v})^2] \tag{1.8}$$

Here, φ refers to the angle that the director makes with the preferred orientation **v**. W is the anchoring coefficient, which determines the strength of the anchoring. This is a convenient functional form for the surface free energy, in that it is bounded and approximates a leading order quadratic term for small angles. To determine the contribution of the surface energy to the total energy, expression (1.8) is integrated over the droplet surface. The choice of bulk matrix is the most important factor in determining the preferred orientation and anchoring strength. (For example, if a polymer substrate is the bulk matrix, then the polymer repeating unit, chain length, nature of the end group, etc. determine the anchoring characteristics.) Materials such as polydimethylsiloxane and glycerin containing a small amount of lecithin generally provide an orthogonal orientation at the interface, while materials such as polyvinyl alcohol and glycerol provide parallel alignment at the droplet interface. Temperature also affects the anchoring coefficient [26]. Polak et. al. [13] and Erdmann et. al. [26] have developed methods to measure the anchoring coefficient W in confined geometries. In these studies, deuterium

magnetic resonance spectra were measured for the nematic in spherical [26] or cylindrical cavities [13] and then compared with computer-generated spectra derived from calculated director patterns. These experimental studies reported the anchoring coefficient W to be of the order of 10^{-5}-10^{-4} J/m^2.

From a comparison between the bulk elastic energy and the surface energy, the extrapolation length $\xi=K/W$ is introduced [4]. If surface forces are strong compared to the bulk forces, the orientation of the director field is fixed at the wall and elastic interactions are unable to affect the interaction of the molecules at the surface. With weak anchoring, however, elastic interactions are comparable to the surface energy; as a consequence, the director can deviate from the preferred orientation. The stronger the local elastic energy, the more the director will be tilted away from the preferred orientation.

1.3 Nematic Configuration Within Droplets

Nematic configurations within droplets have been a topic of interest for many years. When liquid crystals are confined to small cavities, various types of defects [14,27] are created, and those defects can affect the ability of a LC droplet to transform from one configuration to another. In this section we will examine some of the configurations adopted by a nematic droplet. First, we will address the factors that determine the director configuration inside the droplet. The most important factors that affect the nematic alignment are alignment properties of the liquid crystal at the surface, shape and size of the cavity containing the liquid crystal, elastic constants of the bulk nematic (Frank energy), and the presence of the external fields [5]. Among all of these factors, the preferred alignment of the nematic director at the surface is the most important. As

discussed earlier, depending on the anchoring strength, the director possesses a fixed or variable orientation at the droplet surface and the configuration inside the LC droplet is then determined by a minimization of the total free energy of the nematic.

Elastic forces within the droplet also influence the director configurations. The relative values of the elastic constants k_{11}, k_{22}, k_{33}, and k_{24} produce different orientations of the director field inside the droplet.

The geometry of the cavity affects the droplet configuration significantly. For highly symmetric cavities, the nematic configuration is usually isomorphic to that found in spherical cavities. Multiple defects may exist in large droplets.

External fields also can force the droplet configuration to change from one form to another, but this thesis is limited to the effects of the first three factors.

1.3.1 Configurations adopted by spherical droplets

Orthogonal wall alignment

Possible configurations of nematic droplets with orthogonal wall alignment are radial, twisted radial, axial or equatorial, and escaped radial configurations. Among these, radial and axial are the most common configurations.

The radial configuration is formed when the director field is strongly anchored perpendicular to the surface. This structure possesses spherical symmetry, and there is a point defect at the center of the droplet [Fig. 1.8a]. The only deformation present in the structure is a splay deformation. One method to obtain this structure is by dispersing a liquid crystal into polydimethylsiloxane. The axial configuration possesses a cylindrical symmetry, with a line defect that runs around the equator of the spherical droplet [Fig. 1.8b]. The axial configuration was first identified by Candau et. al. [28] through

application of a strong magnetic field to radial droplets. The size of the droplet is a factor that determines the stability of structures, with smaller droplets favoring the axial structure [26]. In smaller droplets the importance of weak anchoring becomes more pronounced, which leads to stabilization of the axial configuration.

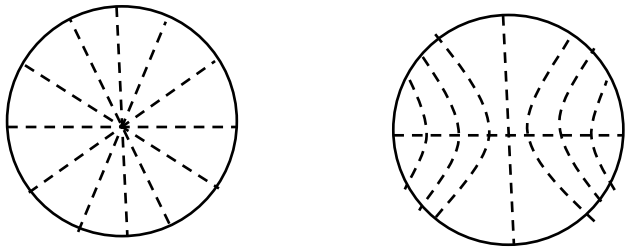

(a) (b)

Fig 1.8: Director configurations in nematic droplets with the orthogonal anchoring: Radial configuration (a) and axial configuration (b).

Parallel wall alignment

Possible configurations with parallel wall alignment are bipolar, concentric, and twisted bipolar configurations. Among these, the bipolar alignment is the most common droplet alignment with parallel alignment. In this configuration, there are two point defects in the droplet, which lie at opposite ends of the droplet [Fig 1.9a], and the line joining those points is called the symmetry axis. The director field is symmetrical about this axis. A bend deformation is the major deformation present in bipolar droplets. Some splay deformation is also present in the structure near the poles. For spherical droplets, the symmetry axis can have any alignment, since all the orientations are equal in the energy, while for non-spherical cavities the symmetry axis lies along the longest distance available within the droplet. For example, for a spheroidal droplet the symmetry axis

aligns along the major axis. Weak anchoring can have an important effect on the droplet configuration. For sufficiently small anchoring strength the surface defects near the poles can be made diffuse or disappear; see Fig 1.9b. Nematic droplets with a bipolar structure were first reported by Meyer [29].

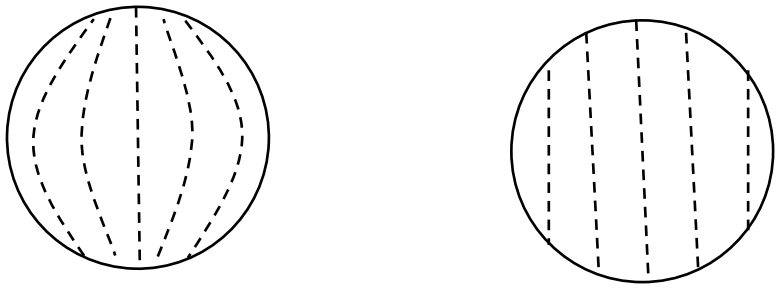

(a) (b)

Fig. 1.9: Schematic of a bipolar droplet with strong (a) and weak (b) parallel anchoring cases.

1.3.2 Configuration within cylindrical cavities

Cylindrical structures have a higher symmetry than spherical droplets. We will discuss structures that are stable for homeotropic anchoring conditions. Four commonly observed structures in cylinders cavities are planar-radial (*PR*), escape-radial (*ER*), planar-polar (*PP*), and planar-polar with two line defects (*PPPD*). Details about these structures can be found in [18], and we will limit our discussion to first three.

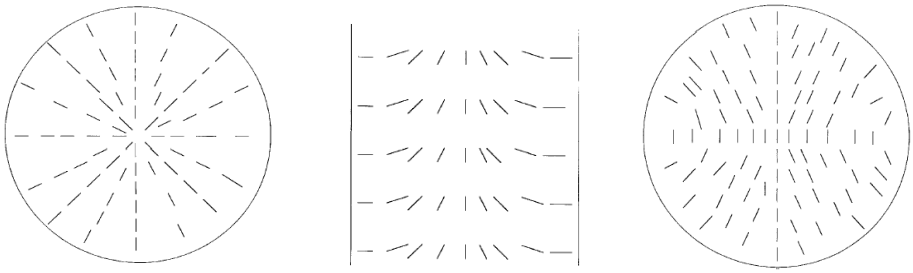

(a) (b) (c)

Fig 1.10: Director configurations with the orthogonal anchoring in cylindrical geometry: Planar-radial (a) escape-radial (b), and planar-polar (c).

The PR configuration consists of only a radial component of the director, with a line disclination along the cylinder axis. Splay is the only deformation present in the configuration, but it is energetically very expensive because of the line defect at the center [Fig. 1.10a]. The ER structure is an extended form of the PR structure, where the high cost of the splay deformation in the center is relieved by introducing a finite amount of bend deformation. In the ER structure, the director is planar radial near the boundary but escapes into the third dimension along the cylinder axis [Fig. 1.10b]. In the PP configuration, the director lies in a plane perpendicular to the cylinder-axis. The local director is uniform near the cylinder-axis while it is radial at the boundary [Fig. 1.10c].

1.4 Orientation transitions and bi-stability in dispersed liquid crystalline droplets

As discussed earlier, the droplet configuration is determined by several parameters, including shape and size of the droplet, elastic constants, anchoring

coefficient, etc. The droplet orientation can be manipulated by introducing external parameters such as temperature, electric fields and magnetic fields. Variation in these parameters causes instability in the droplet configuration and thus leads to transformation to a more stable configuration. These transitions in configurations can provide information on various physical parameters that are used to describe the liquid crystalline state. For example, the Frederiks transition method is used to measure bulk elastic constants [20]. Polak and co-workers measured the saddle-splay and anchoring coefficients using transitions [13]. In other studies, Heppenstall-Butler et. al. [30] and Tixier et. al. [31] attribute different coalescence properties of small and large nematic droplets to a structural transition between radial and axial configuration. They proposed that nematic droplets (dispersed in water) below a characteristic size ($R^*=K/W$) coalescence freely, while droplets with $R>R^*$ show a high-energy barrier for coalescence.

Candau and co-workers observed a radial-axial configuration transition by applying a magnetic field to radial droplets suspended in a mixture of glycerol, polyethylene glycol and water [28]. Variations in surface anchoring density also can be used to transform one structure to another [26]. Another common example of a transition is bipolar-radial, which was observed by Volovik and Lavrentovich (reference in [5]). A detailed study of droplet configurations and transitions can be found in Drzaic [5].

Inn and Denn [32] recently observed multiple locally stable states in a dispersion of 4'-octyl-4-biphenylcarbonitrile (8CB, molecular structure shown in Fig 1.11) into polydimethylsiloxane (PDMS, an isotropic polymer).

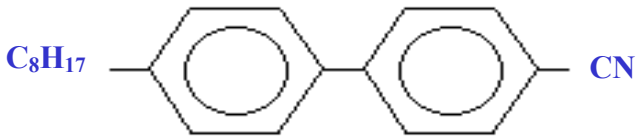

Fig 1.11: Molecular structure of 4'-octyl-4-biphenylcarbonitrile (8CB) liquid crystal.

8CB is a low molar mass liquid crystal, which shows different liquid crystalline phases depending on temperature conditions. Rai and Denn [33] conducted dynamic mechanical tests shown in Fig. 1.12 and observed a slow second-order S-I transition at 33°C (slow decrease in viscosity) and a first-order phase transition between N-I at 41°C (viscosity increases discontinuously).

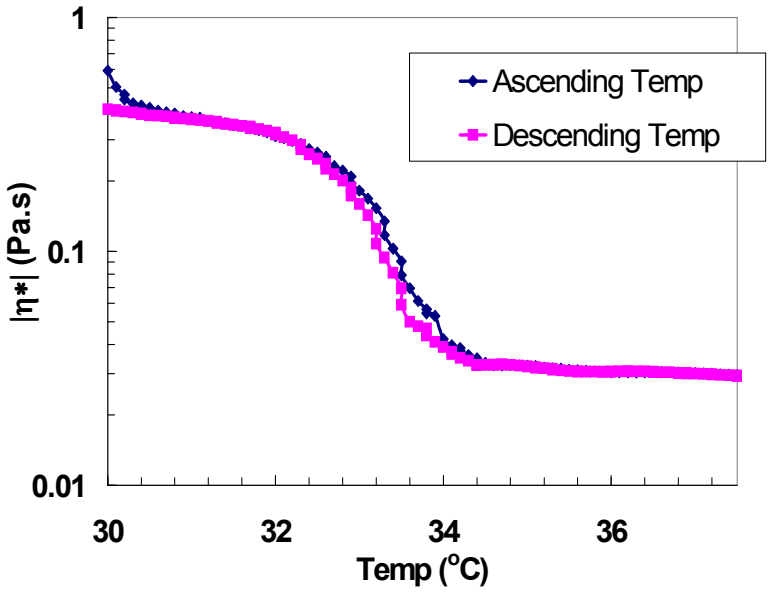

(a)

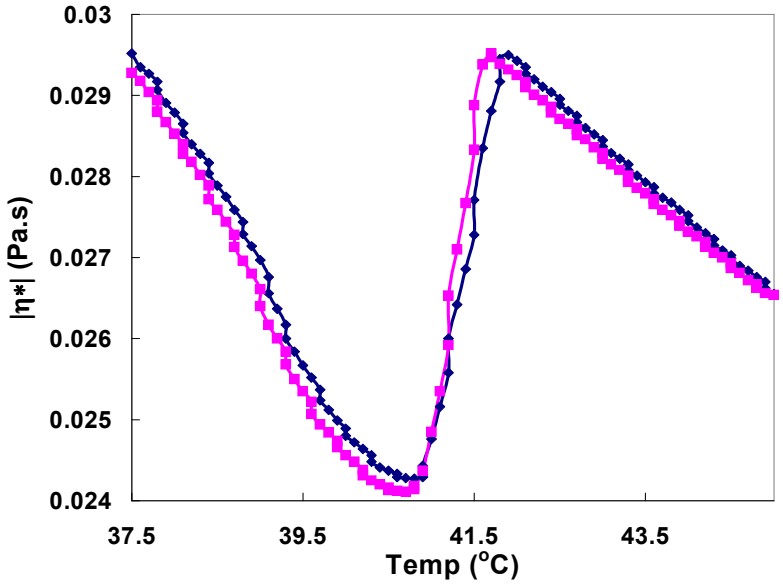

(b)

Fig. 1.12: S-N (a) and N-I (b) phase transition in 8CB [33].

Inn and Denn found that when a dispersion of 8CB is made in PDMS under smectic temperature conditions, a thick bicontinuous gel morphology is the equilibrium state (elastic modulus, G' >> viscous modulus, G''). Similarly, nematic temperature conditions produced a fluid-like state with dispersed droplets with a radial conformation (G'<G'') and isotropic temperature conditions lead to a fluid-like state with no structure inside the droplets. The optical images of these dispersions are shown in Figs 1.13. When they conducted rheological experiments (temperature sweep test) with the dispersion, the system exhibited multiple states. Starting from the smectic temperature regime (where the gel structure is the equilibrium state), and increasing the temperature to the nematic regime, the rheological properties of the dispersion were essentially the same as those of

the gel-like state. They did not observe a fluid-like state until the temperature was increased to the isotropic temperature, where the gel-like state suddenly collapsed into dispersed droplets [Fig 1.14]. Similarly, while conducting a reverse experiment, i.e., starting with the fluid state (isotropic temperature) and decreasing the temperature slowly, a structure having the rheological properties of dispersed droplets was observed throughout the nematic and smectic temperature regimes. In this case, the gel-like state was never recovered by applying shear rates available in a rheometer. Thus, both gel-like and dispersed morphologies were stable in the nematic and smectic regimes [Fig 1.14].

The gel break-up does not occur at the S-N transition temperature, where the interfacial tension increases. Rather it occurs at the N-I transition, where interfacial tension remains essentially constant. Inn and Denn proposed that there was a very high energy barrier between gel and dispersed morphologies, since both are highly ordered structures. Increasing the temperature to the isotropic state lowers the order present in the system and thus decreases the energy barrier, thus permitting an interfacial tension-driven transition to the lower energy state. Similarly, a gel-like morphology can be obtained from the fluid state in the smectic regime by removing the sample from the rheometer and providing a sufficient amount of mixing.

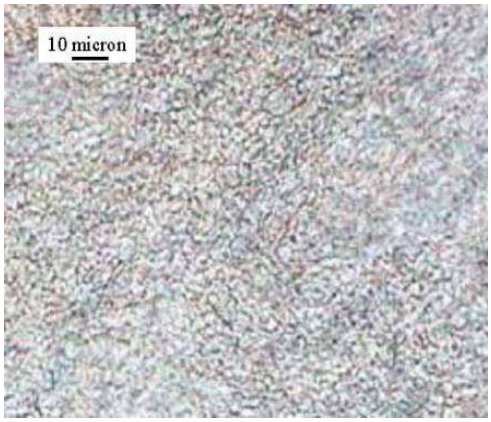

(a)

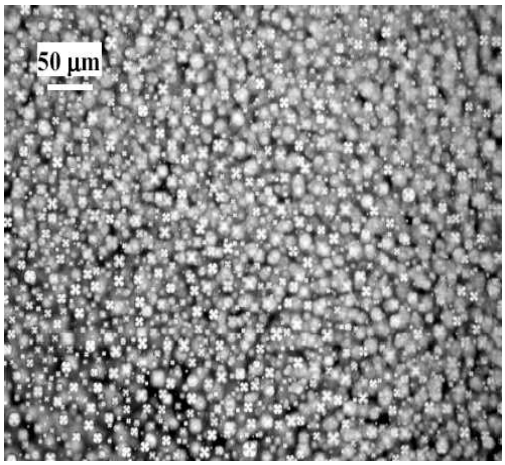

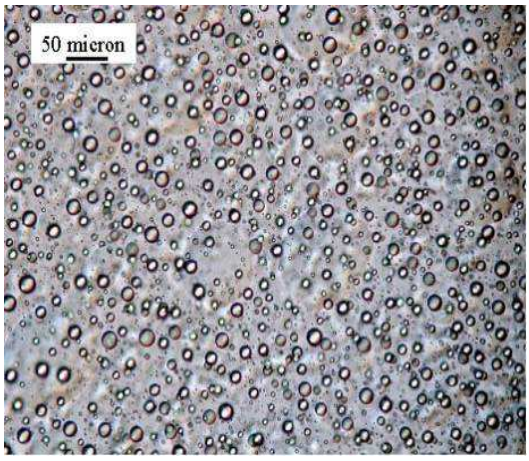

(b) (c)

Fig.1.13: Optical micrographs of dispersion of 8CB into PDMS [32]: Gel-like state in smectic regime (a), fluid-like state in nematic regime (b) and fluid-like state in isotropic regime (c).

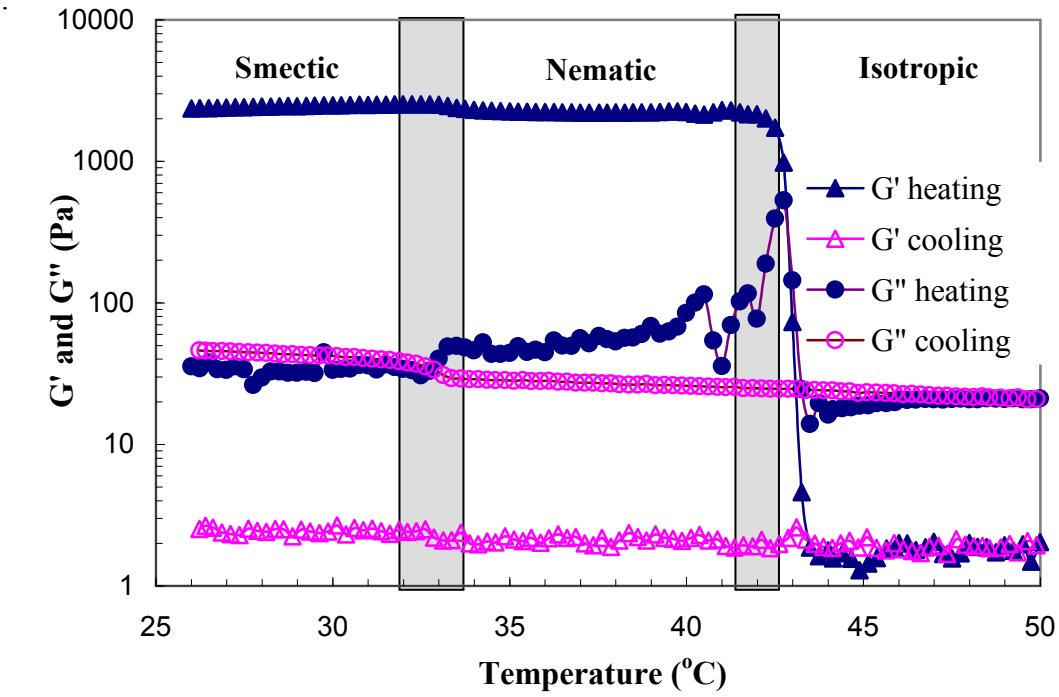

Fig 1.14: Rheological measurements of a dispersion of 8CB in PDMS [32].

In this thesis, we focus on droplet orientations and transitions and the calculation of the energy barriers between orientational states under homeotropic anchoring conditions. The most common transformation found in spherical droplets with this type of anchoring is between radial and axial configurations. In the following paragraph we show the conditions for this transformation in terms of the elastic constants, anchoring strength and droplet radius.

For a sphere of radius *R*, the analytical total free energies for perfectly radial [Fig. 1.8a] and perfectly parallel structures [Fig. 1.9b] are given by:

Radial: $\mathbf{n} = (x,y,z)/(x^2 + y^2 + z^2)^{1/2}$

$$E = 4\pi(2k_{11} - k_{24})R \tag{1.9a}$$

Parallel: $\mathbf{n} = \mathbf{z}$

$$E = \frac{4\pi}{3}WR^2 \tag{1.9b}$$

According to these values, the radial orientation is energetically favored if $WR/(2k_{11} - k_{24}) > 3$ and the parallel orientation is favored if $WR/(2k_{11} - k_{24}) < 3$. Hence, we expect an orientational transition when $WR/(2k_{11} - k_{24})$ is equal to 3. A perfectly radial orientation is possible in principle, but there must be some deviation from a perfectly parallel orientation in the neighborhood of the surface, reducing the surface free energy and introducing a small bulk free energy contribution. Hence, the actual transition between radial and axial structure is expected to occur at a value of $WR/(2k_{11} - k_{24})$ that is greater than 3.

Within cylindrical cavities, the transformation between planar-polar (PP) and escape-radial (ER) structures is the most common. For a cylinder of radius R and length L with $k_{11} = k_{33}$, the free energy calculations have been discussed by Crawford and co-workers [34]. The total energies for PP and ER structures are given by:

$$\text{PP: } E = \pi k_{11} L \left\{ 2 - \left[1 + \frac{1}{4}\left(\frac{WR}{k_{11}}\right)^2 \right]^{1/2} - \ln\left[\frac{4k_{11}}{WR}\left(4\left(\frac{k_{11}}{WR}\right)^2 + 1 \right)^{1/2} - 8\left(\frac{k_{11}}{WR}\right)^2 \right] \right\} \tag{1.10a}$$

$$\text{ER: } E = \begin{cases} \pi k_{11} L\left[3 - \dfrac{k_{24}}{k_{11}} - \left(\dfrac{WR}{k_{11}} + \dfrac{k_{24}}{k_{11}} - 1\right)^{-1}\right], & \dfrac{WR}{k_{11}} > 2 - \dfrac{k_{24}}{k_{11}} \\ \pi RWL, & \dfrac{WR}{k_{11}} < 2 - \dfrac{k_{24}}{k_{11}} \end{cases} \tag{1.10b}$$

The transition between the two structures depends on the value of k_{24}. For k_{24}= k_{11}, the critical value of WR/k_{11} required for transition is about 8.65. Thus, the ER orientation is energetically favored if $WR/k_{11} > 8.65$ and the parallel orientation is favored if $WR/k_{11} < 8.65$.

Chapter 2
Simulation Model and Method

2.1 Overview

In order to understand the macroscopic properties of nematic liquid crystals and to study the stability and conditions for transition between various structures, it is essential to model the orientation inside droplets. Computer simulations are useful tools for understanding the macroscopic properties of liquid crystals and their phase transitions. Simulations of liquid crystals are based on the Monte Carlo and Molecular Dynamics techniques, which are commonly used schemes for fluids [35].

The director configuration is calculated by minimizing the total free energy for given elastic constants and boundary conditions. The total free energy, as discussed in Sec. 1.2, is given by a continuum theory; this is a mean-value theory and, as formulated, has no explicit temperature dependence, although temperature does enter implicitly through the temperature dependence of the elastic parameters. Hence, the theory does not admit thermal fluctuations and cannot predict the N-I phase transition.

Simulated annealing [36-38] is an established methodology for minimizing the free energy. The formalism of simulated annealing is computationally equivalent to a low temperature Monte Carlo technique, which is widely used for simulating the Lebwohl-

Lasher (*LL*) molecular model for liquid crystals [39-47]. The *LL* model is derived from a microscopic approach, wherein liquid crystal molecules placed on a cubic lattice interact through a nearest pair potential of the Maier-Saupe type: $U_{ij} = -\frac{\varepsilon_{ij}(3\cos^2\theta_{ij} - 1)}{2}$. Here ε_{ij} has a constant value ε for nearest molecules *i* and *j* and is zero otherwise, and θ_{ij} is the angle between the axes of the molecules *i* and *j*. The *LL* model has explicit temperature dependence and can be used to investigate properties such as the N-I phase transition and orientational order at the molecular level ([46] and references therein). The essential difference between the two approaches (continuum and *LL* model), despite the computational equivalence, is one of length scale: The *LL* theory is applicable only to the molecular length scale and cannot be used to study the effect of boundary conditions on director configuration in macroscopic objects such as droplets, while the continuum theory applies to length scales much larger than the molecular length. Therefore, the continuum theory must be used to study the director conformation in macroscopic objects. The results of the continuum mean field theory are formally obtained in the limit of zero temperature, for which there are no fluctuations. Monte Carlo calculations using the continuum model have been carried out at zero temperature [36-38] as well as at a low temperature [48-50].

The assumption of equal constants and neglect of the surface terms in the elastic energy expression is quite common in continuum calculations. It is not possible to distinguish between the splay, twist and bend deformations in the single constant approximation, however, and therefore the assumption of equal constants is not appropriate for all cases. In this thesis, we propose a method to study the effect of both equal and unequal elastic constants on droplet orientation. Before describing our method,

we will discuss a few important issues for nematics. First, the director **n** is physically equivalent to **-n** (nematic symmetry), hence, the elastic energy is invariant with respect to changing the sign of the director field. However, the Monte Carlo method requires discretization of the spatial derivatives in the Frank energy expression [Eq. 1.4] and a straightforward discretization can lead to the loss in the nematic symmetry. Different solutions have been proposed to handle this computational problem. Gruhn and Hess [48] used an algebraically equivalent tensorial expression for the elastic energy with three constants (splay, bend and twist) in which nematic symmetry is always preserved with discretization. However, they discarded the saddle-splay term and discussed results with fixed boundary conditions only. Moreover, they considered two-dimensional simulations only, though their work is extendable to three dimensions. Hobdell and Windle [37] carried out three dimensional simulations for the energy with three constants in which the problem of nematic symmetry was avoided with the following algorithm: If two vectors make an angle of more than 90˚ to each other, then one of the vectors is rotated through 180˚ so that the angle is always less than or equal to 90˚. However, this approach still gives a discontinuity in the gradient of the energy function whenever neighboring directors are at 90˚to each other. Also, Hobdell and Windle did not include the effect of the saddle-splay term in their calculations.

As discussed above, Gruhn and Hess and Hobdell and Windle did not consider the effect of saddle-splay constant in energy calculations; however, the saddle-splay term may be of importance in non-planar geometries and when the surface anchoring is weak at the boundary. Kralj and Žumer [51] studied the stability of different structures in nematic droplets with weak homeotropic anchoring at the surface. They started with a

Landau-de Gennes approach ([51] and references therein) for the free energy and then introduced approximations to yield a Frank-type free energy. The basic difference between the two types of free energies is that the free energy is expanded in terms of the derivatives of the components of the nematic director in the Frank approach, while it is expanded in terms of a nematic order parameter and its derivatives in the Landau-de Gennes approach. Kralj and Žumer used the Euler-Lagrange differential equations for the minimization of the director field to discuss the dependencies of the droplet orientation on the ratio of elastic constants k_{33}/k_{11}, k_{24}/k_{11}, anchoring strength and external field, but their discussion was limited to non-twisted cases only (i.e., relatively large k_{22}).

In this work, we employ a Simulated Annealing approach to finding the minimizing vector field **n** in a LC droplet by discretizing the free energy in terms of unit vectors on a lattice and seeking the minimum with a Metropolis Monte Carlo algorithm. To retain the nematic symmetry, we follow the procedure of Gruhn and Hess and propose a general tensorial expression for Frank elastic energy involving all four Frank constants. We also modify their discretization scheme and propose a method to calculate the director field in three-dimensions. The limitation of the algorithm is also discussed [Appendix A], which was absent in Gruhn and Hess's calculations. We show that the scheme is only applicable for ratios of the elastic constants of order unity.

The chapter is organized as follows: First we introduce the general Metropolis Monte Carlo technique. Then we describe our simulation model, discretization scheme and the algorithm. Finally, some of the observed quantities calculated directly in the simulations are described.

2.2 Simulation model

2.2.1 Monte Carlo method

The purpose of the Monte Carlo technique is to calculate the minimum energy state under given thermodynamic conditions by making random changes to the rotation and the translation of the particle [35,52]. A particle is selected at random, and the energy of the configuration E_o is calculated. Now this particle is given a random displacement and the energy of the new configuration E_n is then calculated and compared with E_o**.** If the trial energy E_n is lower than E_o, the trial move is accepted; if it is higher than E_o, then the move is accepted with the probability $p = \exp[-(E_n - E_o)/k_B T]$, where, k_B is the Boltzmann constant and T is the absolute temperature. This process is continued until the equilibrium state is achieved.

2.2.2 Energy calculation

The equilibrium director field **n** in a given geometry follows from a minimization of the total free energy $E = E_b + E_s$ (here E_b is the bulk energy obtained by integrating Eq. 1.4 over the droplet volume and E_s is the surface energy obtained by integrating Eq. 1.7 over the droplet surface.) To minimize the total energy, we require a discretization of the spatial derivatives in the Frank energy expression. To do so, we use a lattice model [Fig. 2.1]; the droplet is circumscribed by a rectangular parallelepiped that is discretized into cubes of equal volume, and the vector field **n** is defined by a discrete value in each element. The centroid of the droplet is located at the intersection of eight central elements (four faces in each coordinate plane), and a cubic element is considered to be contained within the droplet if the centroid of the element lies within the droplet. The curved surface of the droplet can be closely approximated by this method with sufficiently fine

discretization. Only directors in the outermost layer of elements experience the surface potential.

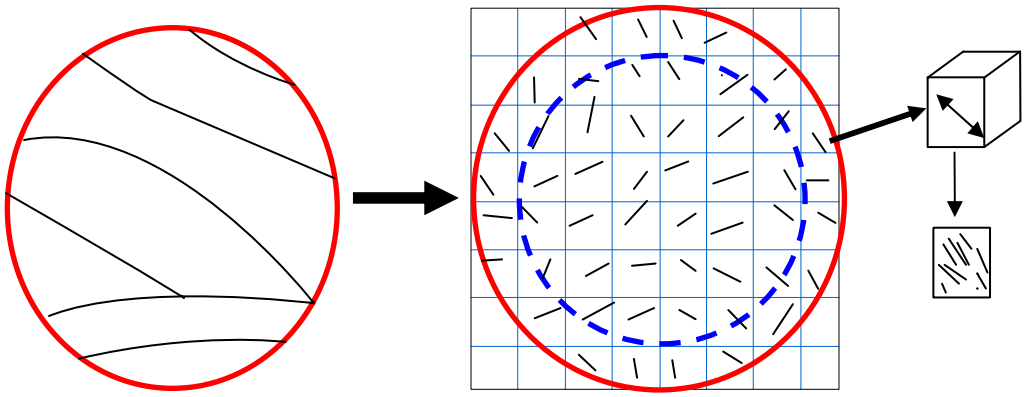

Fig. 2.1: Schematic representation of the lattice model for a spherical droplet. Each cell contains a director, which is the average orientation of the LC molecules within the cell. The bulk directors lie within the spherical boundary made by the continuous line in the rectangle. The surface directors lie within the shell between the continuous and dotted lines.

A straightforward discretization of the free energy density in Eqs (1.4) and (1.7) results in loss of equivalence of **n** and **-n**. To retain nematic symmetry, Eq. (1.4) can be rewritten as

$$f = \tfrac{1}{2}\Big[k_{22}(\nabla\mathbf{n}):(\nabla\mathbf{n})^{\mathrm{T}} + (k_{33}-k_{22})(\mathbf{n}\times\nabla\times\mathbf{n})^2 + (k_{11}-k_{22})(\nabla.\mathbf{n})^2 + (k_{24}-k_{22})((\nabla\mathbf{n}):(\nabla\mathbf{n})^{\mathrm{T}} - (\nabla.\mathbf{n})^2 - (\nabla\times\mathbf{n})^2)\Big], \tag{2.1}$$

which, because of the unit magnitude of **n**, is equivalent to

$$f = \tfrac{1}{2}\Big[\tfrac{1}{2}k_{22}(\nabla_\alpha n_\beta n_\gamma)(\nabla_\alpha n_\beta n_\gamma) + \tfrac{1}{2}(k_{33}-k_{11})(n_\alpha n_\beta)(\nabla_\alpha n_\gamma n_\upsilon)(\nabla_\beta n_\gamma n_\upsilon) + (k_{11}-k_{22})(\nabla_\alpha n_\alpha n_\gamma)(\nabla_\beta n_\beta n_\gamma) + (k_{24}-k_{22})((\nabla_\alpha n_\beta n_\gamma)(\nabla_\beta n_\alpha n_\gamma) - (\nabla_\alpha n_\alpha n_\gamma)(\nabla_\beta n_\beta n_\gamma)\Big]. \tag{2.2}$$

We have used subscript notation and the Einstein summation convention to avoid ambiguity. Eq. (2.2) retains the equivalence of **n** and **-n** following discretization.

2.3 Discretization scheme

Gruhn and Hess proposed implementing both forward and backward differences to approximate derivatives and averaging over eight terms involving nearest neighbors. We find that it is adequate to average over two nearest neighbor terms, as follows: The discretized bulk energy density at each lattice point is

$$f(i,j,k)=\frac{1}{4l^2}\sum_{(r,s,t)\varepsilon[(1,1,1),(-1,-1,-1)]}\Big\{\frac{1}{2}k_{22}\sum_{\beta,\gamma=1}^{3}\sum_{\alpha=1}^{3}(A_{(\alpha\beta\gamma)}^{(r,s,t)})(i,j,k))^2+$$
$$(k_{11}-k_{24})\sum_{\beta=1}^{3}(\sum_{\alpha=1}^{3}A_{(\alpha\alpha\beta)}^{(r,s,t)}(i,j,k))^2+\frac{1}{2}(k_{33}-k_{11})\sum_{\beta,\gamma=1}^{3}(\sum_{\alpha=1}^{3}n_{\alpha}^{(r,s,t)}(i,j,k)A_{(\alpha\beta\gamma)}^{(r,s,t)}(i,j,k))^2+ \quad (2.3)$$
$$(k_{24}-k_{22})(\sum_{\alpha=1}^{3}\sum_{\beta=1}^{3}\sum_{\gamma=1}^{3}A_{(\alpha\beta\gamma)}^{(r,s,t)}A_{(\beta\alpha\gamma)}^{(r,s,t)})\Big\}.$$

Here, l is the lattice spacing and the symbols $A_{(i\beta\gamma)}^{(r,s,t)}$ are defined as

$$\begin{aligned}A_{(1\beta\gamma)}^{(r,s,t)}(0,0,0)&=n_\beta n_\gamma(r,0,0)-n_\beta n_\gamma(0,0,0)\\A_{(2\beta\gamma)}^{(r,s,t)}(0,0,0)&=n_\beta n_\gamma(0,s,0)-n_\beta n_\gamma(0,0,0)\\A_{(3\beta\gamma)}^{(r,s,t)}(0,0,0)&=n_\beta n_\gamma(0,0,t)-n_\beta n_\gamma(0,0,0).\end{aligned} \quad (2.4)$$

The total free energy of the system is then approximated by

$$E=\sum_{\text{All lattices}}f(i,j,k)l^3+\frac{1}{2}\sum_{\text{Surface lattices}}W l^2\sin^2\varphi. \quad (2.5)$$

In the single constant assumption, the total free energy of the system is approximated by

$$E=\frac{K l}{4}\sum_{\text{All lattices}}\sum_{\text{Six NN of (i,j,k)}}[1-(\mathbf{n}(i,j,k).\mathbf{n}(l,m,n))^2]+\frac{1}{2}\sum_{\text{Surface lattices}}Wl^2\sin^2\varphi, \quad (2.6)$$

where (l,m,n) is the nearest neighbor (NN) of (i,j,k).

2.4 Accuracy

We have tested the accuracy of the discretization by entering the analytical director distributions for two defect structures, the hedgehog (radial or noeud, Fig. 2.2a) and col (hyperbolic, Fig 2.2b), respectively, using the discretization to calculate the relative contributions to the bulk free energy densities, which are as follows:

Hedgehog: $\mathbf{n} = (x,y,z)/(x^2 + y^2 + z^2)^{1/2}$

$$E_b = 4\pi R(2k_{11} - k_{24}) \tag{2.7a}$$

Col: $\mathbf{n} = (-x,y,z)/(x^2 + y^2 + z^2)^{1/2}$

$$E_b = 8\pi R(\frac{k_{11}}{5} + \frac{2k_{33}}{15} + \frac{k_{24}}{6}) \tag{2.7b}$$

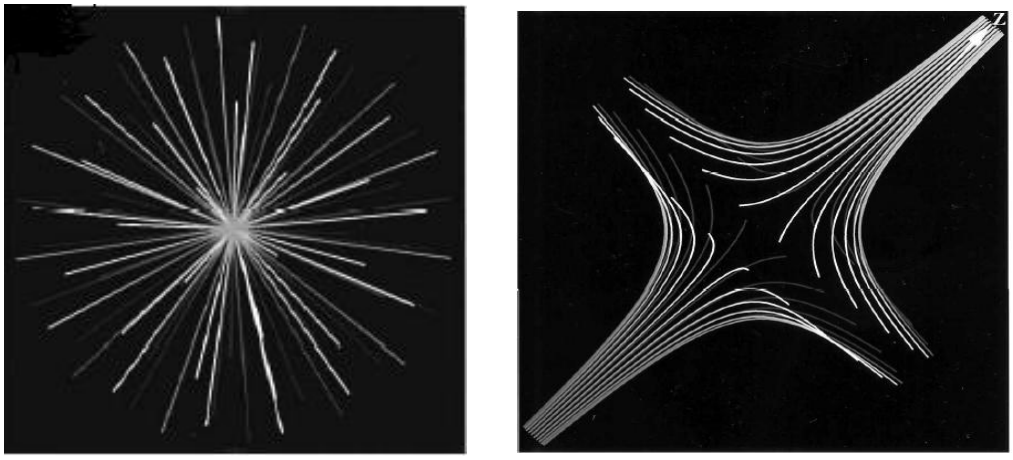

(a) (b)

Fig 2.2: Hedgehog (a) and col point (b) defects. The streamlines in the diagrams follow the director trajectory.

A comparison of the analytical values for the coefficients of the various terms in the free energy densities with computed values using $2x10^5$ lattice cells is shown in Tables 2.1 and 2.2. The computed values using Gruhn and Hess's algorithm are also shown. The computed results are in good agreement with the analytical values, and the two algorithms have comparable accuracy. We assume throughout this study that the center singularity, which is permitted by the Frank formalism, is attainable. In a physical system there is likely to be a small defect core.

Table 2.1: Coefficients of free energy terms of a hedgehog point defect [Eq. (2.7a)] computed using $2x10^5$ lattice cells.

	Analytical	Simulation (Gruhn and Hess's algorithm)	Simulation (this algorithm)
Splay ($\pi k_{11}R$)	8.0000	7.8785	7.8780
Twist ($\pi k_{22}R$)	0.0000	0.0326	0.0323
Bend ($\pi k_{33}R$)	0.0000	0.0204	0.0201
Saddle-splay ($\pi k_{24}R$)	-4.0000	-3.9833	-3.9833
Total	4.0000	3.9482	3.9471

Table 2.2: Coefficients of free energy terms of a col point defect [Eq. (2.7b)] computed using $2\text{x}10^5$ lattice cells.

	Analytical	Simulation (Gruhn and Hess's algorithm)	Simulation (this algorithm)
Splay ($\pi k_{11}R$)	1.6000	1.5716	1.5714
Twist ($\pi k_{22}R$)	0.0000	-0.0078	-0.0090
Bend ($\pi\, k_{33}R$)	1.0667	1.0580	1.0575
Saddle-splay ($\pi\, k_{24}R$)	1.3333	1.3277	1.3277
Total	4.0000	3.9495	3.9476

2.5 Algorithm for free energy minimization

For our lattice model, we apply the Metropolis algorithm to produce a chain of configuration states. The basic simulation procedures can be described briefly as follows:

1 The system is initialized by choosing the vectors $\mathbf{n}(i, j, k)$ randomly, or by choosing a specific distribution (a parallel or radial orientation, for example). The director orientation is described by a unit vector $\mathbf{n}(\sin\theta\cos\phi, \sin\theta\sin\phi, \cos\theta)$, which computationally is achieved by two independent random numbers r_1 and r_2, with even distributions between 0 and 1 ([45] and reference therein), such that $\cos\theta = 1 - 2r_1$, $\phi = 2\pi r_2$.

2 Following initialization, we randomly pick a lattice cell within the droplet, and randomly change the orientation of the local director within the lattice.

3 Changing the orientation of director in any lattice cell affects the free energy density of the system. In this step, we calculate the energy difference ΔE between the configuration with the old local director, $\mathbf{n_o}$ and the new one, $\mathbf{n_n}$. Two cases are considered for the calculation of the energy:

- If the lattice containing the local director does not lie on the surface of the droplet, the energy difference involves only the Frank energy expression. Since a change in the orientation of a lattice director affects the energy in the selected cell and the six nearest neighbors only, for each run we consider the energy difference associated with those seven directors.
- If the lattice cell is a surface cell, then the Rapini-Papoular form of the anchoring energy is also considered.

Since the anchoring energy depends on the angle φ that the director makes with the preferred orientation, we consider an angle φ_s, which is the angle between the local director and the normal line of the droplet surface. For an ellipsoid having axes *a, b,* and *c* and center at (0,0,0), the cosine of the angle φ_s is given by

$$\cos\varphi_s = \frac{1}{d}[\sin\theta\cos\phi(x_s - 0.5)/a^2 + \sin\theta\sin\phi(y_s - 0.5)/b^2 + \cos\theta(z_s - 0.5)/c^2] \tag{2.8a}$$

where $d = \sqrt{(x_s - 0.5)^2/a^4 + (y_s - 0.5)^2/b^4 + (z_s - 0.5)^2/c^4}$ (2.8b)

For a sphere with *a=b=c=r*, the simplified expression for φ_s will be

$$\cos\varphi_s = (\sin\theta\cos\phi(x_s - 0.5) + \sin\theta\sin\phi(y_s - 0.5) + \cos\theta(z_s - 0.5))/r \tag{2.9a}$$

where $r = \sqrt{(x_s - 0.5)^2 + (y_s - 0.5)^2 + (z_s - 0.5)^2}$ (2.9b)

For the case of the homeotropic anchoring the angle φ in Eq. (2.5) will be equal to φ_s, while for the planar anchoring $\varphi = \varphi_s - \pi/2$.

4 The new director orientation is accepted or rejected according to the Metropolis sampling, in which the new orientation is accepted with probability $p(\mathbf{n_o} \rightarrow \mathbf{n_n}) = \min[1, \exp-(\Delta E / k_B T)]$. As discussed earlier, temperature enters the mean-field Oseen-Frank theory only implicitly through the temperature dependence of the physical constants, and fluctuations are not accounted for; hence, T is a fictitious temperature (the *Monte Carlo temperature*). We initially fix the Monte Carlo temperature at a high value to keep the system from becoming trapped in a local minimum, and the temperature is then gradually decreased. The 'high' temperature term can be quantified with the help of the nematic-isotropic transition temperature. When temperature is too high, there will be a high degree of fluctuations in the orientation of the directors and the temperature becomes dependent on size of the lattice cell [Appendix B].

The algorithm becomes inefficient as the system approaches the global free energy minimum, since increasing numbers of trial moves are rejected; in that case, a scale factor is introduced to restrict the magnitude of the change in director orientation. The procedure for obtaining a trial orientation with a restricted orientation field with the current orientation $\mathbf{u_i}$ is the following: First we generate a unit vector $\mathbf{v_i}$ with a random orientation and multiply it by a scale factor γ. We now add $\gamma \mathbf{v_i}$ to $\mathbf{u_i}$ and normalize the resulting vector to obtain a trial orientation unit vector $\gamma \mathbf{u_i'}$. The scale factor γ is adjusted to permit acceptance of about 50 per cent of the trial moves during the simulations.

5 Steps (2-4) are repeated until equilibrium is achieved.

6 Once equilibrium is achieved, the evolution of the total free energy and other observables are obtained by computing averages over a specified number of MC cycles, typically 20,000.

2.6 Observables and their calculations

2.6.1 Energy

At every cycle, bulk and surface energies are calculated and averaged over the specified number of MC cycles.

2.6.2 Global order parameter, $S_{||}$

We use the Zannoni approach [53] to calculate the global order parameter $S_{||}$ (usually denoted *S*). We first calculate the average order matrix $S_{\alpha\beta}$ over the *N* lattice points, as follows:

$$S_{\alpha\beta} = \frac{1}{N}\sum_{i=1}^{N} n_{\alpha i} n_{\beta i} - \frac{1}{3}\delta_{\alpha\beta} \tag{2.10}$$

Here, $n_{\alpha i}$ is the projection of the unit vector on the coordinate axes, where $\alpha, \beta = x, y, z$, and $\delta_{\alpha\beta}$ is Kronecker's delta. $S_{\alpha\beta}$ is a symmetric matrix with zero trace. Such a matrix can be diagonalized, and the eigenvectors and corresponding eigenvalues λ_1, λ_2, and λ_3 ($\lambda_3 \geq \lambda_2 \geq \lambda_1$) can be calculated. For a uniaxial nematic the eigenvalues are related in the following way:

$$\lambda_2 = \lambda_3 = -\frac{1}{2}\lambda_1 \tag{2.11}$$

The largest eigenvalue determines the order parameter $S_{||}$, and the average orientation of the system is given by the eigenvector associated with that eigenvalue. The relation between the order parameter $S_{||}$ and the maximum eigenvalue λ_1 is given by

$$S_{||} = \frac{3}{2}\lambda_1 \tag{2.12}$$

2.6.3 Orthogonal order parameter, $S_{\perp}$

The global order parameter $S_{||}$ equals zero not only for a random orientation, but also when the orientation is radial. In spheroidal geometries, droplet configuration with homeotropic anchoring conditions may be radial, hence $S_{||}$ alone may not be helpful to completely describe the order. Chiccoli and coworkers [42] introduced an orthogonal order parameter, which we denote $S_{\perp}$, defined for ellipsoids as follows:

$$S_{\perp} = \frac{1}{N} < \sum_{i=1}^{N} [\frac{3}{2}(\mathbf{n}_i.\mathbf{r}_i)^2 - \frac{1}{2}] > . \tag{2.13}$$

Here, $\mathbf{r_i}$ is the local normal to the concentric ellipsoid passing through the center of the i^{th} lattice cell. In the case of a sphere, $\mathbf{r_i}$ will always be a radial vector. Thus, for a radial orientation in a spherical geometry, $S_{\perp}$ is unity and $S_{||}$ is zero; for a uniform orientation, $S_{||}$ is unity and $S_{\perp}$ is zero. It is possible for $S_{||}$ and $S_{\perp}$ to have comparable values in an ellipsoidal geometry with a large aspect ratio.

In the case of a cylinder, $\mathbf{r_i}$ again is a radial vector always pointing towards the cylindrical axis. Thus, $S_{\perp}$ is unity for a planar-radial (PR) orientation, positive non-zero for planar-polar (PP) and –1/2 for director orientation along cylindrical axis. It is possible for $S_{\perp}$ to take both negative and positive values for an escape-radial (ER) orientation.

2.6.4 Escape order parameter, S_{ER}

In the case of cylinder geometries with homeotropic anchoring conditions, we also calculate an escape order parameter, which we denote S_{ER}, defined by [54]:

$$S_{ER} = \frac{1}{N} < \sum_{i=1}^{N} [\frac{3}{2}(\mathbf{n}_i.\mathbf{z})^2 - \frac{1}{2}] > . \tag{2.14}$$

Here, cylinder axis is along the z direction. S_{ER} measures the degree of escape from the plane perpendicular to the cylinder axis. Thus, S_{ER} equals $-1/2$ for a PP orientation and unity for a uniform orientation along the cylinder axis. In the case of an ER orientation, S_{ER} can also take both negative and positive values.

2.6.5 Orientational pair correlations

Another useful way to study the droplet configuration quantitatively is through particle angular correlation coefficients, which describe a set of expansion coefficients of the rotationally invariant pair correlation function that are particularly useful in determining the steady state. The calculations of correlation functions are time consuming, and we calculated the pair correlation coefficient $G_2(r)$ only to study the N-I phase transition. To calculate the correlation between two particles i and j at a distance r, the definition of $G_2(r)$ is [53]:

$$G_2(r) = < [\frac{3}{2}(\mathbf{n}_i.\mathbf{n}_j) - \frac{1}{2}] > \tag{2.15}$$

In practice, the average correlation function $G_2(r)$ is calculated during the course of a simulation in the following way: First, we divide the range of interparticle separations into a number of intervals of width Δr. For every separation r, an integer number is assigned. Now, for a given configuration, a particle i is chosen and $G_2(r)$ is computed and

added for every pair *i,j* into the interval corresponding to the separation *r*. This process is repeated until all particles are chosen. To normalize the coefficient $G_2(r)$, we divide the content of every interval by the number of pairs it holds.

2.6.6 Droplet visualization

The information of orientation and position of directors is stored in arrays, and droplet structure can be visualized by the following methods:

Vectorial representation

The droplet information is passed to 'PGPLOT' graphical software and the vectorial orientation distribution can be shown for planes orthogonal to the *x*, *y*, or *z*-axis at different cross-sections inside the droplet.

Simulated confocal micrographs

Droplet order can be visualized more easily using simulated fluorescence confocal polarizing microscopic images. We use the fluorescence confocal polarizing microscopy (FCPM) technique proposed by Shiyanovskii et. al. [55] to obtain computer-generated confocal images both in the plane and along the direction of observation. In principle, the FCPM maps the intensities of polarized fluorescent light, which is emitted by the nematic sample. The technique allows us to collect the fluorescent light from a very small region of the sample and the obtained intensity provides the 3D image of orientation of the liquid crystal sample. The intensity at any point (*x,y,z*) in the sample is given by the following equation [55]:

$$I(x,y,z) \propto \int [g_x n_x^2(x,y,z') + g_y n_y^2(x,y,z') + g_z n_z^2(x,y,z')]\, T(z-z')\, dz', \qquad (2.16)$$

where $g_x + g_y + g_z = 1$; g_x, g_y, and g_z are the anisotropy parameters of fluorescence as described in [55]. $T(z')$ is the weight function, and it is of the Gaussian type $T(z') = \frac{1}{\Delta z\sqrt{\pi}} \exp\left[-(z'/\Delta z)^2\right]$.

Simulated optical pattern of droplet structure

Confocal micrographs only provide 2-D information about the droplet configuration. To analyze the droplet structure thoroughly, one should look at different cross-sections of the droplet at different positions and thus a lot of data is required to visualize the droplet structure. To solve this problem, we calculate an integrated optical image of the droplet configuration. To simulate the integrated optical texture of nematic droplets, we use a standard matrix approach as employed by various research groups (Ondris-Crawford et al. [56], Xu et. al. [57], and Berggren et. al. [58].) The incoming light (defined to travel along the *z*-axis) is characterized by a 1x4 Stokes vector or 1x2 Jones vector [5,59]. The droplet is divided into many thin slices, with the layer direction perpendicular to the incoming light. Each point within a slice is treated as a birefringent slab and is described by a 4x4 Muller matrix or 2x2 Jones matrix. (The two matrix methods produce exactly the same results; the Jones matrix has complex components that are related to the real Muller matrix components [59].) The light beam passing through a row of slabs is then retarded by the matrix resulting from the product of the Jones matrices for each point in the light path. The Jones matrix corresponding to slab ***i***(*x,y,ih*) is given by

$$\mathrm{J_i} = \begin{bmatrix} \cos^2\phi_i \exp(i\delta_i) + \sin^2\phi_i & \cos\phi_i \sin\phi_i [\exp(i\delta_i) - 1] \\ \cos\phi_i \sin\phi_i [\exp(i\delta_i) - 1] & \sin^2\phi_i \exp(i\delta_i) + \cos^2\phi_i \end{bmatrix}, \tag{2.17}$$

where ϕ_i is the azimuthal angle between the projection of the axis of the slab i on the plane perpendicular to the direction of the light (in our case the xy plane) and the x-axis. The phase difference δ_i of the slab i is defined as [5]

$$\delta_i = \frac{2\pi}{\lambda} \Delta z [n_e(\beta_i) - n_o], \tag{2.18}$$

where λ is the wavelength of the light, Δz is the thickness of the layer, and n_o is the ordinary refractive axis of the nematic crystal. $n_e(\beta_i)$ is the local extraordinary refractive index, given as

$$n_e^2(\beta_i) = \frac{n_o n_e}{\sqrt{n_o^2 \sin^2 \beta_i + n_e^2 \cos^2 \beta_i)}}, \tag{2.19}$$

where β_i is the angle between the axis of the i^{th} slab and the direction of the propagation of the light.

The calculation of the transmission of the light through a droplet viewed between crossed-polarizers is performed by computing the resulting Jones vector of the polarized and retarded light [5]:

$$\begin{bmatrix} A_1 \\ A_2 \end{bmatrix} = P_A \Pi_i J_i P_P \begin{bmatrix} A_{1,i} \\ A_{2,i} \end{bmatrix}, \tag{2.20}$$

where $A_{1,i}$ and $A_{2,i}$ are the components of the matrix corresponding to the Jones vector of the unpolarized light incident on the polarizer. P_P and P_A are the Jones matrices corresponding to the polarizer and analyzer, respectively. To obtain the maximum possible intensity, the polarizer must be perpendicular to the analyzer; in that case, P_P and P_A are given by [59]:

$$\mathrm{P_P} = \begin{bmatrix} 1 & 0 \\ 0 & 0 \end{bmatrix}, \qquad \mathrm{P_A} = \begin{bmatrix} 0 & 0 \\ 0 & 1 \end{bmatrix} \tag{2.21}$$

In practice, the angles ϕ and β for each slab are obtained from simulated droplet configurations. We calculate the intensity of the light [Eq. 2.19] using the following typical values of the parameters: λ=0.55μm, n_o=1.5, n_e=1.7, Δz=0.1μm, $A_{1,i}$=1, and $A_{2,i}$=0. Using a MATLAB code, a normalized gray scale image of the droplet configuration is then obtained, where white and black correspond to the highest and lowest intensity, respectively. When there is no sample between the polarizer and analyzer, the transmission will be zero.

2.7 Computational details

We carry out calculations in dimensionless form and define the following dimensionless quantities for our simulations:

$$R^* = \frac{R}{l} \tag{2.22a}$$

$$T^* = \frac{k_B T}{Kl} \tag{2.22b}$$

$$E_b^* = \frac{E_b}{NKl}, \tag{2.22c}$$

$$\text{and } C_v^* = \frac{N}{T^{*2}}\left(< E_b^{*2} > - < E_b^* >^2\right). \tag{2.22d}$$

where R is the radius of the drop, l is the lattice spacing, R* is the dimensionless radius, T* is the dimensionless Monte Carlo temperature (or scaled temperature), E_b^* is the

scaled bulk energy, and C_v^* is the scaled heat capacity. The total number of cells inside a droplet is given by $N = \frac{4}{3}\pi R^{*3}$.

It is straightforward to show for the case of a spherical droplet of radius R with equal elastic coefficients that the only parameters (other than T^*) are the droplet radius R ($R = l \times R^*$) and the dimensionless group WR/K. Hence, changing the drop radius with a fixed lattice spacing and changing the number of lattice sites for a fixed drop size are equivalent calculations [see Appendix D].

Chapter 3
Results for Spheres and Spheroids

In this chapter we will discuss the effect of the anchoring parameter and the elastic coefficients on director orientation inside spherical and spheroidal droplets. First we calculate the orientation distribution corresponding to the minimum energy state; we then explore the possibility of other locally stable states. We also calculate the energy required to overcome the activation barrier where the system is bi-stable, and we study the transition path from a locally stable state to the equilibrium state. For all of these calculations we consider orthogonal anchoring conditions at the droplet surface.

The chapter is organized as follows: First results for different cases for spherical droplets are discussed. Subsequently, results for spheroids of different aspect ratio are presented.

3.1 Results for spherical droplets

3.1.1 Equal elastic constant calculations

We first discuss results for a spherical droplet with equal elastic coefficients. Random initial conditions were used for these calculations, which were carried out for droplet systems with N =14,328, 82,696, 179,904, 268,096, and 523,984 lattice cells,

corresponding to 2,792, 8,872, 14,936, 19,328, and 31,216 surface cells, respectively. For a fixed droplet size, increasing N corresponds to decreasing the lattice spacing. For a fixed lattice spacing of l=0.1μm, these droplet systems are equivalent to spherical droplets of radius R=1.5μm, 2.7μm, 3.5μm, 4.0μm and 5.0μm, respectively, and we will use these length scales for specificity. The results are valid, however, for any droplet size with the same value of WR/K [Appendix A3].

To examine the effect of the anchoring parameter W and droplet size R on the droplet structure, we calculate the order parameters $S_{||}$ and $S_{\perp}$ for all droplets. To see the effect of the anchoring parameter only, we choose the droplet with N = 82,696 and l=0.1μm; the calculated order parameters $S_{||}$ and $S_{\perp}$ are plotted as functions of the surface extrapolation length (K/W) in Fig. 3.1. We observe that below a critical value of K/W=0.49μm, $S_{\perp}$ is close to unity and the global order parameter $S_{||}$ is close to zero; hence the droplet configuration for strong anchoring is perfectly radial. For K/W larger than that the critical value, the radial order parameter $S_{\perp}$ decreases with K/W and the global order parameter $S_{||}$ strongly increases; in this case that the structure is aligned and is insensitive to the radial boundary conditions. We observe that the parameters $S_{||}$ and $S_{\perp}$ change abruptly across the critical region, indicating the onset of a first order transformation between radial and axial orientations at the critical K/W.

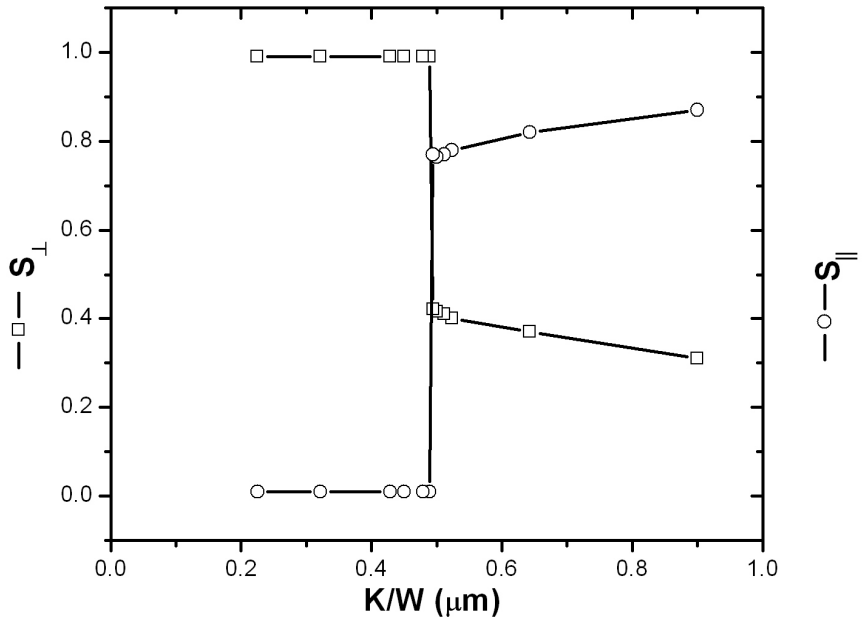

Fig 3.1: Radial order parameter $S_{\perp}$ and global order parameter $S_{||}$ as functions of the surface extrapolation length K/W for droplet with N=82696 lattice cells.

The equilibrium orientation distributions are shown for K/W=0.45μm and K/W=0.64 μm in Figs. 3.2 and 3.3, respectively. These are planar cuts orthogonal to three axes (x, y and z) made at the droplet center. We observe a radial structure with an escape at the droplet center for K/W=0.45μm, while a near parallel (or axial) structure is obtained with K/W=0.64μm. The orientation distribution for K/W=0.64μm will have a different appearance on another planes [Figs. 3.3]. For a better visualization, corresponding simulated fluorescence confocal polarizing microscopic (FCPM) images for these orientations (same planar cuts) are shown in Figs. 3.4 and 3.5, where the escape at the droplet center with radial orientation and parallel order with axial orientation can be easily visualized. However, as discussed earlier, droplet order can be visualized more easily using integrated simulated optical micrographs. The calculated optical

micrographs for K/W=0.45μm and K/W=0.64μm are shown in Fig. 3.6. The radial morphology is clearly revealed through the classic Maltese cross image [Fig. 3.6a] and is symmetric with the rotation [Figs. 3.7]. The details of the image for the axial orientation [Fig. 3.6b] will depend on the relative angle of the simulated polarized light beam and the mean orientation direction (see Figs. 3.8).

We show the propagation of the boundary-induced ordering inside the droplet in Figs 3.9. We divide the droplet into 15 concentric cells and investigate how the two order parameters $S_{||}$ and $S_{\perp}$ change from the center of the droplet (r=0) to the droplet surface (r=15) for different surface extrapolation lengths. We notice that the radial nature of the droplet configuration is maintained for smaller extrapolation lengths (K/W < 0.49μm) until we reach the central core of the droplet [Fig. 3.9a]. In the core region the director escapes from the radial direction to avoid forming an energetically expensive point defect. The escaped behavior is again reflected in Fig 3.9(b), where $S_{||}$ at smaller extrapolation lengths is close to unity in the core region and then goes to zero as we move towards the boundary. For larger extrapolation lengths, K/W > 0.49μm, both $S_{||}$ and $S_{\perp}$ have comparable values and an axial structure is confirmed. Increasing K/W leads to more parallel order in the structure.

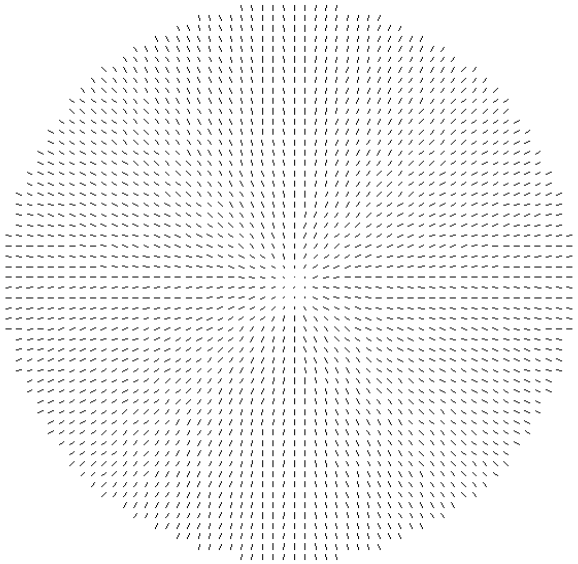

(a)

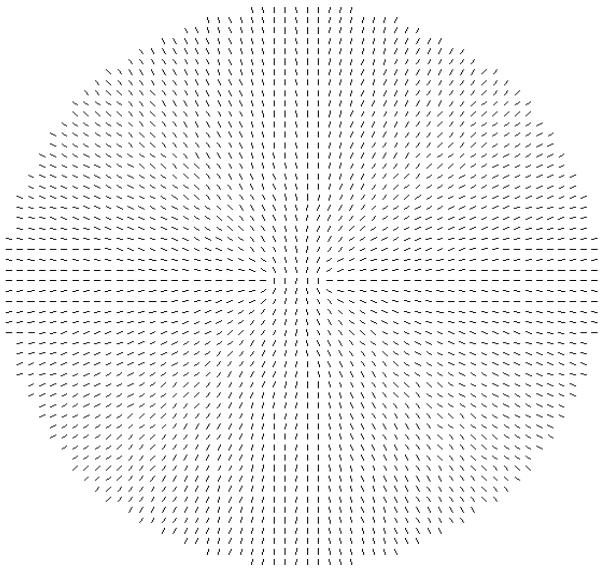

(b)

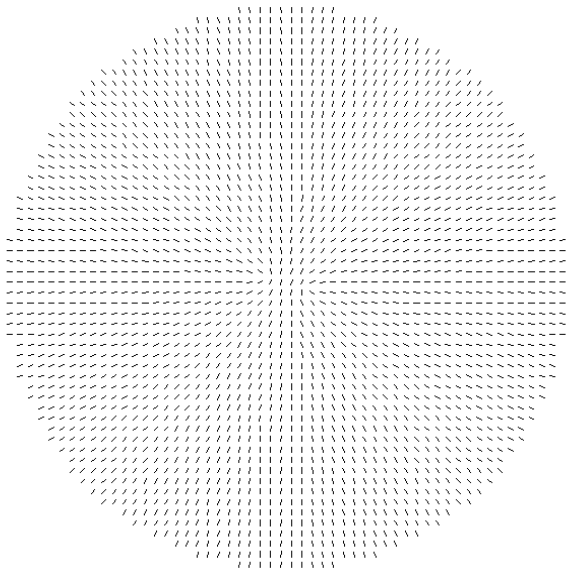

(c)

Fig. 3.2: Director orientation with N=82,696 and K/W = 0.45μm. These are planar cuts orthogonal to three axes (x,y, and z).

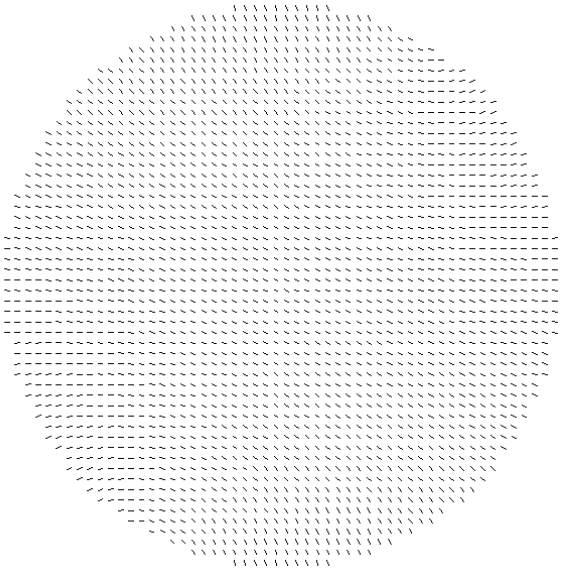

(a)

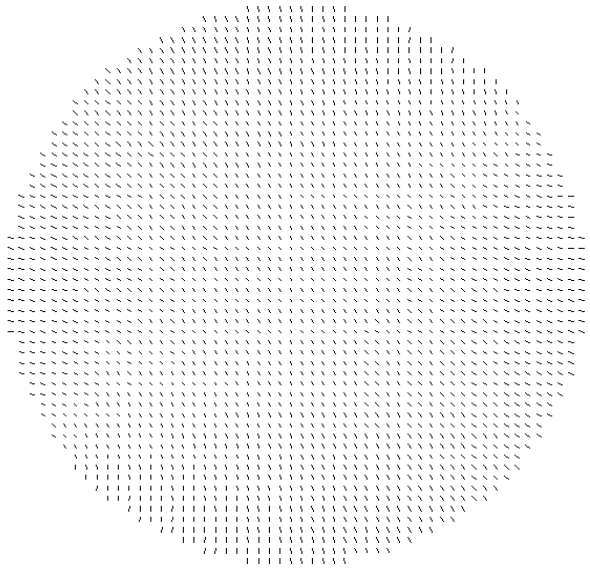

(b)

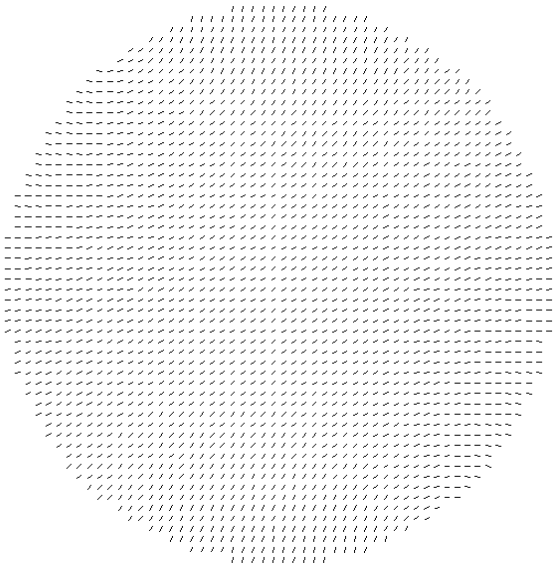

(c)

Fig. 3.3: Droplet configuration for three different planes of the droplet with N=82,696, K/W = 0.64μm.

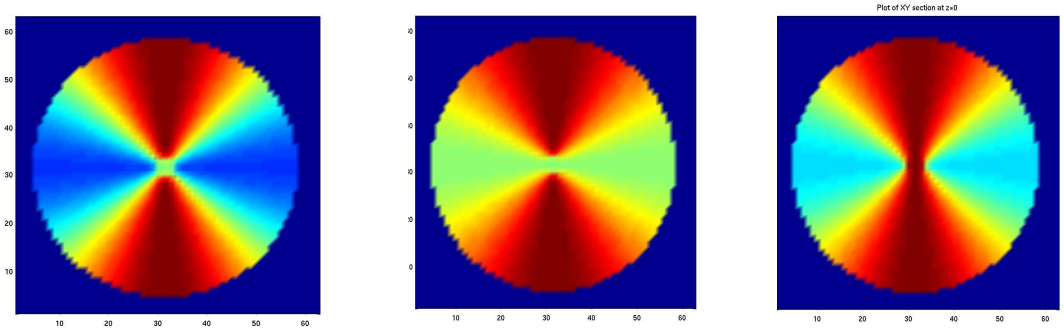

Fig 3.4: Simulated FCPM images of the planar cuts (orthogonal to three axes) for droplet configuration with surface extrapolation length K/W=0.45μm.

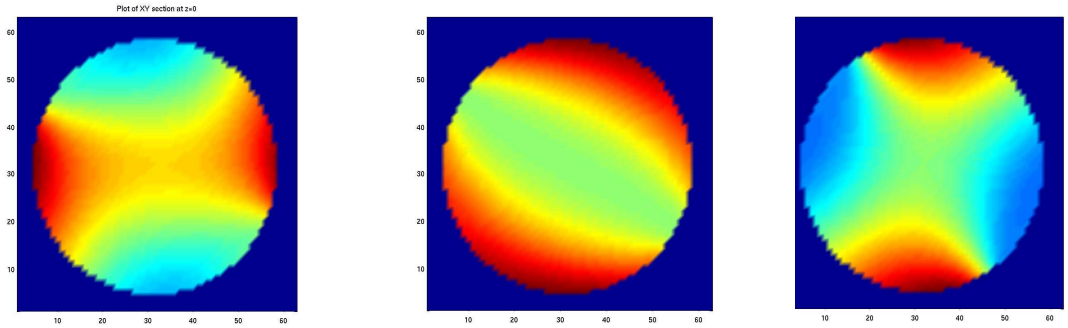

Fig 3.5: Simulated FCPM images of the planar cuts (orthogonal to three axes) for droplet configuration with surface extrapolation length K/W=0.64μm.

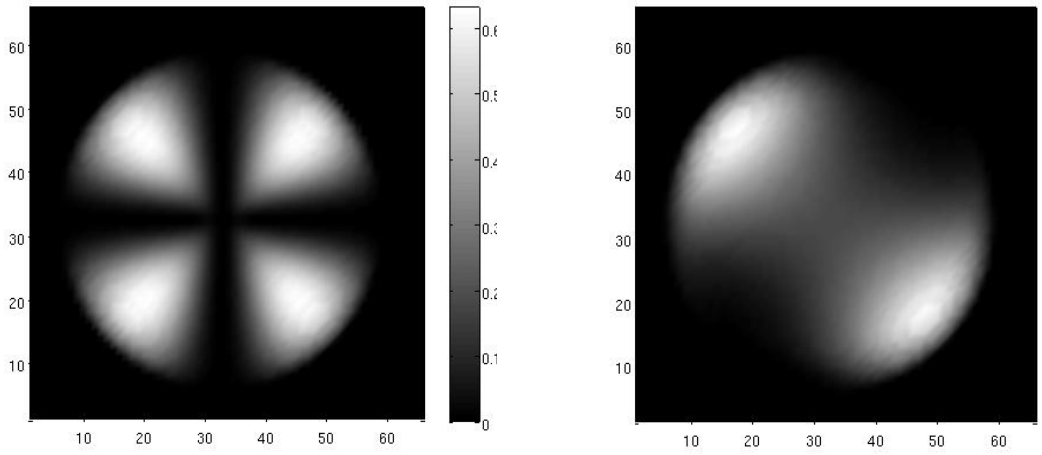

(a) (b)

Fig 3.6: Simulated polarized optical micrographs for the orientations with $K/W = 0.45\mu$m (a) and $K/W = 0.64\mu$m (b).

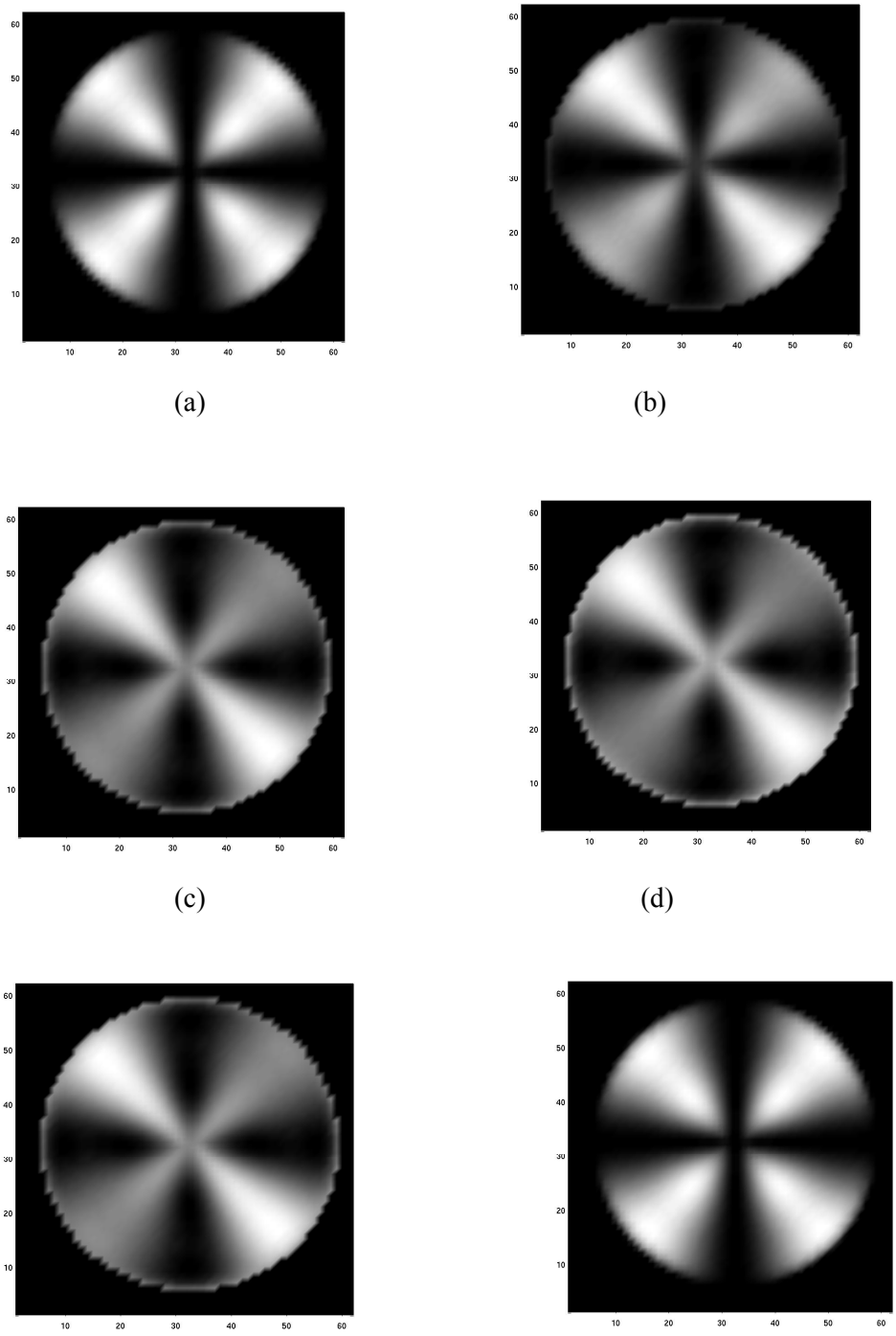

(a) (b)

(c) (d)

(e) (f)

Fig 3.7: Simulated polarized optical micrographs with K/W=0.45μm. Different images correspond to the angle ϕ made by the polarizer to the incident light. (a) $\phi = 0$ (b) $\phi = \pi/12$ (c) $\phi = \pi/6$ (d) $\phi = \pi/4$ (e) $\phi = \pi/3$ and (f) $\phi = \pi/4$.

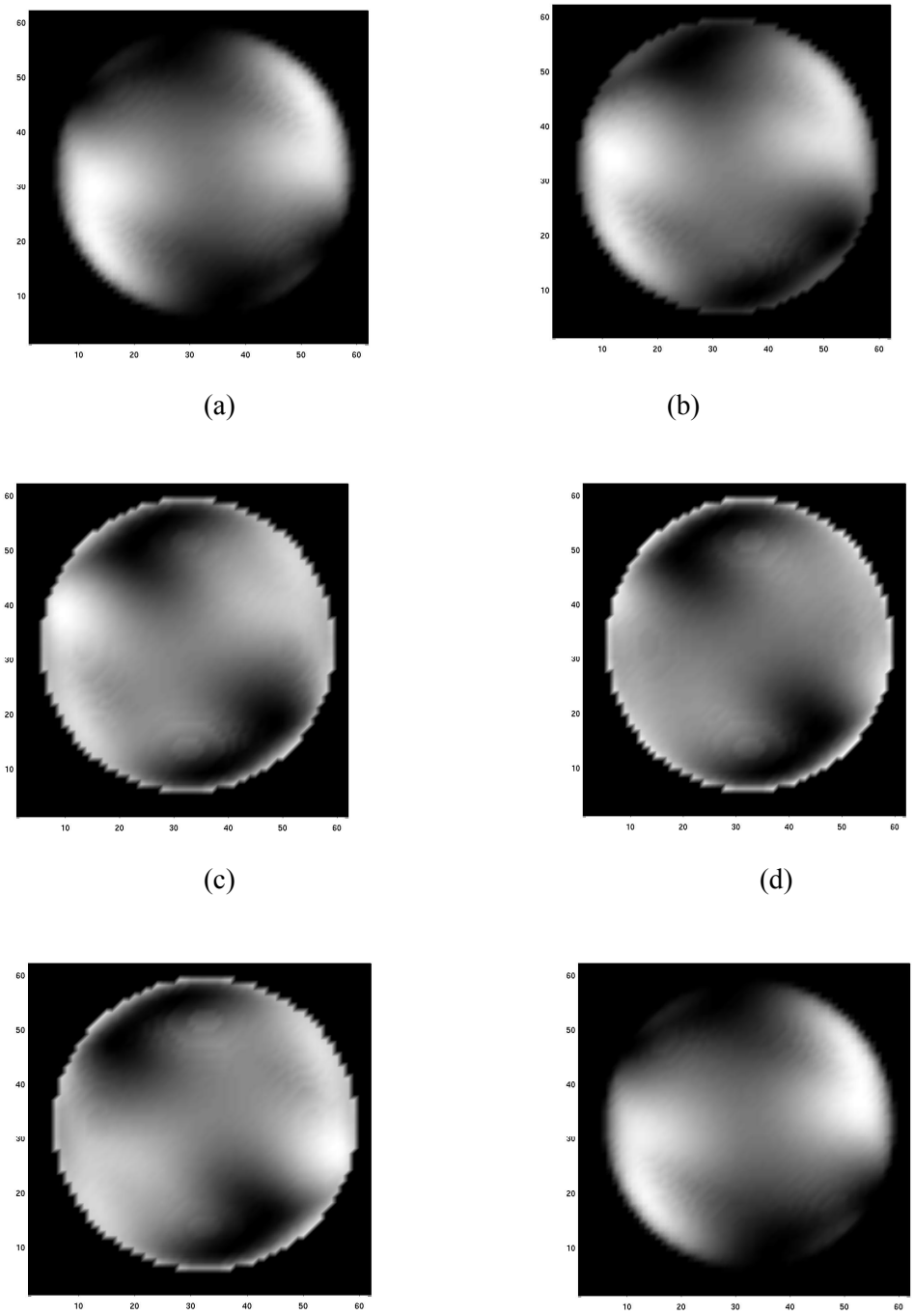

Fig 3.8: Simulated polarized optical micrographs with K/W=0.64μm. Different images correspond to the angle ϕ made by the polarizer to the incident light. (a) $\phi = 0$ (b) $\phi = \pi/12$ (c) $\phi = \pi/6$ (d) $\phi = \pi/4$ (e) $\phi = \pi/3$ and (f) $\phi = \pi/4$.

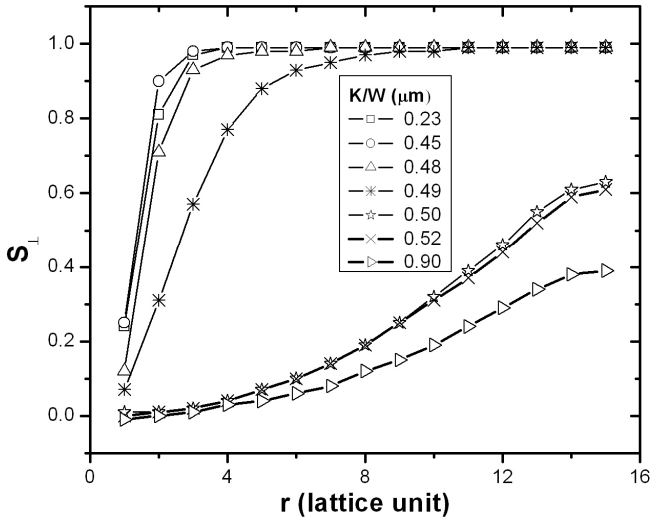

(a)

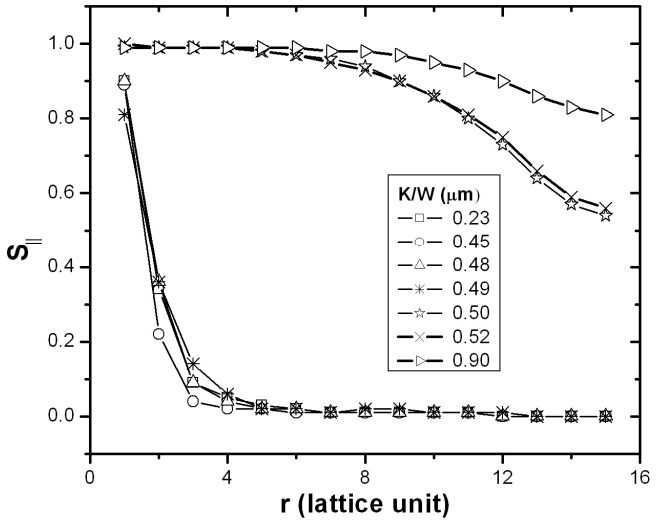

(b)

Fig 3.9: Order parameters $S_\perp$ (a) and $S_\parallel$ (b) as functions of the distance r to the droplet center at different surface extrapolation lengths K/W.

To examine the effect of the droplet size on the director configuration, along with the anchoring parameter W and the mean elastic constant K, the calculated order parameters $S_{||}$ and $S_{\perp}$ for different size droplets are plotted as functions of K/W in Figs. 3.10. We observe that for the same value of K/W, large droplets have a radial alignment while smaller droplets have a parallel alignment. A radial orientation has an energetically expensive point defect at the droplet center, which makes aligned axial structures favorable for small droplets. For small values of K/W, an axial structure becomes more energetically expensive because of the higher penalty associated with the surface anchoring energy, and therefore radial structures are preferred.

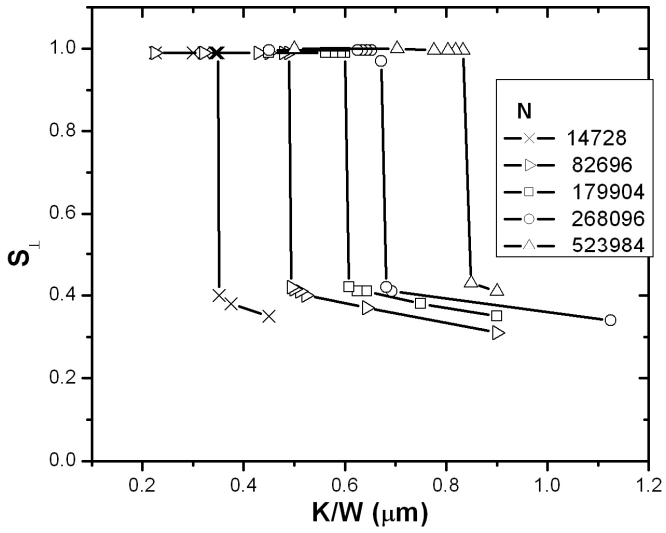

(a)

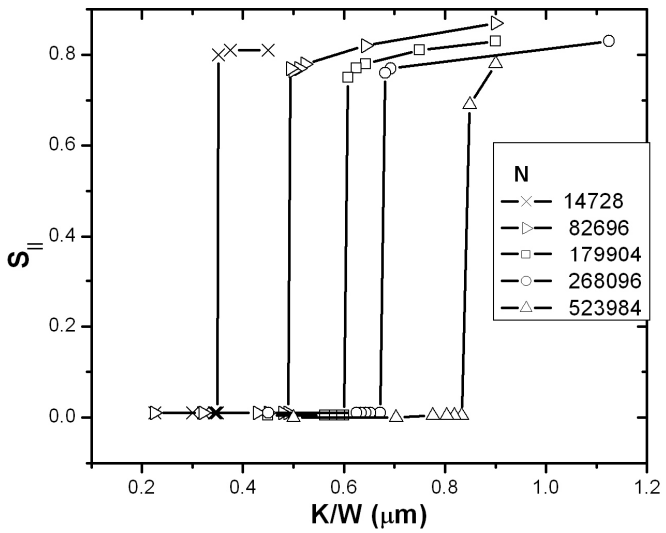

(b)

Fig 3.10: Radial order parameter $S_\perp$ (a) and global order parameter $S_\parallel$ (b) as functions of the surface extrapolation length K/W for different size droplets.

To combine the effect of all parameters, we plot $S_{||}$ and $S_{\perp}$ as a function of the dimensionless parameter *WR/K* in Figs. 3.11. This plot demonstrates convergence with respect to the number of lattice sites for a fixed droplet radius. As expected, there is a first-order transition from a nearly parallel conformation to a radial conformation at a critical value of *WR/K* of about 5.95, which is somewhat larger than the value of 3 that follows from the simple analysis based on a transition from a perfectly parallel alignment (Sec. 1.4).

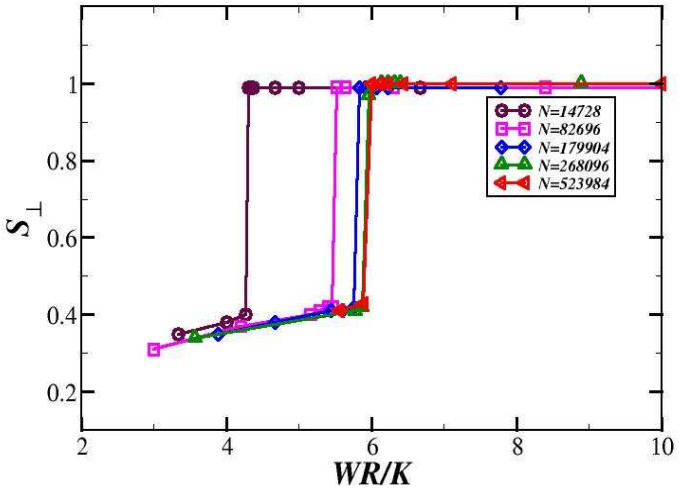

(a)

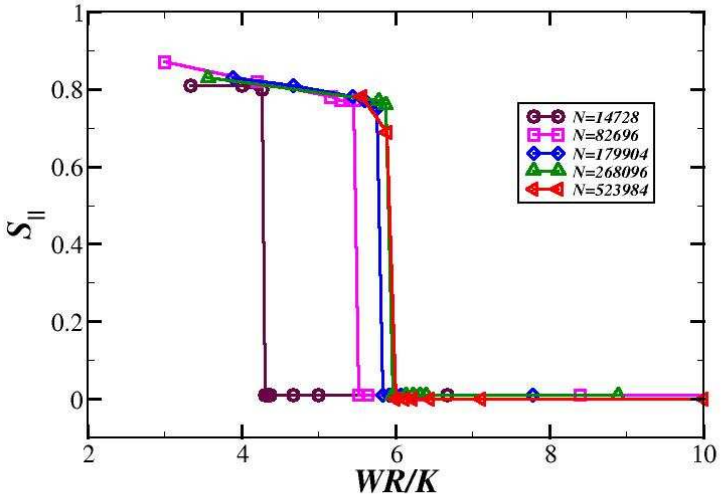

(b)

Fig 3.11: Radial order parameter $S_{\perp}$ (a) and global order parameter $S_{\|}$ (b) as functions of the anchoring strength parameter *WR/K* for various discretizations. Convergence is clearly observed as the number of lattice cells *N* increase.

Next, we see how the bulk and surface energies obtained from the simulations vary with the parameter *WR/K*. To compare the energies for different size droplets, we normalize both the bulk energy (E_b) and surface energy (E_s) by dividing them by the analytical energy of a perfectly radial structure ($4\pi KR$). A comparison of normalized bulk elastic and surface energies as functions of *WR/K* for different size droplets is shown in Figs. 3.12. As expected, the bulk elastic energy increases with *WR/K* until *WR/K* is lower than the critical value, and then it stays constant in the radial region. Similarly, the normalized surface energy increases with *WR/K* until we reach the critical value, and then it takes a value close to zero in the radial region. As discussed earlier, the energy of a

perfectly radial structure can be calculated analytically, but we cannot calculate the energies of an escaped radial or an axial structure of different radial and global order parameters. Our simulations provide an efficient method to calculate the energy for any structure. The efficiency of our algorithm is reflected by the results we obtain for different size droplets. We observe that the normalized energy plots for different size droplets superimpose on each other and give a unique plot. We also show a plot of the total of the normalized bulk and surface energies with *WR/K* for different size droplets [Fig. 3.12c]. As expected, an axial structure is energetically favorable in the region *WR/K* $\leq$ 5.95, and for *WR/K* > 5.95 a radial structure becomes energetically more favorable. The region close to *WR/K* =5.95 is a bi-stable region; depending on the choice of initial configuration, initial Monte Carlo Temperature, and simulated annealing scheme, we obtain radial or axial structures with essentially equal probability.

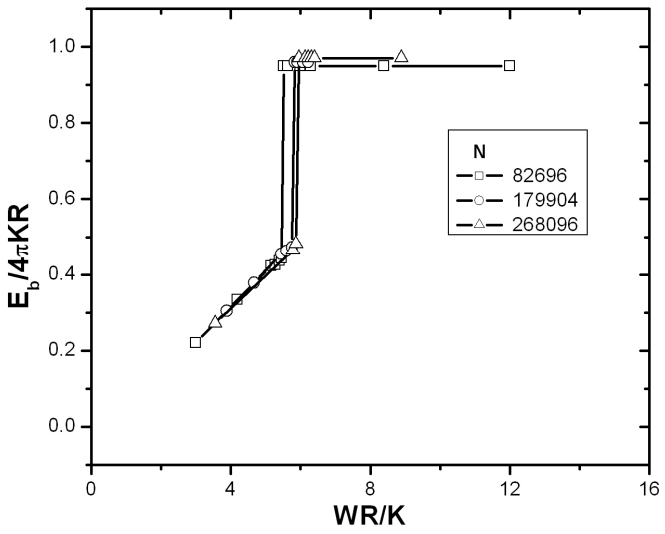

(a)

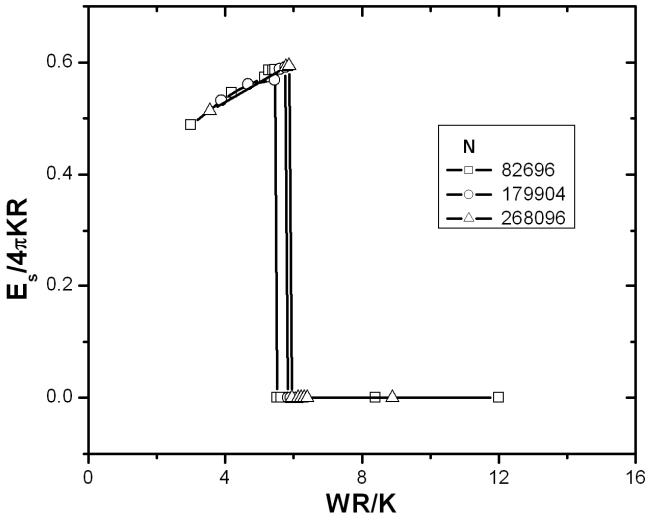

(b)

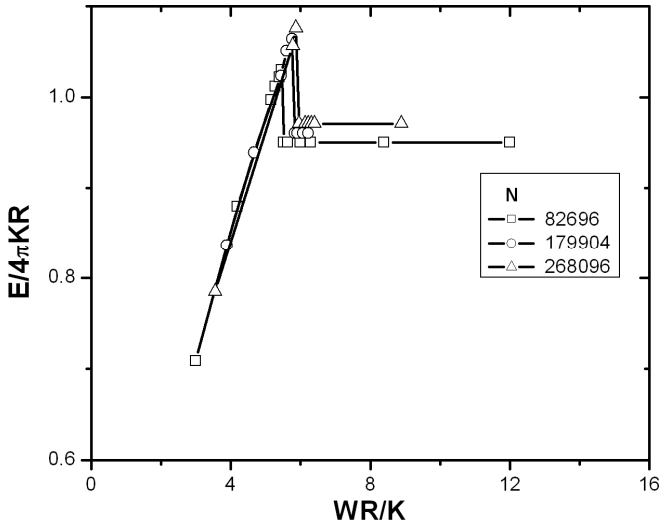

(c)

Fig. 3.12: Normalized bulk elastic energy (a), surface anchoring energy (b), and total energy (c) versus *WR/K* for different size droplets.

3.1.2 Multiplicity

We have found that other locally stable states may exist for equal elastic coefficients by starting simulated annealing calculations with a radial distribution when *WR/K* is less than the transition value and with a near-axial distribution when *WR/K* is greater than the transition value, keeping the Monte Carlo temperature (hence the fluctuations) small. To compromise between accuracy and computational efficiency we choose a system of 82,696 lattice cells. We observe that in such cases, convergence to a second local minimum in free energy is obtained; in the former case the local free energy state is radial, while in the latter it is an axial state with increasing distortion as *WR/K* is increased. The calculated order parameters for both the global and local minima are shown in Figs. 3.13.

The complementary order parameters $S_{||}$ and $S_{\perp}$ comprise a minimal description of the droplet morphology. The simulations converge to a local free energy minimum at each value of the Monte-Carlo temperature for a given *WR/K* and specified starting conditions, and each of these converged states is characterized by a unique pair ($S_{||}$, $S_{\perp}$). Hence, incremental changes in the Monte-Carlo temperature, starting from a local minimum, will provide a path through the conformation space along a sequence of feasible quasi-static states; this path can be tailored to lead to the global minimum by first increasing the Monte-Carlo temperature until the morphology has changed from one qualitative type to the other, then decreasing the temperature to reach the equilibrium state. Figure 3.14, for example, shows the bulk and surface energies at *WR/K* = 3.6 for a succession of successful Monte Carlo steps at increasing dimensionless Monte Carlo temperatures $T^* = k_B T/Kl$, where T is the MC temperature. Since an axial configuration

costs less in bulk energy but has a high surface energy, the transition from a radial conformation to an orientation with substantial alignment is clearly observed at T^* between 0.337 and 0.347. (A nematic-isotropic transition occurs at T* = 0.375 [Appendix A1].) The small increase in the surface energy ($0.6\pi KR$) is offset by the small decrease ($2.4\pi KR$) in the bulk energy, with a net change in the total free energy of only 0.35%. The sequence of states in the $S_{||}$-$S_{\perp}$ plane, together with the corresponding free energies as a three-dimensional curve, are shown in Fig. 3.15. The transition between two states with similar energies, and the corresponding development of global alignment, is readily seen. The difference between the free energy of the initial state and the maximum free energy along the path is an upper bound for the height of the energy barrier between the local and global equilibrium states; it is only an upper bound because our algorithm gives a particular path through the conformation space, and another path might exist that has a lower-barrier.

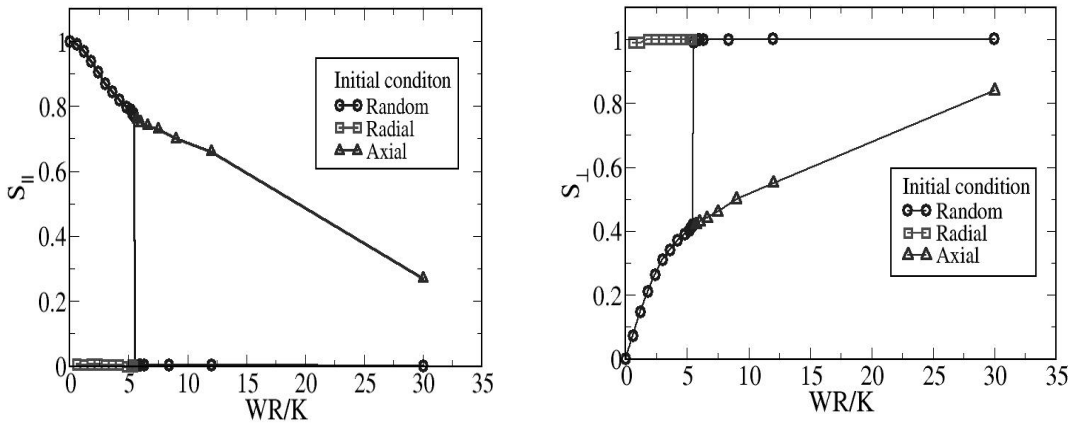

(a) (b)

Fig 3.13. Order parameters $S_{\|}$ (a) and $S_{\perp}$ (b) as functions of WR/K. (○) Global minimum. (Δ) Axial local minimum. (◊) Radial local minimum.

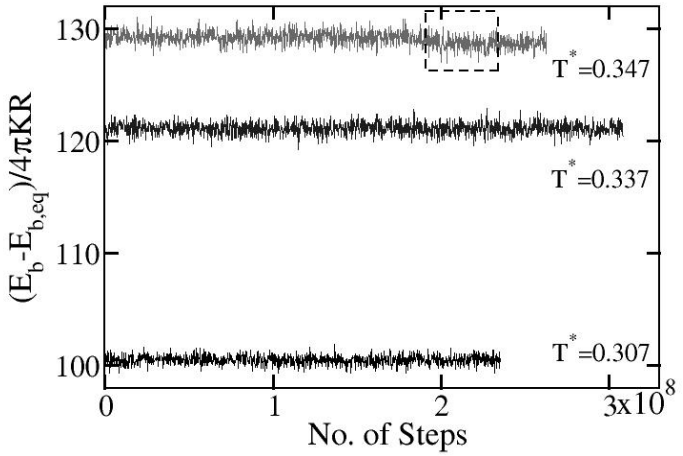

(a)

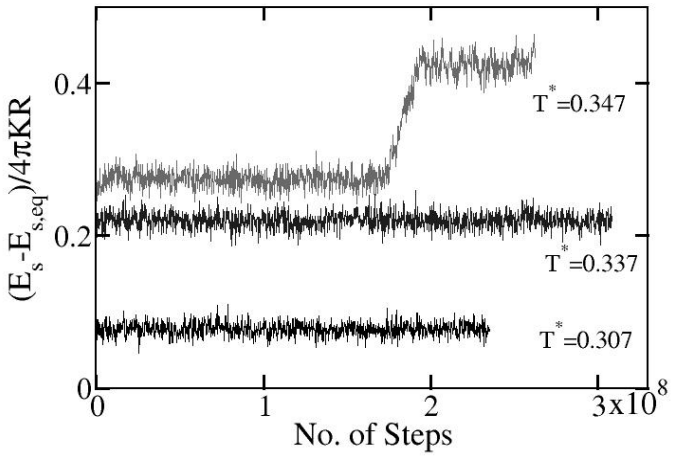

(b)

Fig. 3.14. Bulk and surface free energies for equal elastic coefficients with *WR/K* = 3.6 at different values of reduced Monte Carlo temperature $T^* = k_B T/Kl$. Average bulk energies before and after the transformation are $<(E_b - E_{b,eq})>/4\pi KR$ =129.25 and 128.65, respectively, while average surface energies before and after the transformation are $<(E_s - E_{s,eq})>/4\pi KR$ = 0.27 and 0.42, respectively.

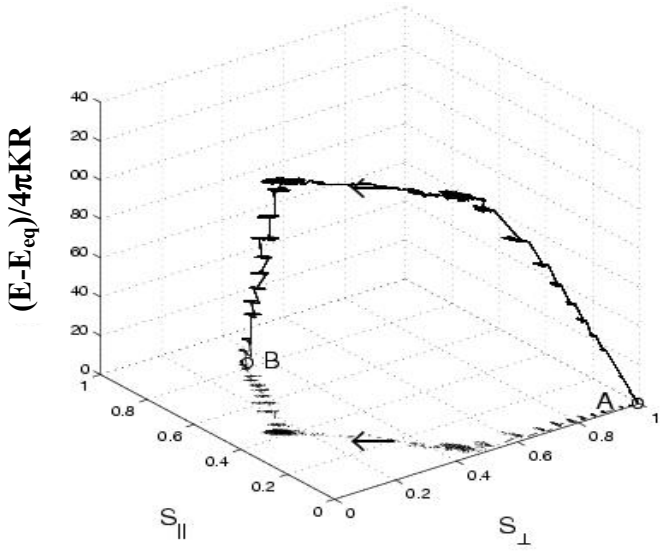

Fig. 3.15. Path in conformation space and corresponding energy in passing from a locally stable radial state (A) to the axial free energy minimum state (B) with *WR/K* =3.6.

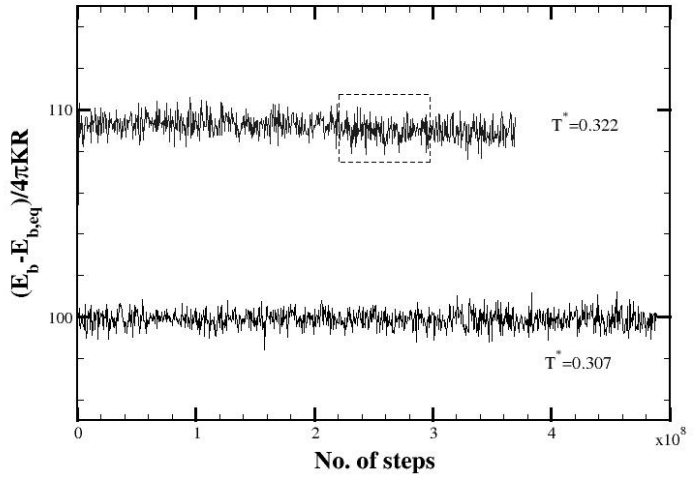

(a)

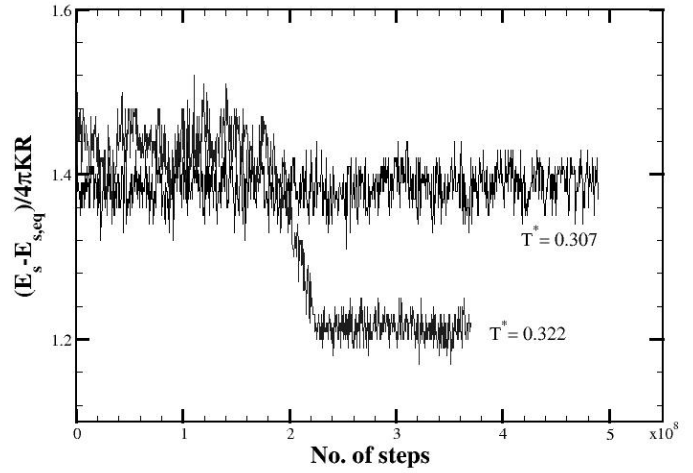

(b)

Fig. 3.16. Bulk and surface free energies with *WR/K* = 7.5 at different values of T^*. Average bulk energies before and after the transformation are $<(E_b-E_{b,eq})>/4\pi KR$ =109.3 and 108.95, respectively, while average surface energies before and after the transformation are $<(E_s-E_{s,eq})>/4\pi KR$ = 1.44 and 1.21, respectively.

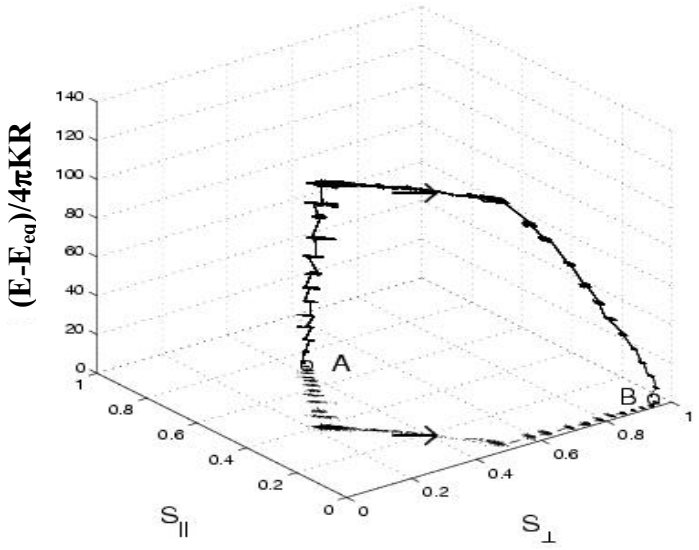

Fig. 3.17. Path in conformation space and corresponding energy in passing from a locally stable axial state (A) to the radial free energy minimum state (B) for *WR/K* =7.5.

We observe a different behavior in Fig 3.16, where we plot the bulk and surface energies at *WR/K* = 7.5 for a succession of successful Monte Carlo steps at increasing dimensionless Monte Carlo temperatures *T*. In this case, both bulk and surface energies are lowered at the transition. The transition from the initial axial orientation to the equilibrium radial confirmation occurs for *T** between 0.307 and 0.322. The sequence of states in the $S_{||}$-$S_{\perp}$ plane, together with the corresponding free energies as a three-dimensional curve, are shown in Fig. 3.17.

The estimated energy barrier is shown as a function of *WR/K* in Fig. 3.18. The maximum corresponds to an energy density of about 2,000 J/m^3 (Pa) for a droplet with a radius of 1 μm and a typical elastic coefficient of 5×10^{-12} N. This energy density could be transmitted mechanically in a dilute suspension with a suspension viscosity of 50 Pa-s at

a shear rate of about 40 s^{-1}; it would require shear rates of the order of 80,000 s^{-1} for a suspension with a viscosity comparable to a typical nematic viscosity of 0.025 Pa-s.

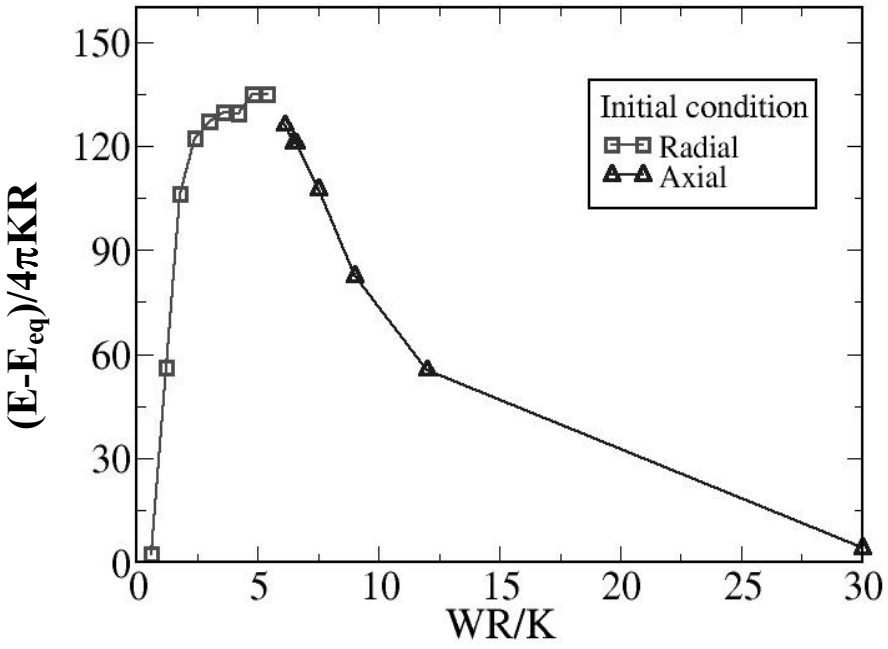

Fig. 3.18. Estimated energy barrier for spherical droplets as a function of *WR/K*.

3.1.3 Defect development

Figures 3.19, 3.20, and 3.21 show the development of defects and transitions between locally stable and equilibrium energy states for different initial and boundary conditions. Figure 3.19 shows the progression of the structural change with Monte Carlo steps during the transition from a locally stable radial conformation to the stable aligned conformation at $WR/K = 5.1$, which is close to the transition. Radial order is initially lost in the region of the singularity at the origin, and the parallel orientation then spreads outward to envelop the entire droplet. The sequence is different during a transition from radial to axial with weak anchoring (WR/K=0.6), as shown in Fig. 3.20; in this case the singularity moves asymmetrically from the center towards a point on the surface as the parallel orientation develops. We also show a transition from an aligned conformation to a strong-anchoring global minimum (WR/K=1000) in Fig. 3.21; in this case, two defects originate at opposite poles, progress to the center, and merge into the center singularity of a radial orientation.

3.1.4 Unequal elastic constants

Effect of the saddle-splay constant

We have examined the effect of the saddle-splay coefficient k_{24} by carrying out droplet calculations in which $k_{11}=k_{22}=k_{33}$ and the ratio k_{24}/k_{11} is varied between 2/3 and 4/3. All calculations were performed with N=82696 lattice cells. The computed order parameters $S_{||}$ and $S_{\perp}$ are shown as functions of WR/k_{11} for different values of k_{24} in Fig. 3.22. The droplet orientation is not affected by k_{24} when WR/k_{11} is large ($WR/k_{11} > 7$), and we always obtain a radial structure. For low WR/k_{11}, either a radial or an axial structure is

obtained *depending* on the value of $k_{24;}$ low values of k_{24} favor an axial structure, while high k_{24} favors a radial structure.

To combine the effect of k_{24} with other constants, following Eq. 2.7a (Sec. 2.4), we plot $S_{||}$ and $S_{\perp}$ as a function of $WR/(2k_{11}\text{-}k_{24})$ in Figs. 3.23. The lines in Fig. 3.22 for different values of k_{24} overlap to a single plot for $WR/(2k_{11}\text{-}k_{24}) > 5.7$, and changing k_{24} does not alter the droplet orientation. There is a first-order transition between radial and axial structures at a critical value of $WR/(2k_{11}\text{-}k_{24})$ of about 5.7, which is close to the result for equal constants. However, the lines do not overlap for $WR/(2k_{11}\text{-}k_{24})$ less than the critical value. In this region the values of $S_{||}$ and $S_{\perp}$ depend on the saddle-splay constant.

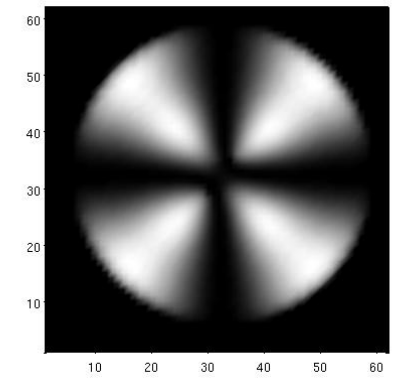

(a)

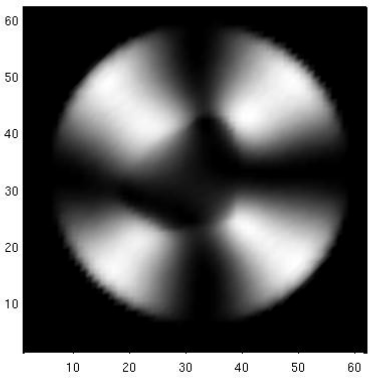

(b)

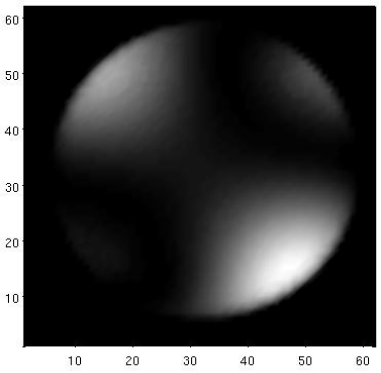

(c)

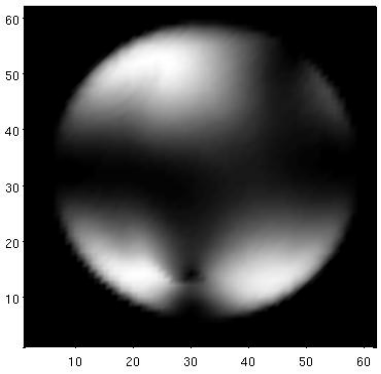

(d)

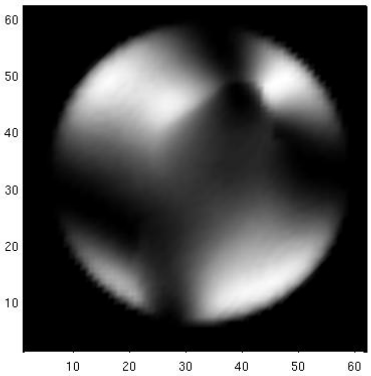

(e)

Fig. 3.19(a)-(e): Defect development and transition between locally stable radial configuration (computed at *WR/K*=1000) and equilibrium axial configuration at *WR/K*=5.1.

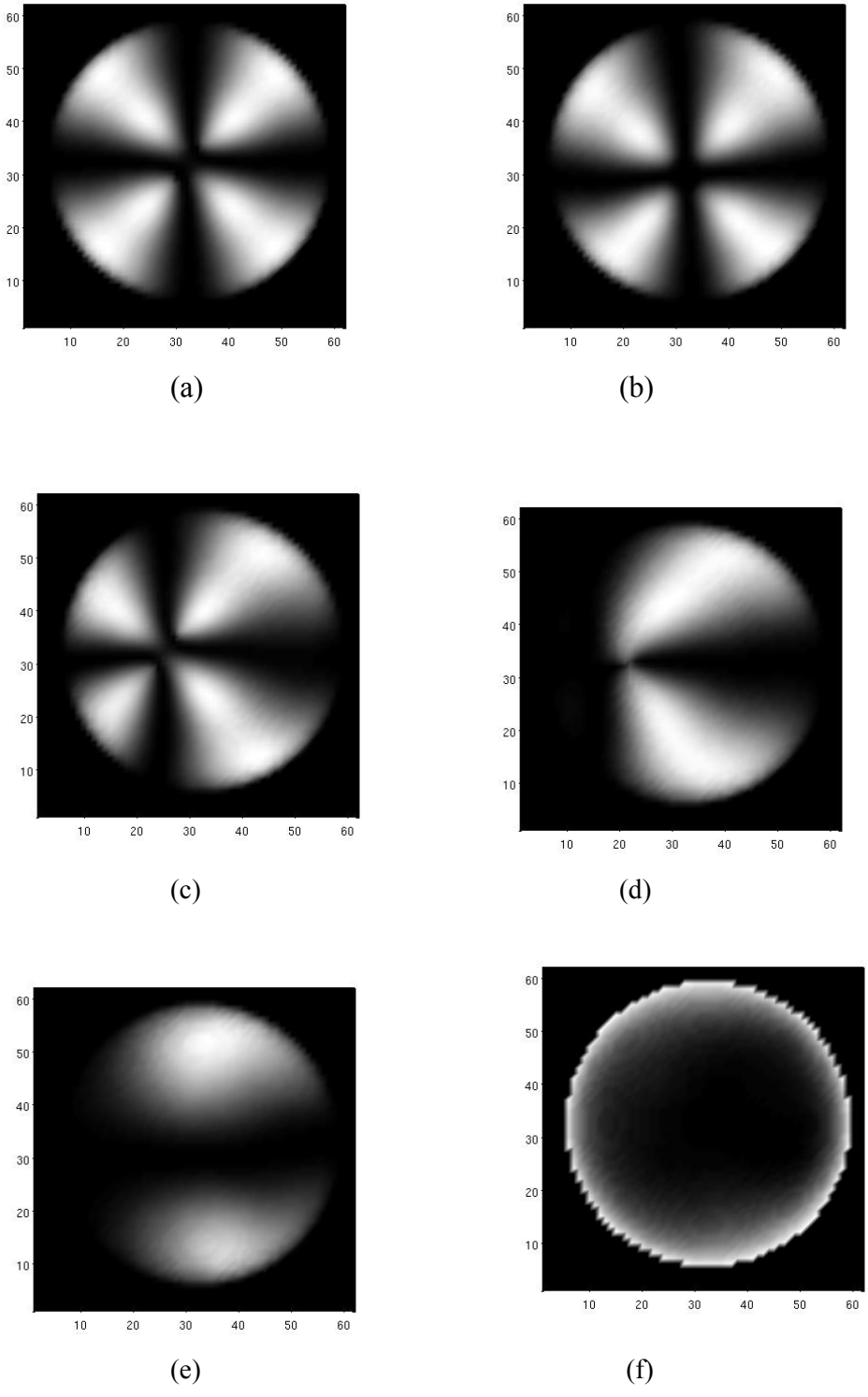

Fig. 3.20(a)-(f): Defect development and transition between locally stable radial configuration (computed at WR/K=1000) and equilibrium axial configuration at WR/K=0.6.

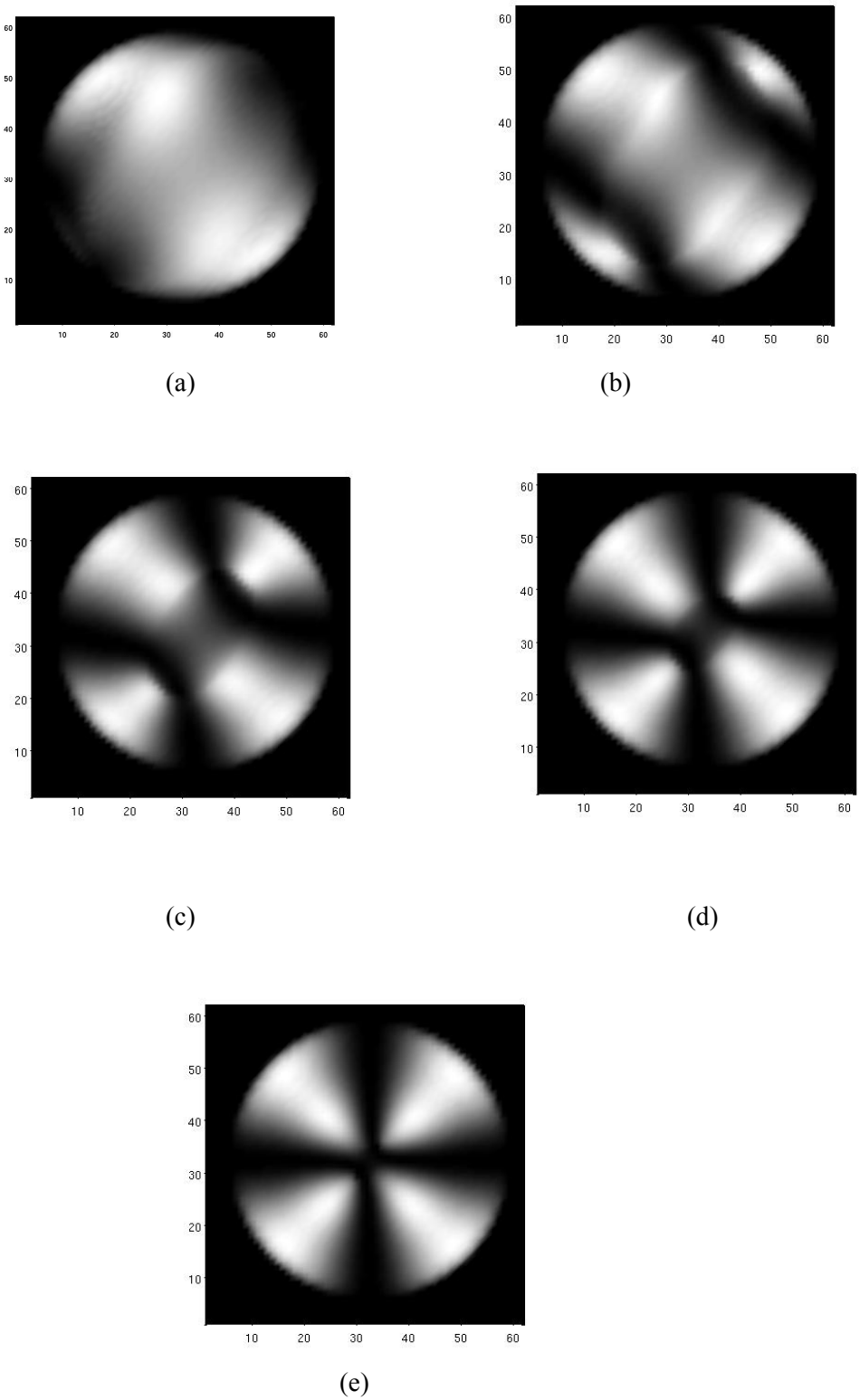

Fig. 3.21(a)-(e): Defect development and transition between locally stable axial configuration (computed at *WR/K*=5.4) and equilibrium radial configuration at *WR/K*=1000.

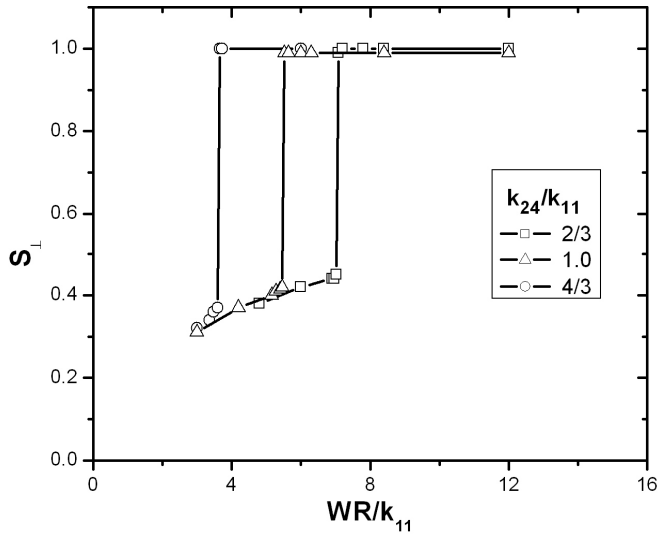

(a)

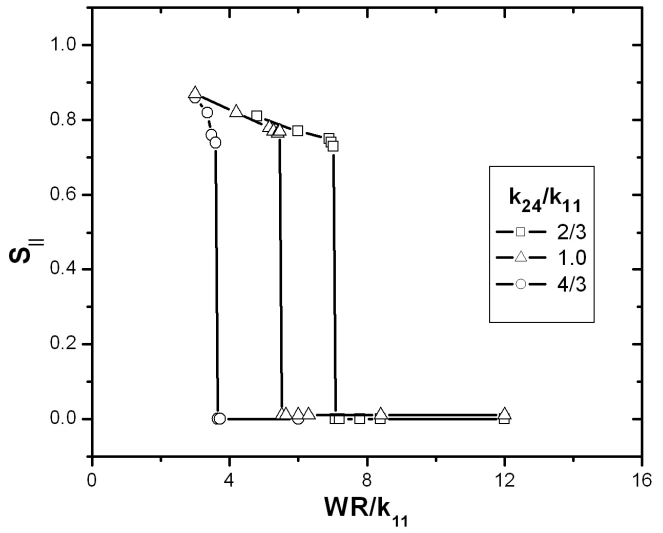

(b)

Fig 3.22: Order parameters $S_\perp$ and $S_{||}$ as functions of WR/k_{11} for different values of k_{24}.

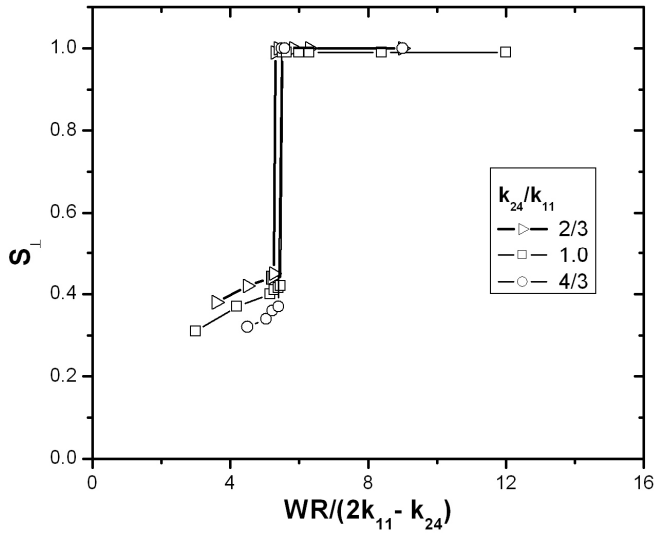

(a)

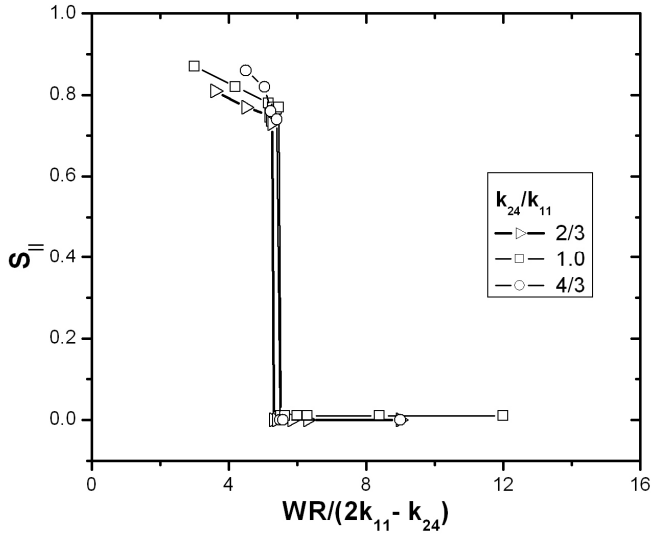

(b)

Fig 3.23 Order parameters $S_\perp$ and $S_\parallel$ as functions of $WR/(2k_{11}\text{-}k_{24})$ for different values of k_{24}.

Results for unequal elastic constants

To investigate the effect of unequal elastic constants on the droplet configuration, we performed simulations with the elastic constants of 5CB at room temperature: $k_{33}/k_{11} = 1.31$, $k_{22}/k_{11} = 0.51$, and $k_{24} = (k_{11}+k_{22})/2$.

The calculated order parameters $S_{||}$ and $S_{\perp}$ are plotted as functions of $WR/(2k_{11}-k_{24})$ in Figs. 3.24, together with the curves for equal elastic coefficients. The transition is broader, and the parallel and radial order before and after the transition is less perfect because of the presence of twist distortions, since $k_{22}/k_{11} < 1$. The minimum energy structures obtained in simulated annealing calculations starting from a random initial state in the region between the two dashed lines, roughly $4.5 < WR/(2k_{11} - k_{24}) < 7.3$, were not consistently reproducible and often reflected "escaped" structures that differed significantly from the parallel or radial morphologies computed at lower and higher values of $WR/(2k_{11} - k_{24})$. The simulated micrograph in Fig. 3.25b shows one realization for $WR/(2k_{11} - k_{24}) = 7.16$, for example, in which there is a substantial core region with an escaped structure. Radial orientation is always achieved from a random initial condition at $WR/(2k_{11} - k_{24}) = 7.8$, but it is distorted by twist, as shown in Fig. 3.25c. Some twist distortion persists even at extremely strong anchoring, as seen in Fig. 3.25d for $WR/(2k_{11} - k_{24}) = 21.7$. (In this case $S_{||}$=0.97, and $S_{\perp}$=0.05, which are slightly different from the parameters for equal constants, $S_{||}$=0.995, and $S_{\perp}$=0.001.) This result is expected, since the small ratio of twist to splay constants makes splay deformations energetically unfavorable. We obtain different orientations inside the droplet depending on the value of $WR/(2k_{11} - k_{24})$. Equilibrium orientation distributions are shown as vector plots in Fig. 3.26 for different values of $WR/(2k_{11} - k_{24})$.

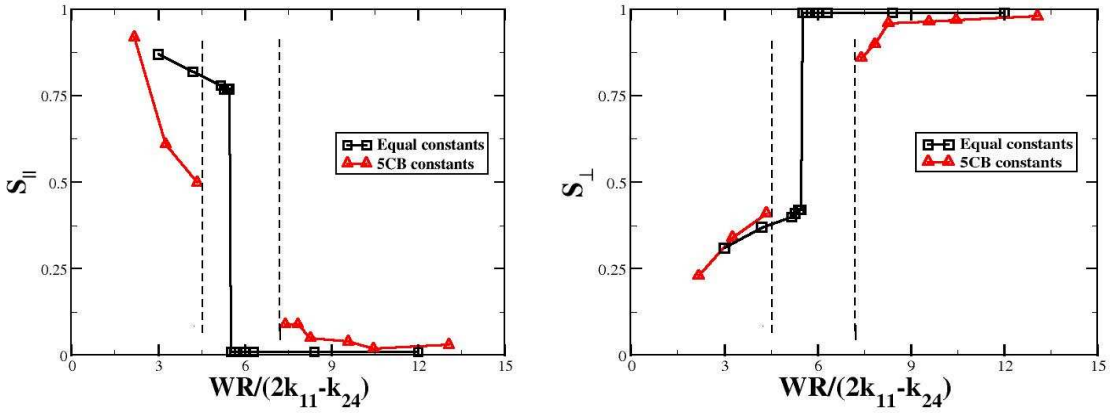

(a) (b)

Fig 3.24: $S_{\parallel}$ (a) and $S_{\perp}$ (b) as functions of anchoring strength parameter $WR/(2k_{11} - k_{24})$ for equal elastic coefficients and elastic coefficients characteristic of 5CB.

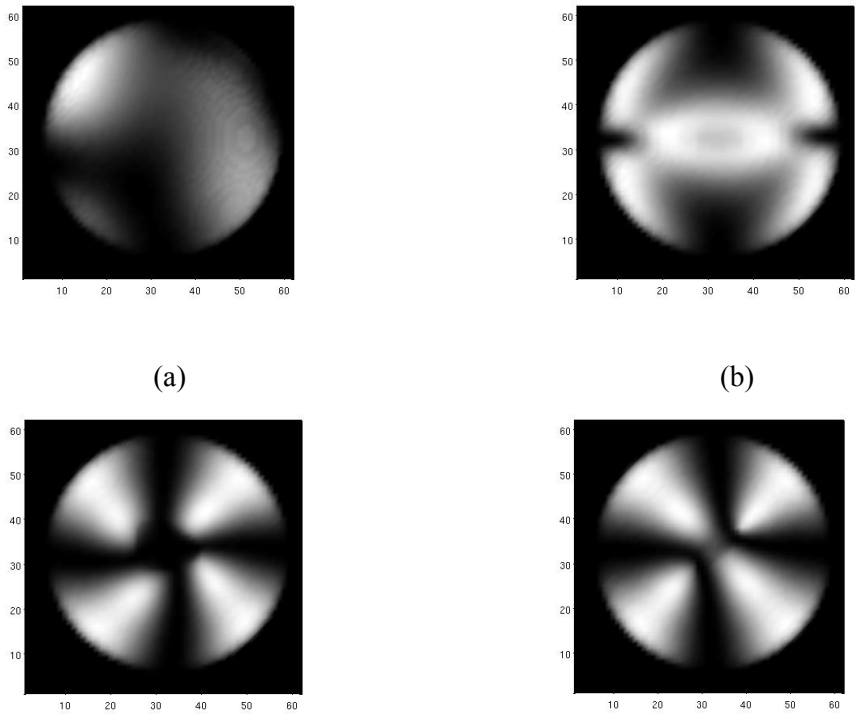

(a) (b)

(c) (d)

Fig. 3.25 (a)-(d): Optical micrographs for different values of $WR/(2k_{11}-k_{24})$. (a) $WR/(2k_{11}-k_{24})$ = 0.217, (b) $WR/(2k_{11}-k_{24})$= 7.16, (c) $WR/(2k_{11}-k_{24})$=7.8 and (d) $WR/(2k_{11}-k_{24})$=21.7.

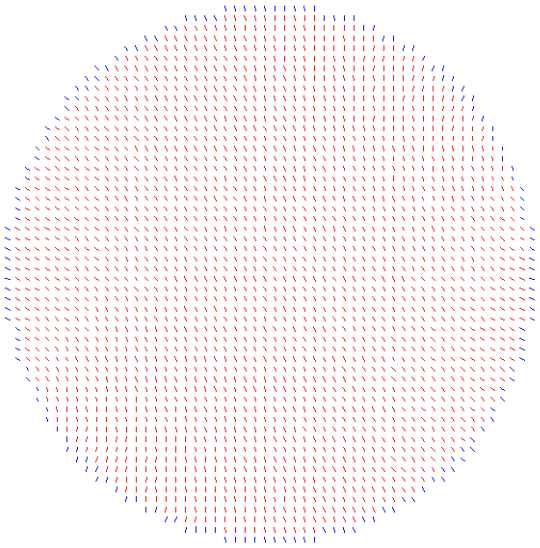

(a) $WR/(2k_{11}\text{-}k_{24})$ = 4.35

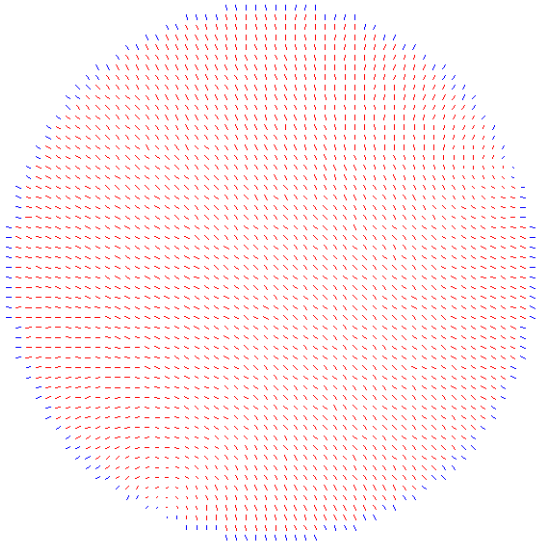

(b) $WR/(2k_{11}\text{-}k_{24})$ =6.53

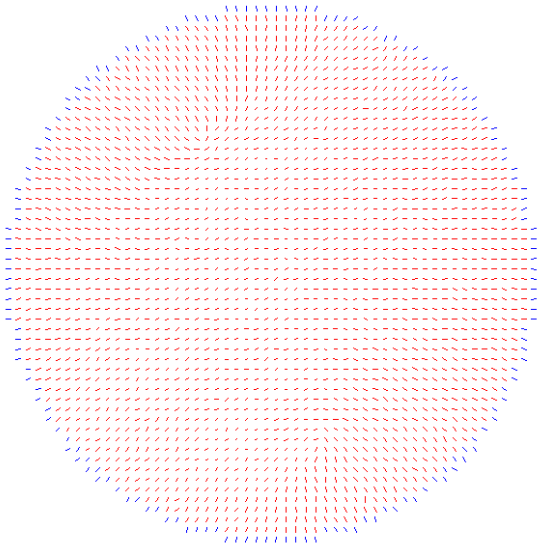

(c) $WR/(2k_{11}\text{-}k_{24})$ =7.62

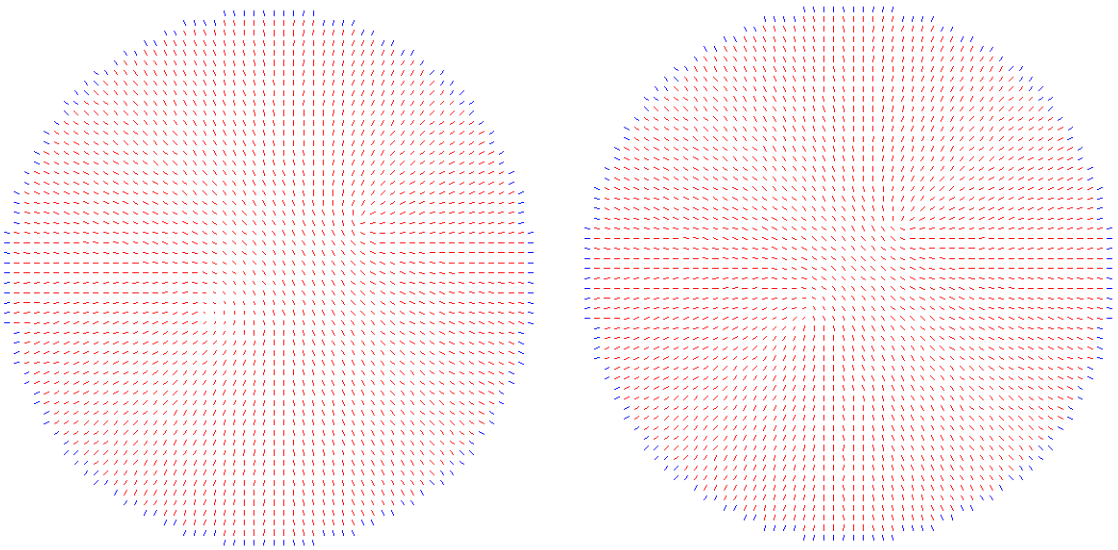

(d) $WR/(2k_{11}\text{-}k_{24})$ =8.06 (e) $WR/(2k_{11}\text{-}k_{24})$ =12.0

Fig. 3.26 (a)-(e): Radial section of droplet for different values of $WR/(2k_{11}\text{-}k_{24})$.

3.2 Results for spheroidal droplets

3.2.1 Minimum energy state calculations

In practical applications, droplets may deform to other geometries. An ellipsoidal geometry is likely to approximate the droplet shape in a flow field, for example. All three major axes in an ellipsoid are unequal; a spheroid is a simpler form of an ellipsoid where any two of the three major axes are equal. The ratio of the unequal length scales (ratio of large length scale to the small one) in a spheroid is known as the aspect ratio. We also define a deformation parameter D = (L – B)/(L + B) for our calculations, where L and B are the major and minor axes of the spheroid. (D=0.78 corresponds to L/B=8, for example.) This section focuses on calculations of spheroidal droplets.

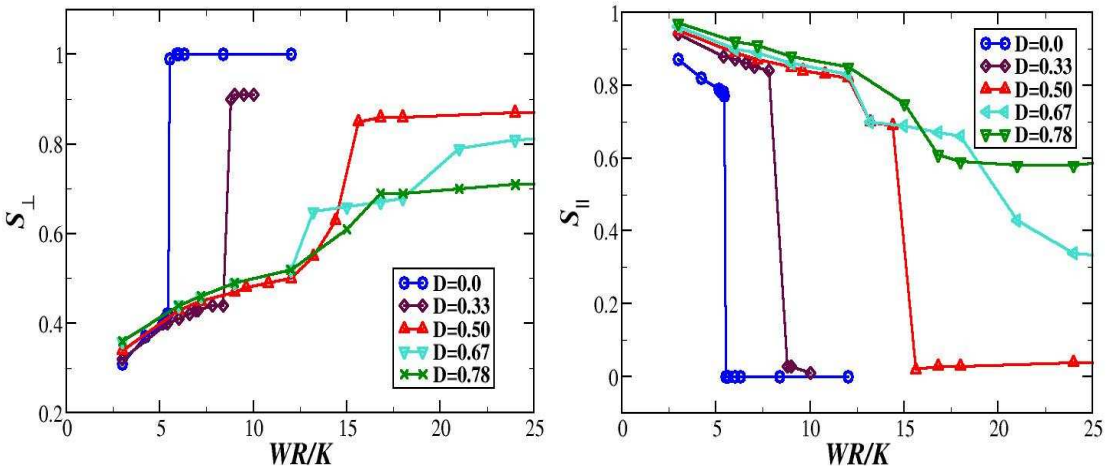

(a) (b)

Fig 3.27: Order parameters $S_\perp$ (a) and $S_{||}$ (b) as functions of WR/K for spheroidal droplets at various values of the deformation parameter D.

The parameters $S_{\perp}$ and $S_{||}$ with equal elastic coefficients are shown in Figs. 3.27 as functions of *WR/K* for various values of *D*. *R* is based on the radius of the sphere with the same volume (*N*=82696, *l*=0.1μm). The calculations were always started with a random initial configuration and a Monte Carlo Temperature *T** close to the isotropic-nematic transition. Both order parameters change in much the same way for small values of *D* as they do for spherical droplets, with the same first order axial-radial structure transformation at a critical value of *WR/K*. However, the peak value of $S_{\perp}$ in the radial regime decreases as *D* increases, and the critical value of *WR/K* required for the transformation also shifts towards higher values. The transition is gradual for large extensions (*D*=0.67 and 0.78).

The equilibrium orientation distributions in droplets with *D*=0.5 and *D*=0.78 are shown in Figs. 3.28 and 3.29 for weak and strong anchoring conditions. Corresponding simulated optical micrographs using the Jones matrix formalism for the director distribution are shown in Figs. 3.30 and 3.31. The optical micrographs for smaller *D* values are similar to those for spherical droplets, although the cross pattern is deformed in the spheroids. For spheroids with larger *D* values uniform axial structures are observed for low *WR/K*, and then the radial alignment is increased slowly as the parameter *WR/K* increases; hence the transition is gradual for large extensions. This is because the orientation distribution in a highly elongated droplet with strong homeotropic anchoring is nearly parallel over a large fraction of the droplet volume. $S_{||}$ and $S_{\perp}$ are nearly equal for *D* = 0.78 with strong anchoring.

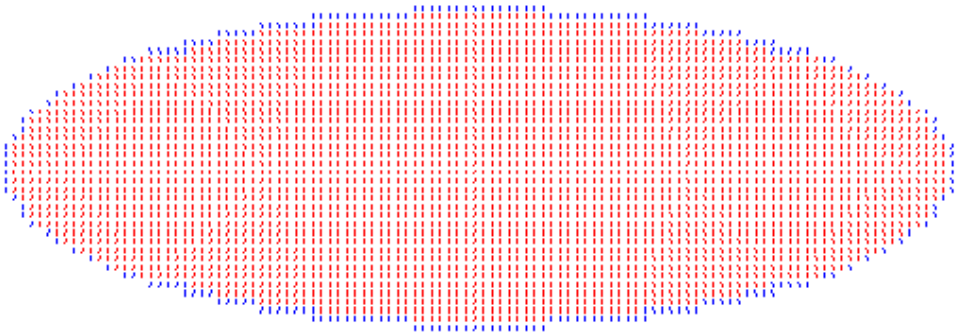

(a) *WR/K*=6.0

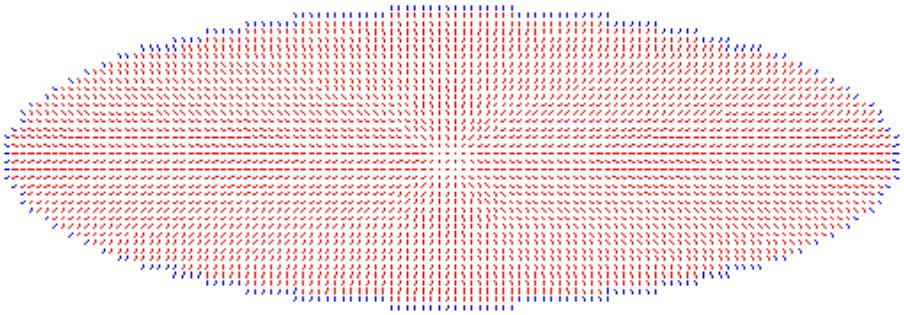

(b) *WR/K*=24.0

Fig. 3.28: Droplet configuration for a spheroidal droplet with *D*=0.5.

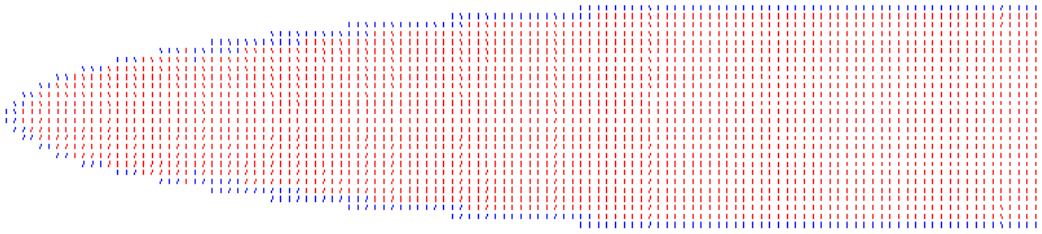

(a) *WR/K*=12.0

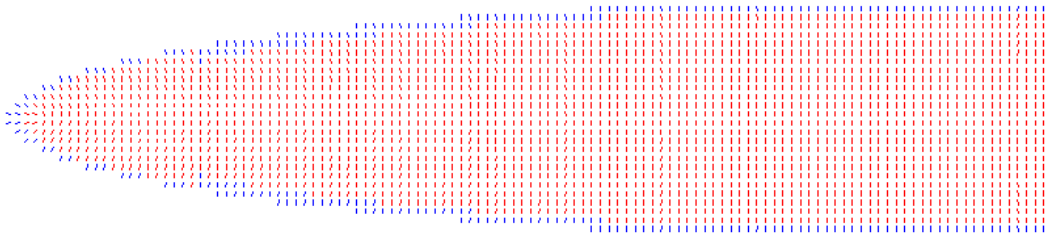

(b) *WR/K*=24.0

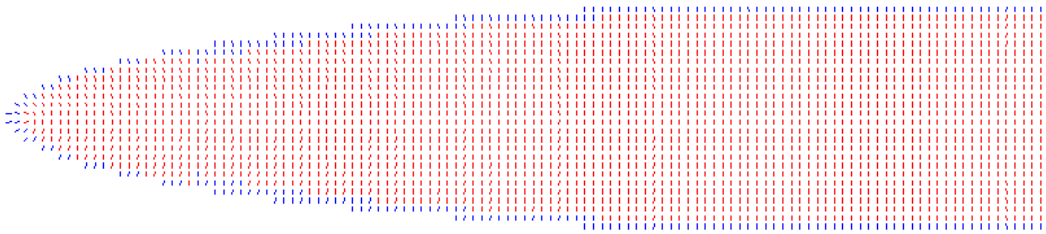

(c) *WR/K*=1000

Fig. 3.29 (a)-(c): Droplet configuration with different values of *WR/K* for a spheroidal droplet with deformation parameter *D*=0.78.

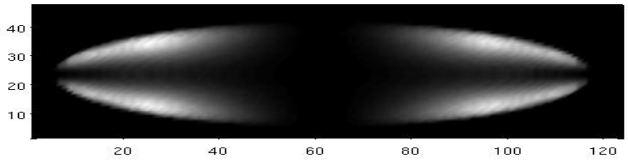

(a)

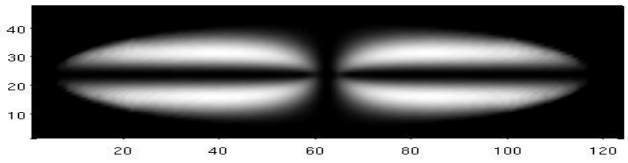

(b)

Fig. 3.30: Droplet configuration for a spheroidal droplet with deformation parameter D=0.5. (a) WR/K =6.0 and (b) WR/K =24.0.

(a)

(b)

(c)

Fig. 3.31: Droplet configuration for a spheroidal droplet with deformation parameter D=0.78. (a) WR/K =6.0, (b) WR/K =24.0, and (c) WR/K =1000.

3.2.2 Energy barrier for spheroids

As with spherical droplets, the system can become trapped in a local minimum in the energy surface and exhibit multiplicity. Such trapping could occur physically by, for example, deforming a sphere with homeotropic anchoring that has a radial orientation to a value of D such that a parallel orientation is the minimum energy state. (This would occur, for example, if a sphere with $WR/K = 10$ were to be deformed to a spheroid with $D \geq 0.67$.)

We have estimated the energy barrier between the local and global minima by initializing the system in the local minimum and then gradually increasing the Monte Carlo temperature until the transition occurs. Figure 3.32, for example, shows the structural evolution from a droplet with a parallel distribution [Fig. 3.32a] to the globally stable orthogonal distribution with a singularity at the center [Fig. 3.32c] for $WR/K = 30$ and $D = 0.5$. Figure 3.32b is an intermediate state that persists during the transition and seems to occupy a local minimum; here, two singularities separate orthogonal end regions from an essentially parallel center. The estimated energy barriers as functions of WR/K are shown in Fig. 3.33 for spheroids with D ranging from 0 to 0.78. The broken lines indicate small ranges of WR/K where the algorithm was not effective because of the absence of a large shift in the values of the order parameter pairs. The maximum transition energy is substantially reduced by elongation to aspect ratios of four or more ($D \geq 0.6$).

(a)

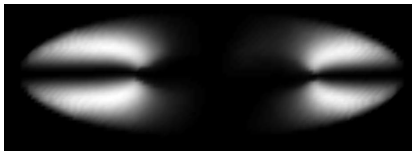

(b)

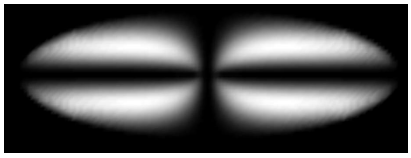

(c)

Fig. 3.32(a)-(c):Transition from a parallel conformation to the equilibrium orthogonal conformation, WR/K=30, D=0.5.

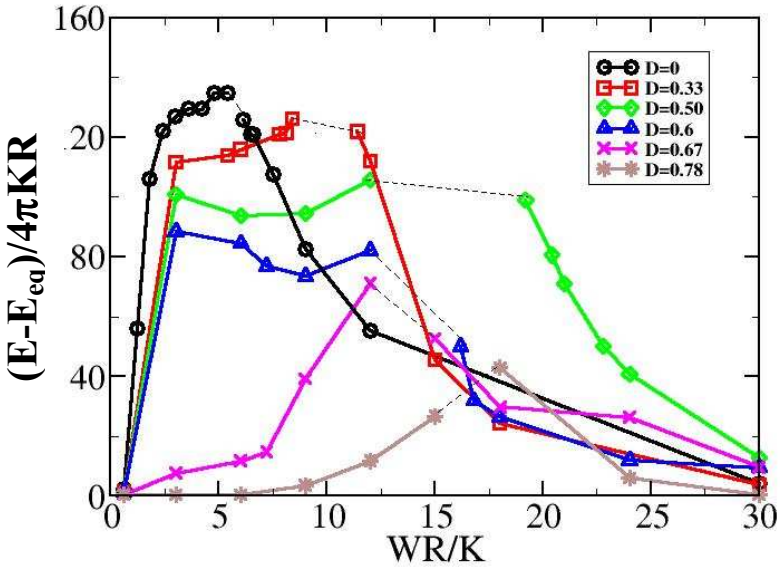

Fig. 3.33. Estimated energy barriers as functions of *WR/K* for spheroids with various values of *D*.

The structural evolution from a radial conformation to the equilibrium parallel orientation at very strong anchoring is shown in Fig. 3.34 when a sphere with radial orientation is deformed to a spheroid with *D*=0.78. In this case the center singularity from the radial spherical droplet separates into two singularities that migrate to the ends during the transition to the parallel orientation. The reverse process is observed when a spheroid with *D*=0.78 and parallel orientation is deformed to low-*D* spheroids such that the radial orientation is the equilibrium state; depending on the value of *D*, evolution follows a path as shown earlier in Fig. 3.20 or 3.21 (*D*=0) or Fig. 3.32 (*D*=0.5). The estimated energy barriers as functions of *D* for these transformations are shown in Fig. 3.35; the energy barrier does not depend on *D* when passing from a radial to a parallel conformation (low *D* to *D*=0.78), but it increases with *D* in the reverse process.

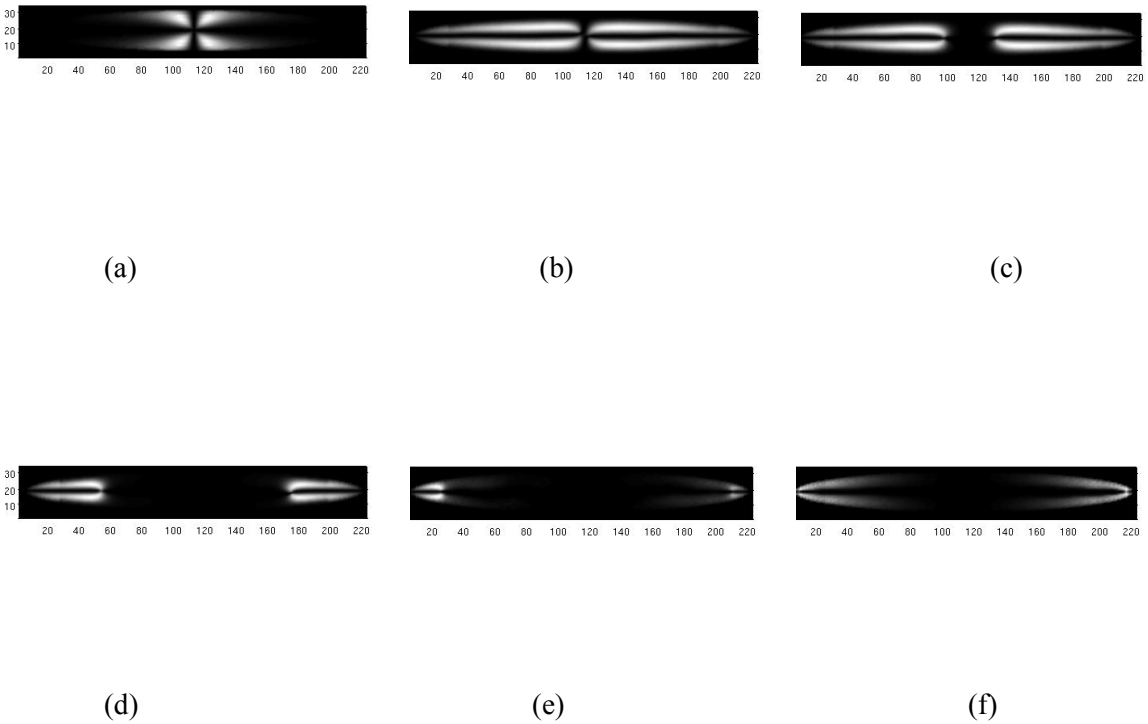

Fig. 3.34(a)-(f): Transition from a radial conformation to the equilibrium parallel conformation. A spherical droplet with radial conformaiton is deformed into a spheroid with D=0.78 and WR/K=30.

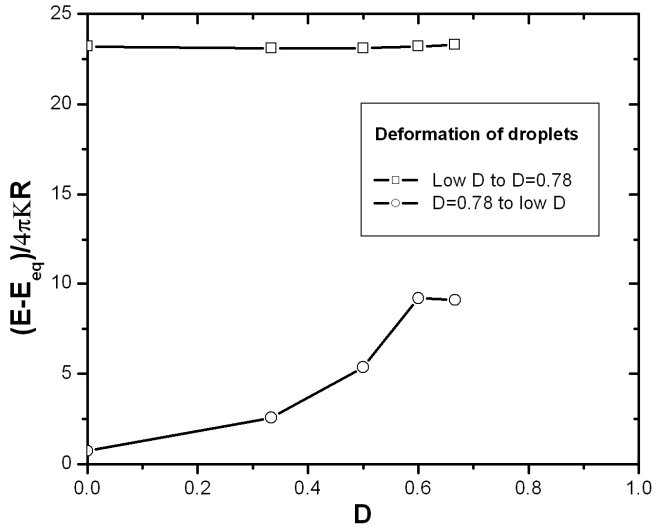

Fig. 3.35. Estimated energy barriers as a function of D passing from/to a low D spheroid (radial conformation) to/from D=0.78 (parallel orientation).

3.3 Summary

Our approach allows free choice of the elastic constants (splay, $k_{11;}$ twist, k_{22}; bend, $k_{33;}$ and saddle-splay, k_{24}) in the Frank free energy expression, as well as the surface anchoring strength W in the Rapini/Papoular surface anchoring energy. The simulation results establish the morphological richness of these droplets, even in the approximation of equal elastic coefficients (k_{11}= k_{22}= k_{33}= k_{24}=K). A first-order transition from an axial conformation induced by the bulk nematic potential over most of the droplet to a radial conformation induced by the strong surface anchoring is observed in a spherical droplet of radius R for equal bulk constants (k_{11}= k_{22}= k_{33}) when the dimensionless anchoring strength parameter $WR/(2k_{11}- k_{24})$ exceeds a value of 5.9. A scaling argument based on a transition between perfectly parallel and radial alignments predicts a transition at a value

of $WR/(2k_{11}- k_{24})$ of order 3, which is acceptably close to the computed transition. The transition is broader if the Frank elastic coefficients are unequal. A similar transition occurs at a critical elongation of a deforming droplet. Indeed, affine deformation of a sphere will lead to alignment that is nearly orthogonal to the surface of the spheroid throughout much of the bulk for a sufficiently large aspect ratio (aspect ratio ≥ 5.0). This is borne out by the degree of parallel ordering exhibited at large deformations for large values of the dimensionless anchoring strength parameter *WR/K*, where substantial deviation from parallel ordering transverse to the axis of elongation is restricted to tip regions.

Multiple steady states that are separated by finite energy barriers exist for spherical and spheroidal droplets with homeotropic anchoring over the entire range of the dimensionless parameter *WR/K*, with maximum transition energy densities of the order of 2,000 J/m^3 (Pa) for a typical liquid crystalline droplet with a spherical radius of 1μm. The transition energy density decreases with elongation to aspect ratios of four or more, indicating that elongation is favored to drive surface-induced transitions.

Chapter 4
Results for Cylinders

In Chapter 3 we explored the orientational morphologies of spherical and spheroidal droplets of nematic liquid crystals using a simulated annealing approach, with particular attention to bistability, the transitions between locally stable states, and the energy barriers for such transitions. Here, we extend this approach to liquid crystalline cylinders and to the development of pathways by which a liquid crystalline cylinder might break up into droplets. Motivation for this work comes from earlier work of Inn and Denn [32], as discussed in Sec. 1.4.

The breakup of cylinders of isotropic liquids into droplets is driven by interfacial tension. Rayleigh first showed that an infinitely long circular comprising an incompressible Newtonian liquid will break up into spherical droplets if the wavelength of infinitesimal sinusoidal perturbations is larger than some minimum value, equal to the periphery for an inviscid liquid; the problem is addressed in detail by Chandrasekhar [60]**.** Tomotika [61] analyzed capillary instabilities in an isotropic viscous matrix, including the effect of the fiber-to-matrix viscosity ratio. Rey [62-64] recently studied the stability of incompressible nematic fibers, taking into account the nematic orientation and the matrix-to-fiber viscosity ratio. Our approach differs from the classical treatment of

stability, in that we assume that any breakup will occur because of finite sinusoidal disturbances of the nematic cylinder, and we calculate the equilibrium free energies of the perturbed states. In this way we can define feasible pathways by which a transition from cylinder to droplets can occur through a monotonic decrease in free energy, and we can determine any energy barriers that must be overcome along such a path.

Our overall approach in seeking to understand transitions from cylindrical liquid crystalline structures to spherical droplets is to follow the morphology and free energy through a series of shapes, from cylinder to increasingly perturbed cylinder to spherical droplet, seeking paths through which the equilibrium free energy continuously decreases. We have previously studied spherical droplets with a preferred orthogonal surface orientation [Chapter 3]. In this chapter, we study the effect of various parameters such as *WR/K*, wavelength of perturbation, perturbation amplitude, etc., on director orientation in both perturbed and unperturbed (circular) cylinders. We also explore the possibilities of multiplicity and energy barrier requirements in cylindrical droplets.

4.1 Cylindrical droplets

4.1.1 Equal elastic coefficients

We first discuss results for a circular cylinder with equal elastic coefficients. Periodic boundary conditions were established at the open ends of the cylinder, and we used random initial conditions for the director and an initial MC temperature close to the Isotropic-Nematic transition to permit large fluctuations. The calculated total free energy normalized by $2\pi KL$ (Eq. 1.10b for $WR/K \rightarrow \infty$) is shown in Fig. 4.1 as a function of WR/K for cylindrical cavities with different length/radius (L/R) ratios. (The number of

lattice cells scales linearly with *L/R*; *L/R* = 5 requires 124696 cells.) There is clear convergence with respect to length of the cylinder, and there is a sharp change in free energy at a value of *WR/K* of about 7. A planar-polar structure is obtained for low *WR/K*, as expected, while strong anchoring exhibits a planar-polar structure with two line defects (*PPLD*) near the interface. Simulated optical micrographs of the equilibrium orientation distributions below and above the transition are shown for *WR/K* = 4.44 and 1000 in Figs. 4.2 and 4.3, respectively.

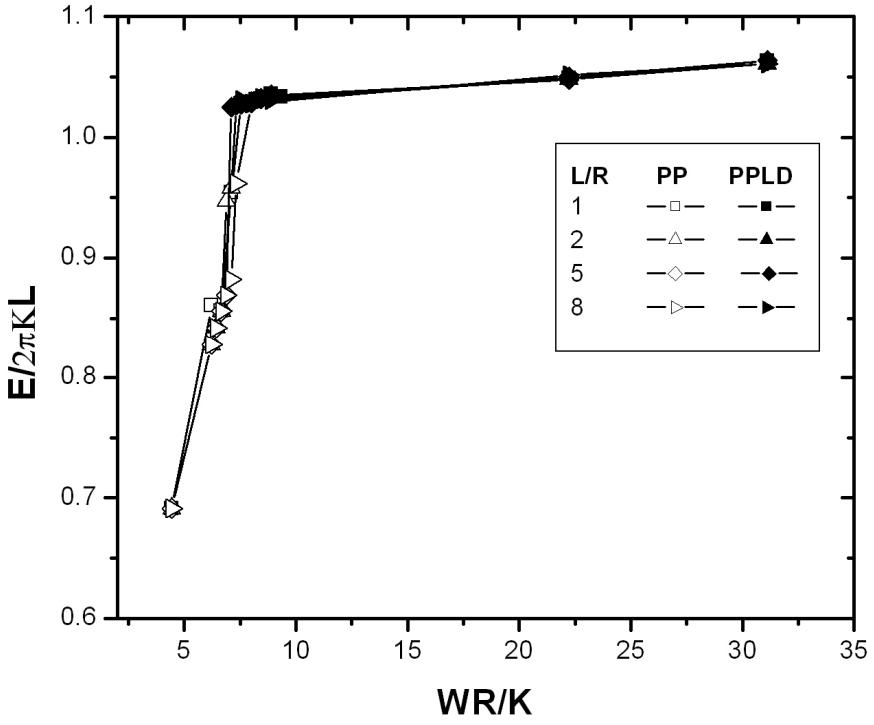

Fig 4.1. Total free energy for unperturbed cylinders when simulations are started with random initial state.

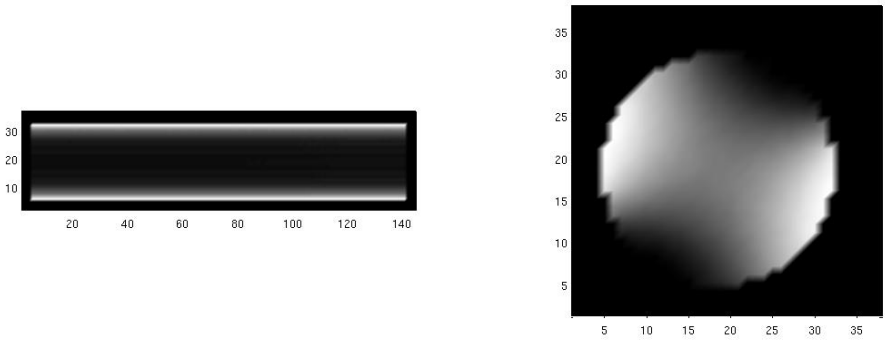

(a) (b)

Fig. 4.2: Simulated optical micrographs in nematic cylinders for *WR/K*=4.44. (a) Planar-polar orientation when light propagates perpendicular to the cylindrical axis and (b) Planar-polar orientation when light propagates along the cylindrical axis.

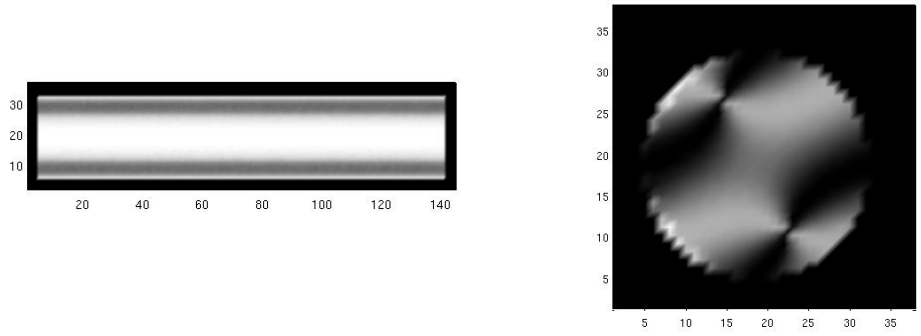

(a) (b)

Fig. 4.3: Simulated optical micrographs in nematic cylinders for *WR/K*=1000. We obtain planar-polar orientation with two defects when simulations are started with random initial state. (a) Optical image when light propagates perpendicular to the cylindrical axis and (b) when light propagates along the cylindrical axis.

The computed normalized energy for the PPLD structure for large *WR/K* is higher than the asymptotic value of unity given by Eq. 1.10b for the escape radial structure. We were unable to obtain an ER structure with our simulated annealing algorithm starting from random initial conditions. A similar observation was made by Smondrev and Pelcovits [65] and Chicoli et al [66] in Monte Carlo simulations of the analogous molecular theory. It appears that the system always becomes trapped in a local minimum.

The free energies computed using the analytical expressions for PP and ER orientations as initial conditions, with low Monte Carlo temperatures to keep fluctuations small, are shown in Fig. 4.4. The PP structure is still found to be energetically favorable for small values of *WR/K*, while the ER structure is favored for large values of *WR/K*. A simulated optical micrograph of the ER configuration for *WR/K* = 20 is shown in Fig. 4.5, and a vectorial representation is shown in Fig. 4.6. The escape line along the cylindrical axis is evident in the vector diagram. The intensity of escape is high close to the cylinder axis but decreases as we move towards the boundary. The calculated order parameters S_{ER} and $S_{||}$ corresponding to the minimum energy states are shown in Fig 4.7. The critical *WR/K* at the transition between ER and PP morphologies lies between 8.44 and 8.89, which is close to the analytical value of 8.65 obtained in Sec. 1.4. (As shown in Fig. 4.1, the algorithm predicts a PP-PPLD transition at about *WR/K* = 7, so we might expect to find PPLD structures for *WR/K* between 7 and 8.65.)

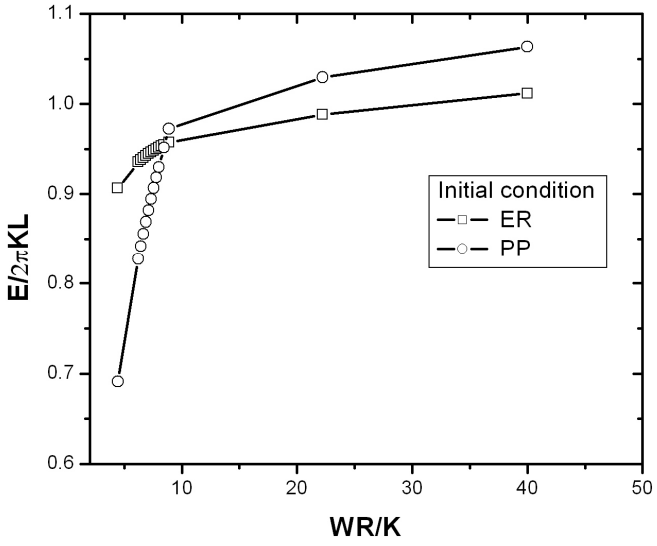

Fig. 4.4: Energy comparison and calculation of minimum energy state for unperturbed cylinders.

(a) (b)

Fig. 4.5: Simulated optical micrographs for escaped-radial orientation in nematic cylinders for *WR/K*=20. (a) Optical image when light propagates perpendicular to the cylindrical axis and (b) when light propagates along the cylindrical axis.

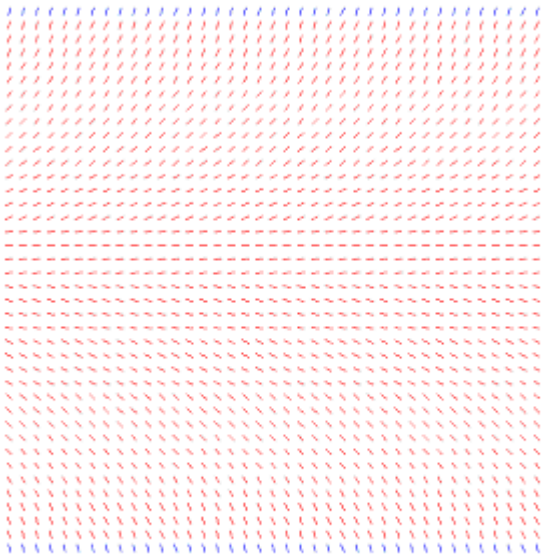

Fig. 4.6: Escaped-radial orientation with $WR/K = 20$. We make a cut at the center of cylinder and in the plane of cylindrical axis.

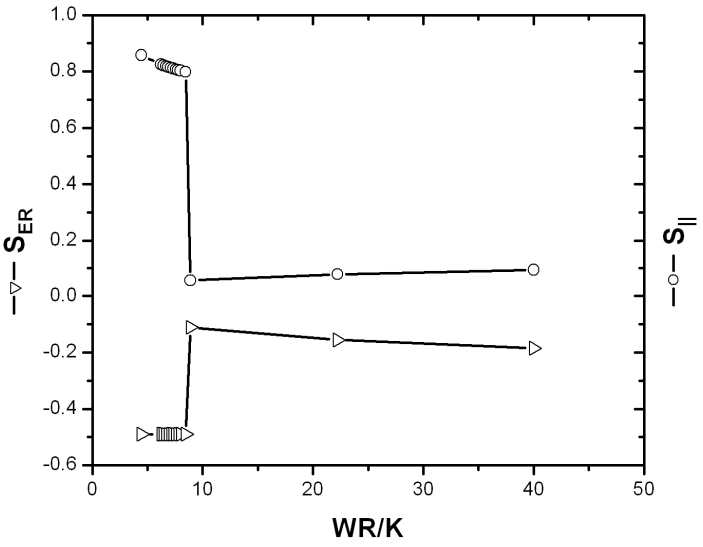

Fig. 4.7: Order parameters corresponding to minimum energy state for unperturbed cylinders.

4.1.2 Multiplicity

We have found orientational multiplicities in cylinders similar to those observed in spheroids [Chapter 3] by starting simulated annealing calculations with an ER distribution when *WR/K* is less than the transition value and with a PP distribution when *WR/K* is greater than the transition value, always keeping the Monte Carlo temperature small. In such cases we obtain convergence to a local minimum in the free energy; in the former case the local minimum free energy state is escaped-radial, while in the latter it is a PP state with increasing distortion as *WR/K* is increased. As with the spheroids, we have estimated the energy barrier between the local and global minima by initializing the system in the local minimum and then gradually increasing the Monte Carlo temperature until the transition occurs. The sequence of states in the S_{ER}-$S_{\perp}$ plane in passing from a locally stable ER configuration to the globally minimal PP state, together with the corresponding free energies as a three-dimensional curve, are shown in Fig. 4.8 for *WR/K* = 4.44, and simulated micrographs of the transition states are shown in Fig. 4.9. The transition from the escaped radial structure initiates at one end of the cylindrical computational domain and propagates axially. The sequence is different during a transition from escaped-radial to planar-polar with weak anchoring [Fig. 4.10]; in this case the escaped-radial structure first transforms into a parallel orientation along the cylinder axis. We could not carry out the corresponding calculation from PP to ER because the system always went to a PPLD orientation, as noted above.

The estimated energy barrier is shown as a function of *WR/K* in Fig. 4.11 for transitions from a locally stable ER configuration to the minimizing PP configuration. The maximum corresponds to an energy density of about 550 J/m^3 (Pa) for a typical

elastic coefficient of $5x10^{-12}$ N and a cylinder with a radius of 1μm. This energy density is less than that for the transition between radial and aligned configurations in spheres, but it is comparable to the computed barrier for elongated spheroids [Sec. 3.2.2].

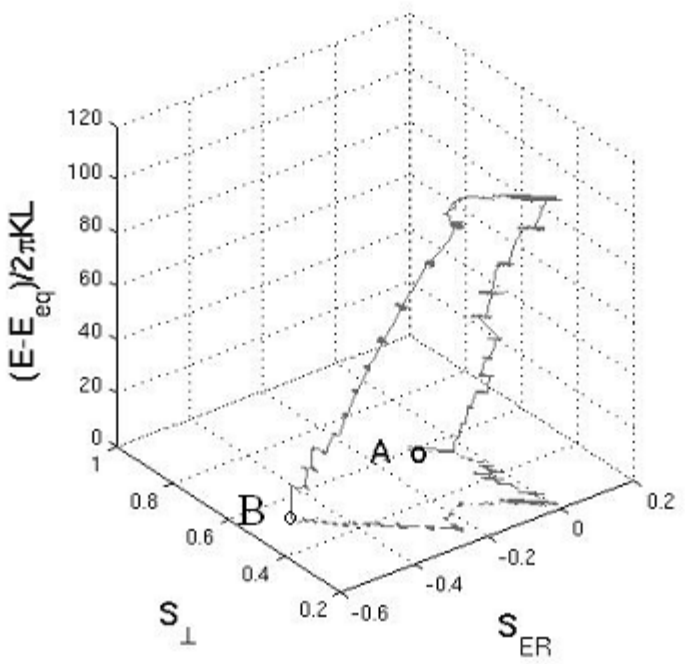

Fig. 4.8: Path in conformation space and corresponding energy in passing from a locally stable escaped-radial (A) to the planar-polar free energy minimum state (B).

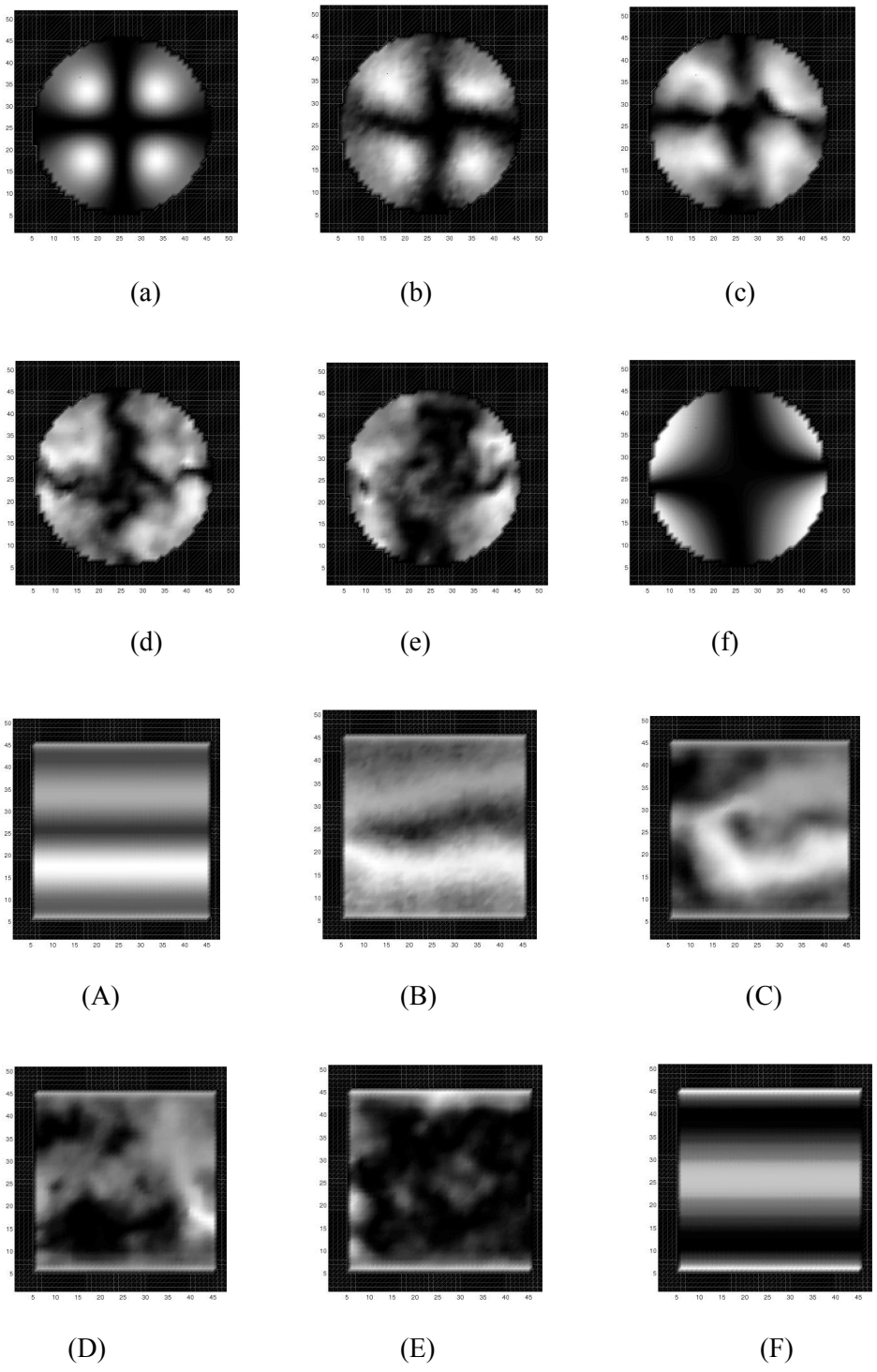

Fig. 4.9: Defect development during the transition from a locally stable ER conformation to the equilibrium PP conformation, *WR/K*=4.44. (a)-(f) Images when light propagates along the cylindrical axis and (A)-(F) when light propagates perpendicular to the cylindrical axis.

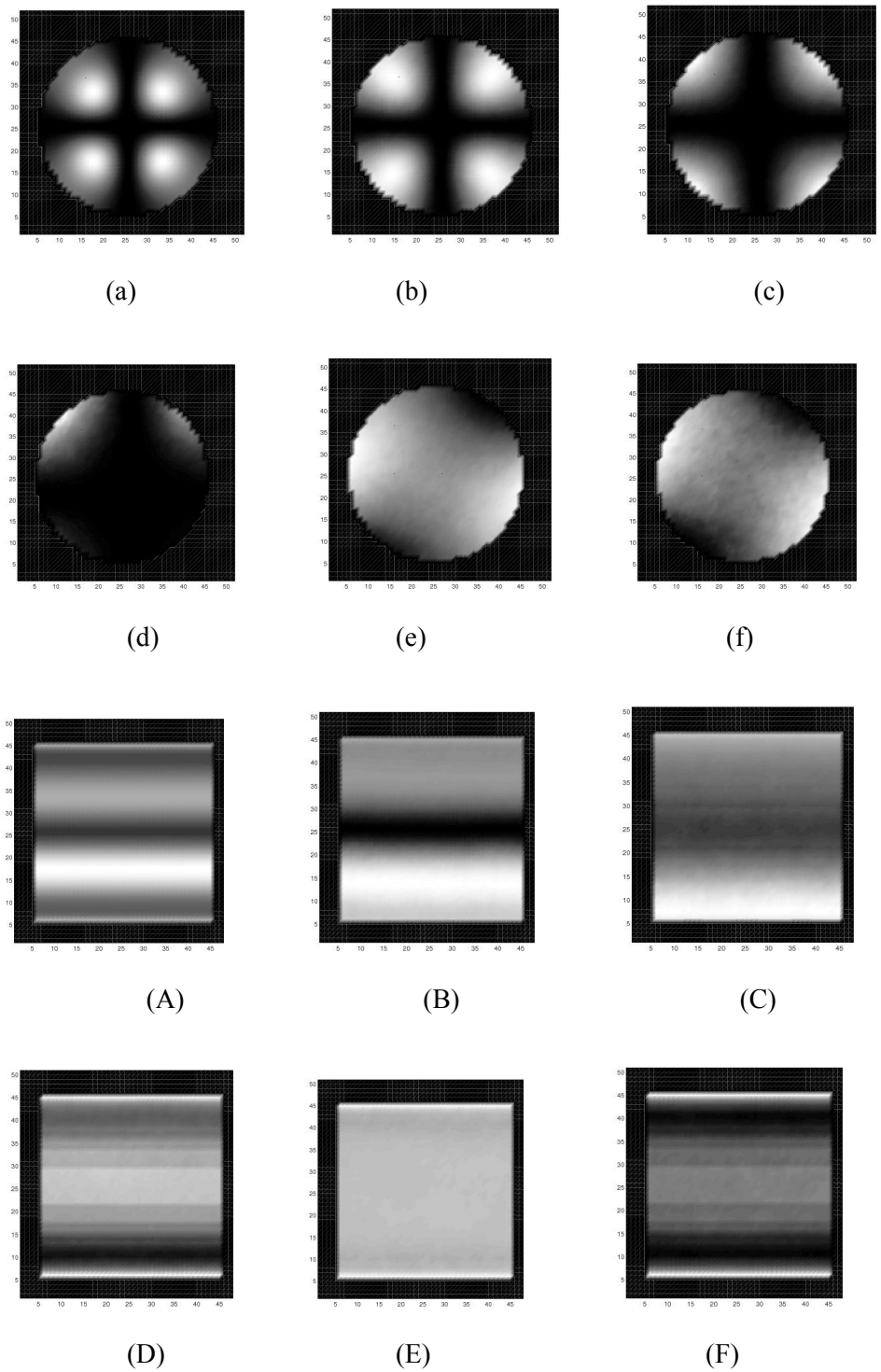

Fig. 4.10: Defect development during the transition from a locally stable ER conformation to the equilibrium PP conformation, *WR/K*=0.89. (a)-(f) Images when light propagates along the cylindrical axis and (A)-(F) when light propagates perpendicular to the cylindrical axis.

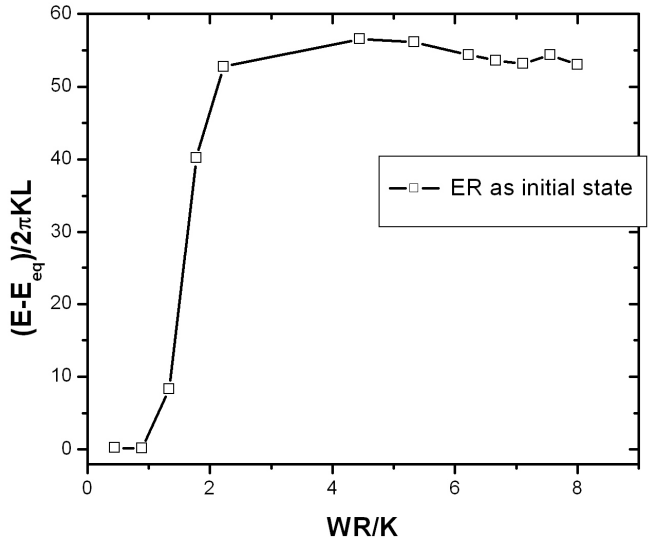

Fig. 4.11. Estimated energy barrier as a function of *WR/K*.

4.1.3 Unequal elastic constants

We have examined the effect of unequal coefficients on director orientation in nematic cylinders, using elastic constants typical of 5CB at room temperature: k_{33}/k_{11} = 1.31, k_{22}/k_{11} = 0.51, and k_{24} = $(k_{11}+k_{22})/2$. We initiated the simulations with both plane parallel and escaped-radial orientations, comparing the energies of the converged states to determine the minimum. The overall features of the computations are similar to those for equal elastic constants, as seen in Fig. 4.12. Bend distortions in the PP orientation are small relative to the equal constant case because of the relatively large value of the bend elastic coefficient. The radial order parameter $S_{\perp}$ for $WR/(2k_{11} - k_{24})$ = 8.03, where the PP orientation is the minimizing state, is only 0.21, for example, compared to a value of 0.60 for equal constants.

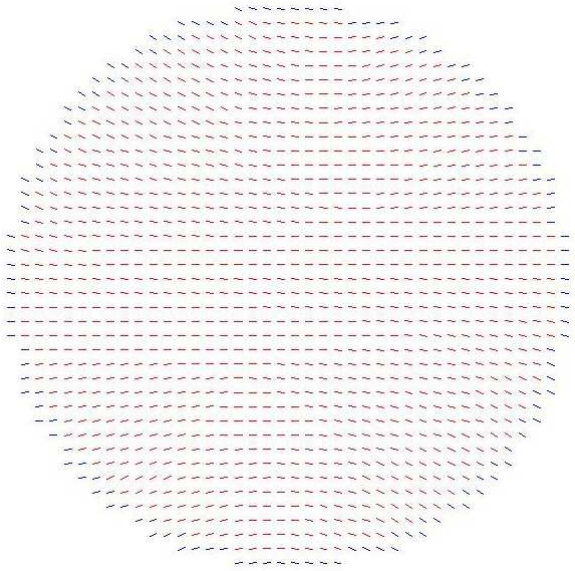

(a)

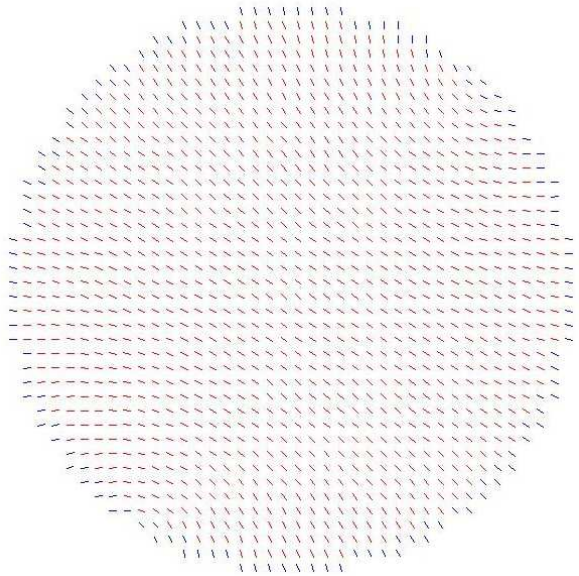

(b)

Fig. 4.12. Director orientation for unequal constants with $WR/(2k_{11} - k_{24}) = 1.606$ (a) and $WR/(2k_{11} - k_{24}) = 8.03$ (b).

4.2 Perturbed cylinders

4.2.1 Minimum energy morphologies

We now consider perturbed cylinders with radii of the form $R(z) = R_0 + b\sin(2\pi z/\lambda)$, where z is measured along the cylindrical axis [Fig. 4.13]. R_0 is the radius of the unperturbed cylinder, b is the perturbation amplitude, and λ is the wavelength of the perturbation. The ratio b/R_0 defines the magnitude of the relative perturbation; when $b/R_0 = 1$ we presume that the cylinder has broken up into droplets.

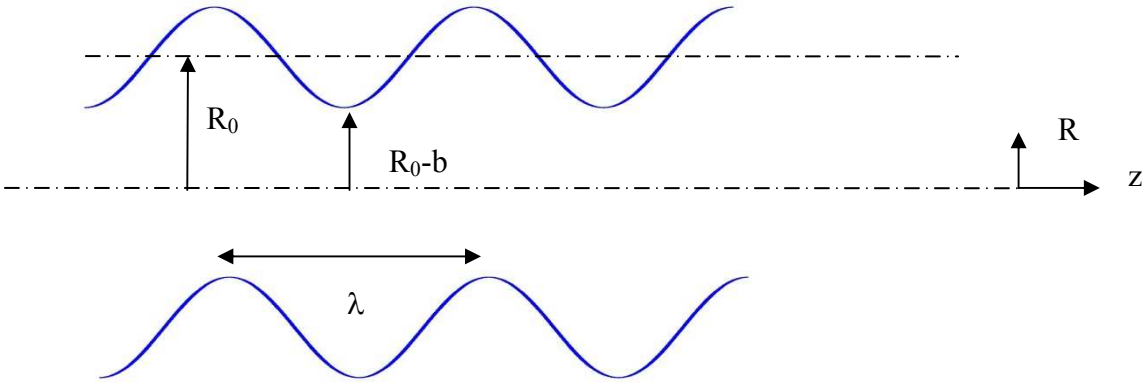

Fig. 4.13: Shape of the cylindrical filament. We consider filaments of sinusoidal form.

We carried out simulated annealing calculations for different values of λ and b using a variety of starting orientations: parallel to the cylinder axis, parallel in the orthogonal plane, deformed escaped-radial (obtained by an affine transformation of a cylinder with an escaped-radial orientation), and deformed spherical radial, with a singularity on the cylinder axis at the center of the cycle. The calculated escaped-radial order parameters S_{ER} corresponding to the minimum energy states are shown as functions of WR_0/K in Figs. 4.14a,b, and c for $\lambda/R_0 = 1$, 2, and 5, respectively, and various values of

b/R_0. For small perturbation amplitudes or long wavelengths the perturbed and unperturbed cylinders have the same morphologies: weak anchoring favors a PP orientation while strong anchoring favors an ER orientation. With increasing perturbation amplitude there is a transition at long wavelengths to a deformed radial orientation, while at shorter wavelengths the dominant orientation is parallel to the cylinder axis except near the interface. Typical simulated optical micrographs are shown in Figs. 4.15 for very strong anchoring (WR/K = 1000); the similarity between the deformed radial structure in Fig. 4.15c for λ/R_0 = 5 and b = 0.75 and the radial orientation in a sphere shown in Fig. 3.6a is evident.

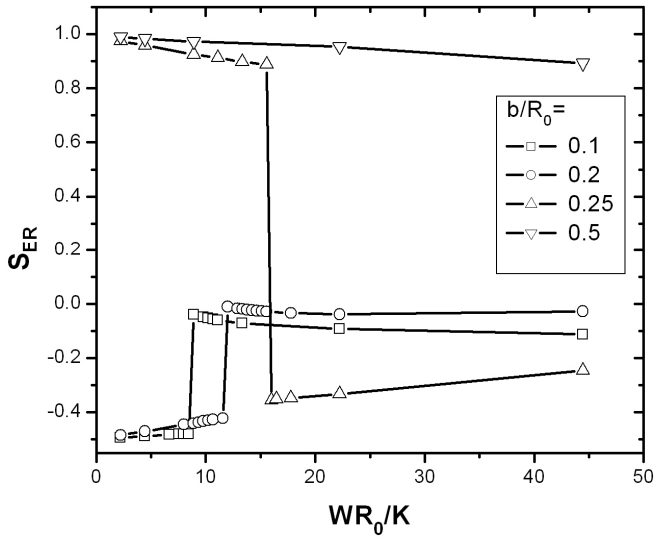

(a)

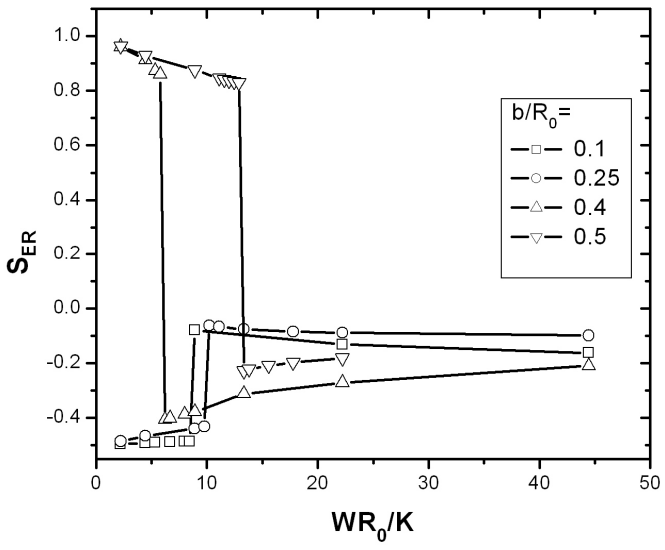

(b)

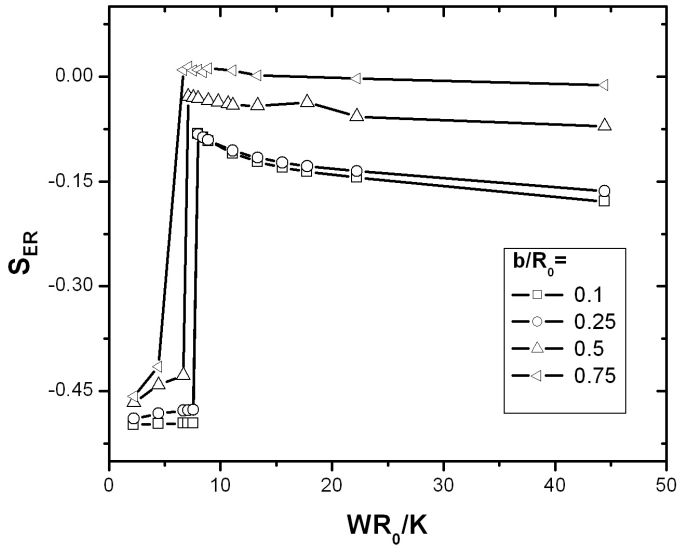

(c)

Fig. 4.14: Escaped-radial order parameter as a function of *WR/K* for perturbed cylinders. (a) $\lambda/R_0 = 1$, (b) $\lambda/R_0 = 2$, and (c) $\lambda/R_0 = 5$.

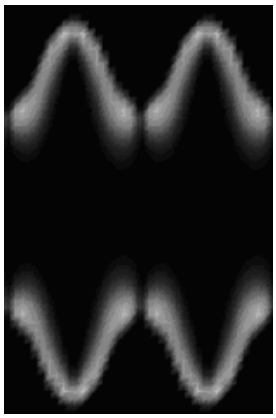

(a)

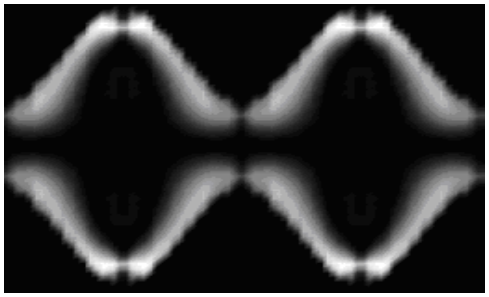

(b)

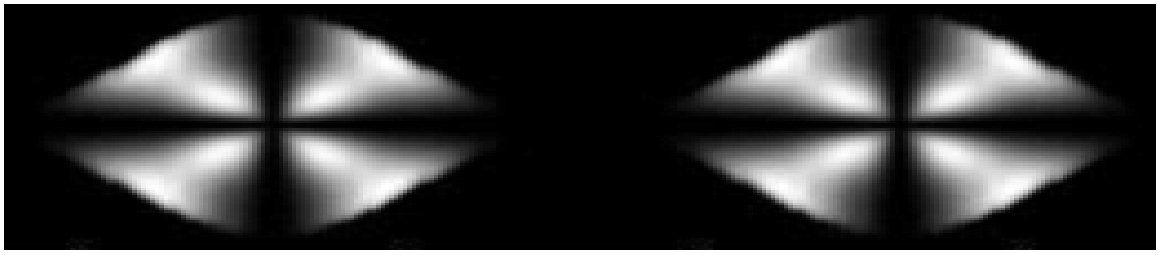

(c)

Fig. 4.15: Optical micrographs for perturbed cylinders with fixed anchoring at the surface. (a) $\lambda/R_0 = 1$, $b/R_0 = 0.3$ (b) $\lambda/R_0 = 2$, $b/R_0 = 0.5$, and (c) $\lambda/R_0 = 5$, $b/R_0 = 0.75$.

We plot the normalized minimum free energy of deformed cylinders as functions of the perturbation magnitude in Fig. 4.16 for WR_0/K = 1000. The free energy increases with increasing perturbation amplitude for small wavelength disturbances ($\lambda/R_0 \leq 3$), hence such disturbances should not grow. The free energy *decreases* with increasing perturbation amplitude for cylinders with long wavelength disturbances ($\lambda/R_0 \geq 4$), however, indicating that perturbation growth is energetically favored and that the nematic cylinders should break up into droplets. The normalized energies are plotted as functions of WR_0/K in Figs 4.17a and b for λ/R_0 = 3 and 4, respectively, together with the free energy of a sphere having the volume contained in one wavelength. For strong anchoring, where the minimum energy state for the cylinder is escaped-radial, breakup into spheres is always favored energetically, but a feasible path with monotonically decreasing free energy is possible only for the larger wavelength. A cylinder with weak anchoring is energetically more favorable than the equivalent spheres.

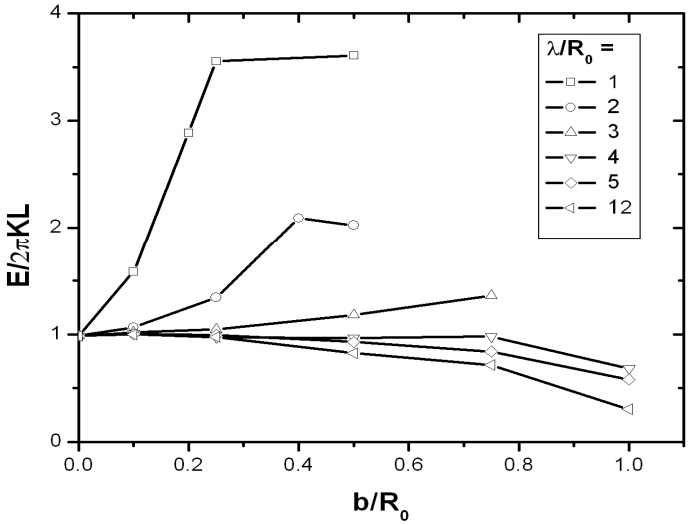

Fig. 4.16: Energy as a function of deformation amplitude *b* for dispersed nematic liquid crystalline filaments with perturbation wavelength λ; WR_0/K=1000.

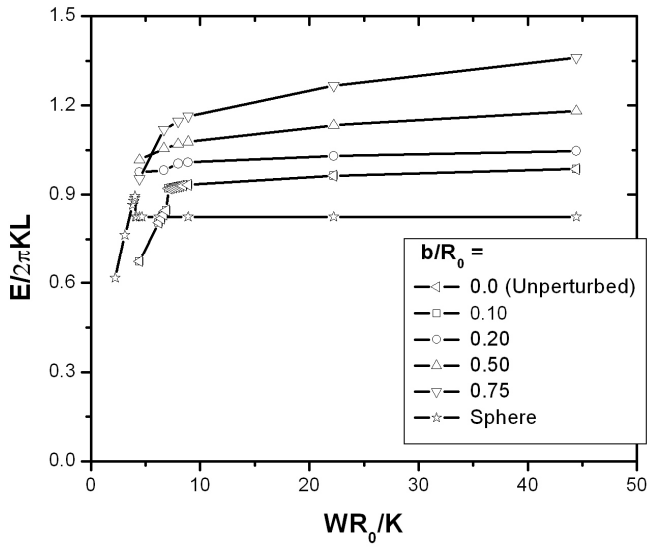

(a)

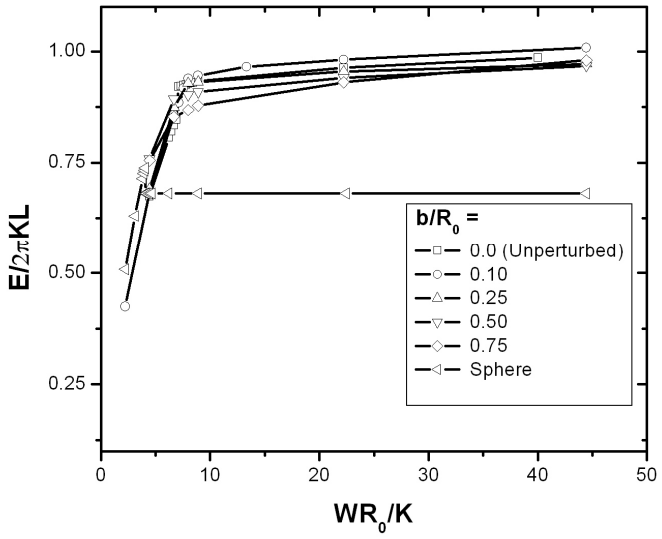

(b)

Fig. 4.17: Energy as a function of WR_0/K for dispersed nematic liquid crystalline filaments with perturbation amplitude b and wavelength (a) λ/R_0=3 and (b) λ/R_0 =4.

4.2.2 Morphological transition and energy barrier

The progression from a circular cylinder to breakup through a sequence of feasible minimum energy states requires a morphological transition from escaped-radial to radial; the latter is the morphology that exists in a sphere for strong anchoring and, as shown in Fig. 4.15c, is also the morphology for a sinusoidally perturbed cylinder with large wavelength and large perturbation amplitude. Figure 4.18 shows simulated optical micrographs of the transition pathway for $\lambda/R_0=5$ and $b/R_0=0.75$ as the Monte Carlo temperature is first increased and then decreased to permit the transition from a locally stable deformed escaped-radial structure to the minimum energy deformed radial structure. A singularity is generated at one end of the cycle, which then propagates to the center. The maximum energy barrier in this case corresponds to about 2400 J/m^3 [Fig. 4.19] for an equivalent droplet with a radius of 1μm, which is comparable to the maximum transition energy for a sphere. (When $b/R_0=0.5$, convergence to half ER and half PR [Fig. 4.18b] was obtained, although the equilibrium structure is radial.) We could not carry out the corresponding calculation from a radial orientation to an ER orientation because the system always went to a PPLD orientation, as discussed in Sec. 4.1.2.

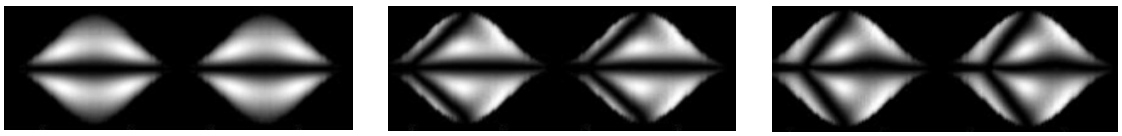

(a) (b) (c)

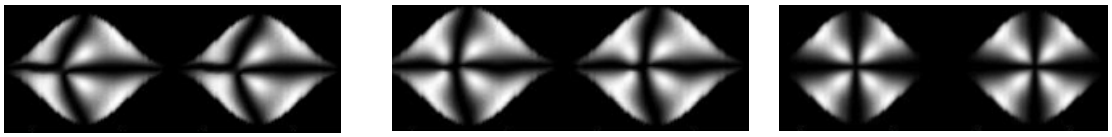

(d) (e) (f)

Fig. 4.18(a)-(f): Morphological transition in passing from a locally stable escaped-radial orientation to radial equilibrium orientation; λ/R_0=5, b/R_0=0.75.

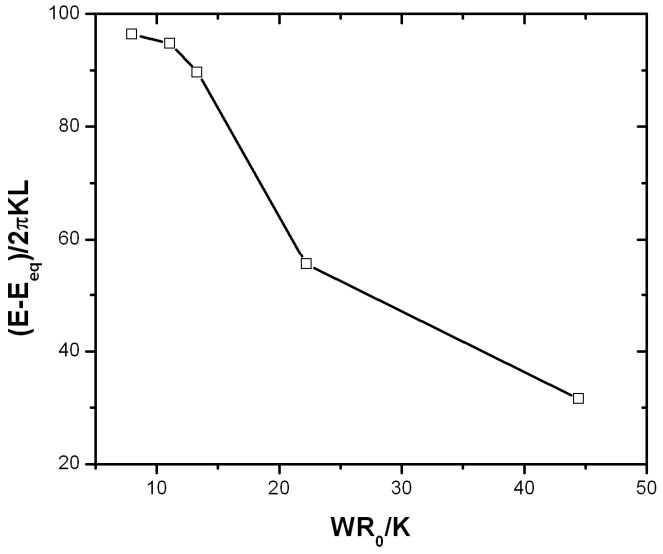

Fig. 4.19: Estimated energy barrier between cylinders and spheres as a function of WR_0/K.

4.3 Summary

There is a first order transformation in circular cylinders between planar-polar and escaped-radial configurations at a critical value of the parameter *WR/K* between 8.44 and 8.89, which is close to the analytical value of 8.65. With increasing perturbation amplitude there is a transition at long wavelengths to a deformed radial orientation, while at shorter wavelengths the dominant orientation is parallel to the cylinder axis except near the interface.

There are feasible paths with decreasing equilibrium free energies by which a nematic filament with strong homeotropic surface orientation can progress through a sequence of growing sinusoidal perturbations until it breaks up into nematic droplets. A morphological transition is required, however, in order to pass from the escaped radial orientation favored for cylinders to the radial orientation favored for strongly varicose distorted cylinders and spheres. The activation energy density for this transition is finite, and it is possible that progress towards breakup will be kinetically trapped in a varicose cylindrical shape without the possibility of breakup; in that case, breakup can only occur by raising the temperature sufficiently high to permit large orientational fluctuations, perhaps past the nematic-isotropic transition. Such varicose distortions on filaments were observed by Shaw [67] in a blend of a nematic polymer in an isotropic matrix, although direct comparison is not appropriate because the Oseen-Frank theory used here is not applicable to liquid crystalline polymers. This energy barrier may be related to the kinetic trapping of a dispersion of nematic 8CB in a gel state observed by Inn and Denn [32].

Chapter 5
Possible Future Work

Simulated annealing scheme is an effective computational scheme for calculating minimum free energy orientation distributions and transitions between local mimina in the energy landscape of liquid crystalline droplets. The following propositions can be made to continue the current thesis:

- Our approach allows free choice of the elastic constants in the Frank free energy expression; we have made the equal constants approximation to calculate the transitions and energy-barriers between locally stable states, however, since these calculations are computationally expensive. Although our calculations provide a feasible path through the conformation space for equal elastic constants, another path might exist that has a lower barrier with realistic values of the elastic constants. In order to obtain more realistic values for the energy barriers in liquid crystalline materials, simulations may be carried out with unequal constants appropriate to specific liquid crystals such as 5CB or 8CB.
- We studied nematic configurations in cylindrical filaments and the development of pathways by which a liquid crystalline cylinder might break up into droplets. Inn and Denn [32] made the same observation where both dispersed droplet morphologies and

gel-like morphologies were obtainable by introducing either thermal fluctuations or by providing a sufficient amount of mixing. Our thesis is limited to a transition from the gel-like state to dispersed droplets only and can be extended for reverse calculations.

- As discussed in Appendix A, our algorithm is valid only for small ratios of elastic constants. In order to use our simulated annealing scheme for large ratios of elastic constant- for liquid crystalline polymers, for example- the algorithm needs to be modified.
- In this thesis, we have assumed homeotropic anchoring at the droplet surface. The work can be extended for planar anchoring as well. Materials such as polyvinyl alcohol and glycerol provide parallel alignment at the droplet interface, and it may be interesting to determine whether or not liquid crystalline dispersions exhibit the same bistability with planar anchoring. One can also calculate the effect of various parameters, such as elastic constants, surface anchoring, and geometry on the droplet configuration.

Appendix A

Limitations of the algorithm (upper bound for the ratio of elastic constants)

In the absence of external fields or when there is no preferred molecular orientation at the surface, Ericksen [22] proposed that the elastic energy is a minimum (equals zero) when gradient of the director field is zero, i.e., $\nabla \mathbf{n} = 0$. When external fields are applied or the surface of the sample is given a special treatment, then the elastic energy always stays non-negative ($f \geq 0$ in Eq. 1.4). Ericksen derived the following inequalities for the Frank constants:

$$k_{11} \geq 0, \qquad k_{22} \geq 0, \qquad k_{33} \geq 0,$$

$$\text{and} \quad |k_{24}| \leq 2k_{22}, \qquad |k_{24}| \leq 2k_{11} \tag{A1}$$

To test our computational scheme for large ratios of the elastic constants (along with Eq. A1), we chose three sets of ratios of elastic constants: $k_{11}:k_{22}:k_{33}:k_{24} = 100:1:1:1$, $k_{11}:k_{22}:k_{33}:k_{24} = 1:100:1:1$ and $k_{11}:k_{22}:k_{33}:k_{24} = 1:1:100:1$, and carried out simulations with no anchoring at the surface. The results are shown in Figs. A1a, b and c: For the third set, where the bend constant k_{33} is the largest, we obtained a parallel orientation [Fig. A1c] and the system takes a non-negative total free energy. However, with the first two sets, where splay or twist constants are the largest, we obtained non-uniform orientations with negative energies [Figs. A1a and b]. These results are not in an agreement with the theory. We then performed three different simulations, where we chose only one non-zero elastic constant (splay, bend or twist), and we obtained the same kinds of results. These results were not acceptable, since Eq. 1.4 always results in a non-negative energy

if Eq. A1 is satisfied. Reducing the lattice size by a factor of up to 5 also did not produce physically meaningful results. We propose that since we have discretized the tensorial form of the elastic energy [Eq. 2.2] for our simulations, the discretization scheme may produce discontinuous patterns, although Eq. 2.2 is an algebraically equivalent form of Eq. 1.4. However, no pattern can have negative energy with only a non-zero bend constant, since the bend-constant term remains a square term even after the discretization, which is not the case with other three constants [Eq. 2.3]. Gruhn and Hess did not mention this problem in their work, and we believe it is a discretization issue.

In this thesis, we have implemented forward and backward differences to approximate derivatives in the energy expression. To find a solution to this computational problem, however, we tried central differences, but we were not successful for high ratios of the elastic constants. We carried out many simulations and found that our discretization scheme produces physically meaningful results up to the ratios of the elastic constants k_{11}:k_{22}:k_{33}:k_{24} = 6.0:0.51:1.31:3.5. Within these limits we observe uniform configurations with non-negative energies. Beyond these limits our scheme is not applicable. Since low molar mass liquid crystals have small ratios of elastic constants, however, our method is an elegant method to calculate the droplet configurations.

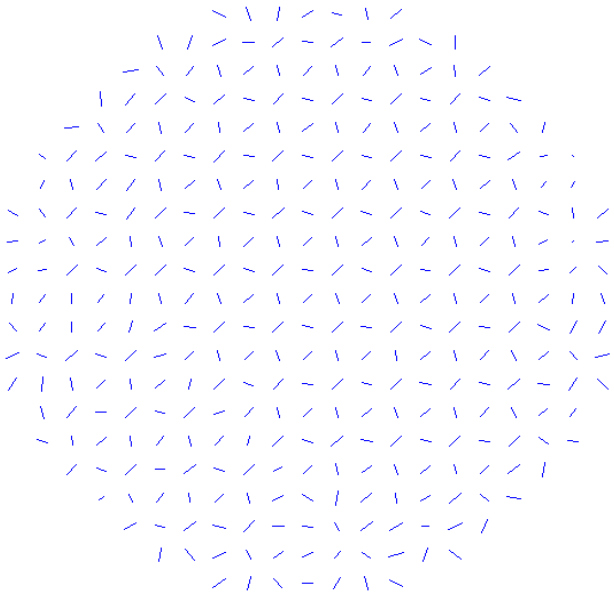

(a) k_{11}:k_{22}:k_{33}:k_{24} = 100:1:1:1; Free energy negative

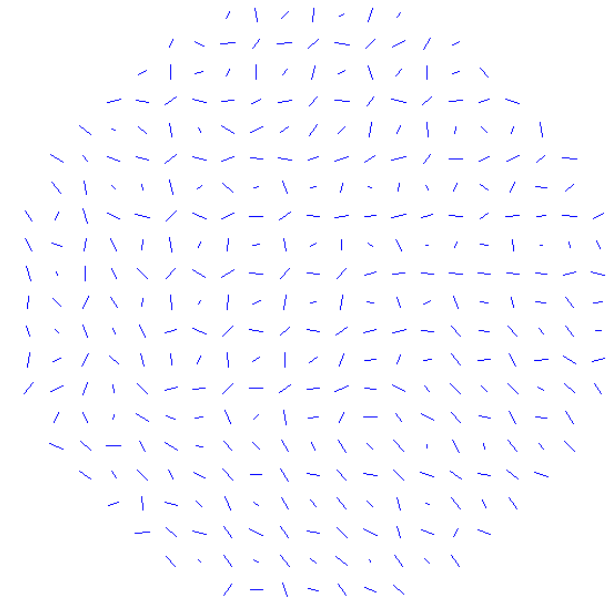

(b) k_{11}:k_{22}:k_{33}:k_{24} = 1:100:1:1; Free energy negative

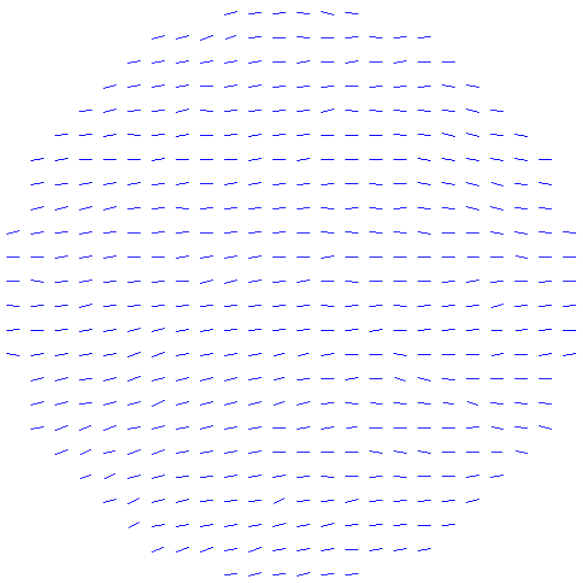

(c) k_{11}:k_{22}:k_{33}:k_{24} = 1:1:100:1; Free energy non-negative

Fig. A1 (a)-(c): Droplet configurations and energies with large ratios of elastic constants.

Appendix B

Importance of lattice dimensions

As discussed in Chapter 2, the continuum theory is applicable only at length scales larger than the molecular length, while there is a direct dependence of the scaled temperature on the size of lattice: $T^* = \frac{k_B T}{Kl}$ [Eq. 2.22b]. Thus, the question of the size of the cells becomes important. If the Monte Carlo temperature is zero, the results are in the continuum limit and changing the lattice size should not affect the calculations. However, if the Monte Carlo temperature is not zero, then the simulations will include the effect of thermal fluctuations. Alternatively, for a given temperature and mean elastic constant, increasing the scaled temperature corresponds to a decrease in the size of the unit cell. In another words, decreasing the lattice spacing implies an increase in thermal fluctuations. For a given value of the temperature and the mean elastic constant, there is a limiting value of the lattice cell above which the size of the lattice cell becomes comparable to the molecular dimension and continuum theory is no longer applicable. Moreover, since we are dealing with a discretization of derivatives in our computational method, we need to choose a system where we have a sufficient number of lattices to minimize the error associated with the discretization scheme. Hence, l is bounded from both above and below, and it is necessary to explore the regime for lattice sizes where our computational scheme is valid and efficient.

To study the effect of the lattice size on the elastic energy and orientation, we performed simulations for four different sets of spherical droplets with strong homeotropic anchoring condition at the surface. We chose the mean elastic constant

K=5x10^{-12}N and Monte Carlo temperature T=300K for our simulations and calculated the energy and radial order parameter $S_{\perp}$. It is apparent from Table B1 that at high values of lattice cell (order of 10μm), we get simulation results in a good agreement with continuum theory, and energy and order parameter remain essentially unchanged with the lattice size. Moreover, the simulated energy results are in agreement with analytical values. (The energies differ slightly since our simulations produce a radial orientation with an escape at the center, which is slightly less energetically expensive than the perfectly radial one.) When the lattice size is less than 1μm, then a decrease in the lattice spacing (thus a increase in T*) makes thermal effects more prominent and we obtain deviations between simulation results and continuum theory. We obtain different values for the energy for the same drop size with changing lattice size, but the radial order parameter is still almost constant [Table B2 and Table B3]. However, when we carried out simulations with very high values of T*, both energies and radial order parameters changed significantly by changing the lattice size [Table B4]. Here, we observe that E scales as $1/l^3$, since $N = \frac{4\pi R^3}{3l^3}$, the energy scales with the number of lattice cells N for a fixed size droplet. This suggests that the cell dimension is approaching the molecular length and continuum theory no longer holds. In fact, in this case the method can be used to study the nematic-isotropic phase transition in the same way as other molecular models do (Appendix C).

Table B1: Simulation results for different lattice sizes (drop size=150μm)

Lattice spacing, l (μm)	T^* (k_BT/Kl)	Simulated Elastic energy, $E/(4\pi KR)$	Radial order parameter, $S_\perp$	Theoretical energy/$(4\pi KR)$ (perfectly radial)
10.00	$8.28*10^{-5}$	0.9207	0.99400	1
5.55	$14.90*10^{-5}$	0.9839	0.99880	1
4.29	$19.33*10^{-5}$	1.0363	0.99790	1

Table B2: Simulation results for different lattice sizes (drop size=15μm)

Lattice spacing, l (μm)	T^* (k_BT/Kl)	Simulated Elastic energy, $E/(4\pi KR)$	Radial order parameter, $S_\perp$	Theoretical energy/$(4\pi KR)$ (perfectly radial)
1.000	$8.28*10^{-4}$	0.9655	0.99370	1
0.550	$14.90*10^{-4}$	1.2547	0.99810	1
0.429	$19.33*10^{-4}$	1.6840	0.99690	1

Table B3: Simulation results for different lattice sizes (drop size=1.5μm)

Lattice spacing, l (μm)	T^* (k_BT/Kl)	Simulated Elastic energy, $E/(4\pi KR)$	Radial order parameter, $S_\perp$	Theoretical energy/($4\pi KR$) (perfectly radial)
0.1000	$8.28*10^{-3}$	1.4233	0.98960	1
0.0550	$14.90*10^{-3}$	4.0234	0.98900	1
0.0429	$19.33*10^{-3}$	8.2615	0.98430	1

Table B4: Simulation results for different lattice sizes (drop size=0.15μm)

Lattice spacing, l (μm)	T^* (k_BT/Kl)	Simulated Elastic energy, $E/(4\pi KR)$	Radial order parameter, $S_\perp$	Theoretical energy/($4\pi KR$) (perfectly radial)
0.01000	0.08	6.1593	0.9457	1
0.00550	0.15	35.9419	0.8914	1
0.00429	0.19	81.7683	0.8430	1

Appendix C

Nematic-Isotropic phase transition study

To examine the effect of thermal fluctuations in the continuum model, we performed simulations with a lattice size close to the molecular length in the equal elastic constants energy expression and compared the results to those obtained by the *LL* molecular model. We carried out simulations with no anchoring at the surface and calculated scaled energy E_b^*, heat capacity C_v^*, and parallel order parameter $S_{||}$ as a function of scaled temperatures T^* (Sec. 2.7). Figure C1 shows a plot of E_b^*; energy changes continuously with T^*, however, a sharp change in the slope in observed. This discontinuous change in the slope suggests the onset of a first order N-I phase transition. From the plot of the heat capacity C_v^* [Fig C2], we identify the transition temperature $T_{NI}^* = 0.373$. The transition temperature corresponds to the maximum in the heat capacity curve.

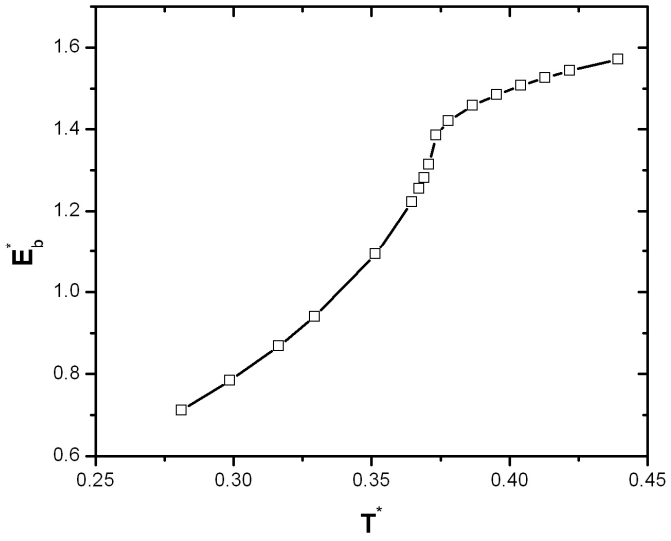

Fig. C1: Scaled energy E_b^* as a function of T^* for a droplet with N=179944.

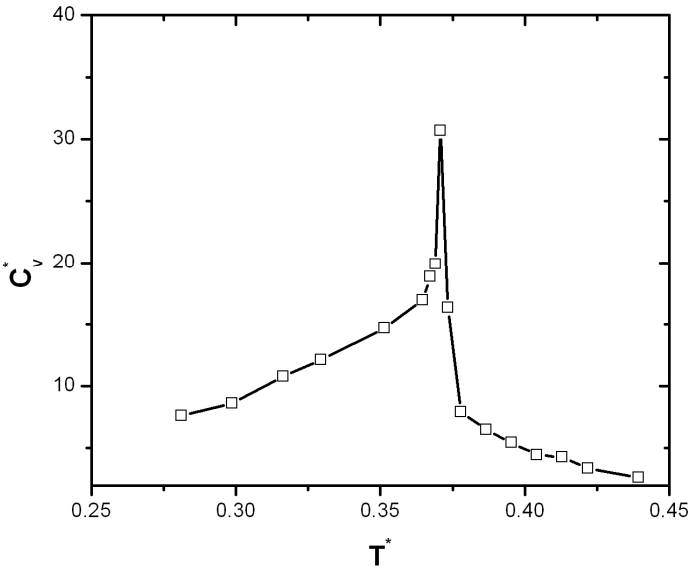

Fig. C2: Scaled heat capacity C_v^* as a function of T^* for a droplet with N=179944.

The behavior of the parallel order parameter $S_{||}$ as a function of T^* for different droplet systems is shown in Fig C3. The order parameter curves are continuous, although quite abruptly changing across the region near T^*=0.37. This accords with the first order

characteristic of the nematic-isotropic phase transition and suggests a transition temperature T_{NI}^{*}=0.373. Fabbri and Zannoni [40] obtained a transition temperature value T^{*}=1.123 using the *LL* model. (Which is three times that of our result). The difference between our results and the *LL* model arises because of the difference in the energy expression; The *LL* potential is $U_{ij} = -\varepsilon_{ij}\left(\frac{3}{2}\cos^2\theta_{ij} - \frac{1}{2}\right)$, while our energy expression is $E_{ij} = -Kl\left(\frac{1}{2}\cos^2\theta_{ij} - \frac{1}{2}\right)$ [Eq. 2.6]. If ε_{ij} is equal to Kl then the energy expressions differ by a factor of 3.

Convergence with increasing number of cells (*N*) is clearly observed in Fig C3. We observe that the transition is sharper for large *N* values; this is because increasing the number of lattice cells will provide a better average for the order parameter, especially when fluctuations in the director orientation are high.

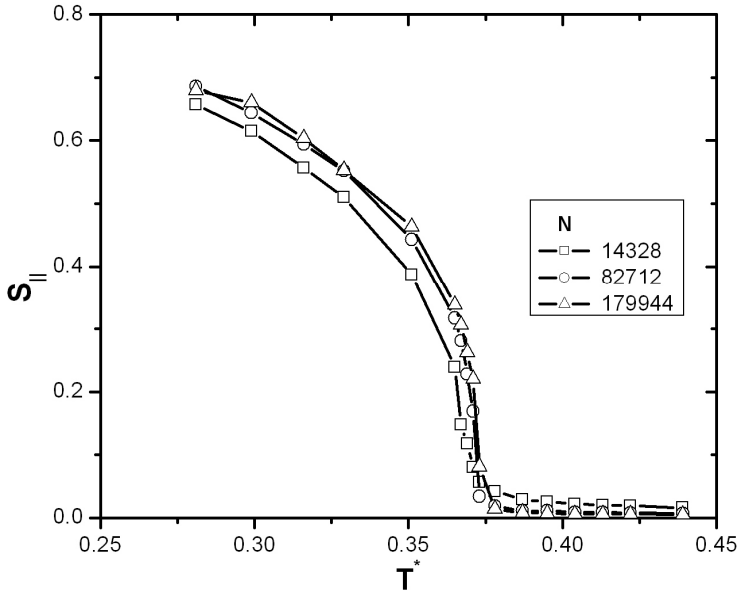

Fig. C3: Order parameter $S_{||}$ as a function of the scaled temperature T^{*}.

To study the correlation in orientation between directors, we calculated the pair correlation coefficient $G_2(r)$ at various scaled temperatures and plotted it as a function of separation r (Fig C4). The trivial starting point $G_2(0)=1$ is not shown in the plot for clarity purposes. We observe that in the nematic phase $G_2(r)$ starts from unity and tails off to the square of the order parameter ($S_{\|}^2$). Above the N-I transition, $G_2(r)$ decays to zero. We show the comparison of tail value of G_2 with $S_{\|}^2$ in Table C1. The results are in good agreement with Fabbri and Zannoni [40].

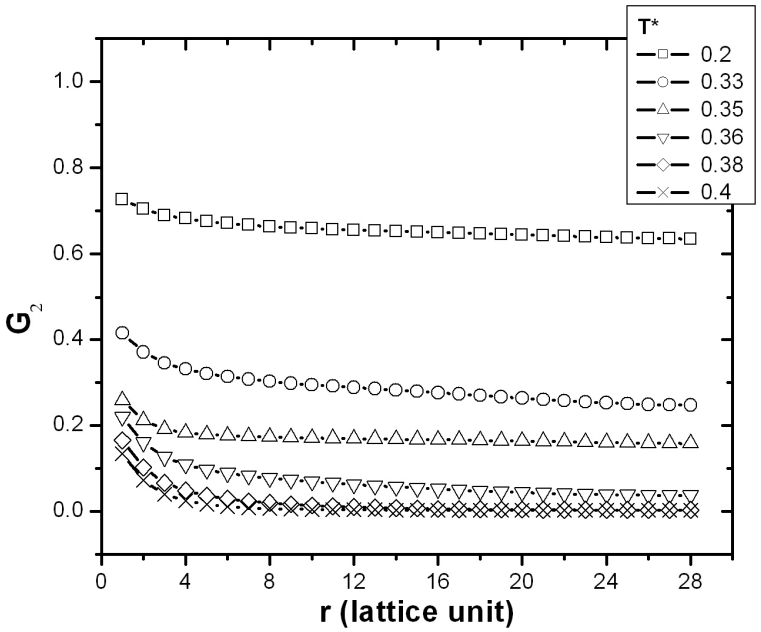

Fig C4: Correlation function $G_2(r)$ as a function of separation r (in lattice units) at various values of T^*.

Table C1: Comparison of tail values of G_2 with $S_{\|}^2$.

T^*	0.2	0.33	0.35	0.36	0.38
$S_{\|}^2$ obtained from simulation	0.648	0.260	0.152	0.050	0.002
Tail value of correlation function G_2	0.642	0.250	0.160	0.040	0.002

Fig C5a and b, respectively, display the equilibrium droplet orientation at temperatures below and above the N-I transition temperature. For a temperature in the nematic range (T^*=0.2), the droplet has a substantial amount of order and the directors try to arrange parallel to each other, while for an isotropic temperature (T^*=0.4) there is no order in the system.

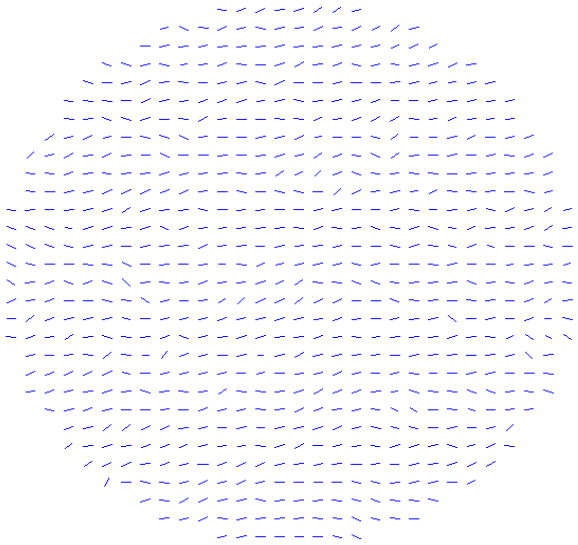

(a)

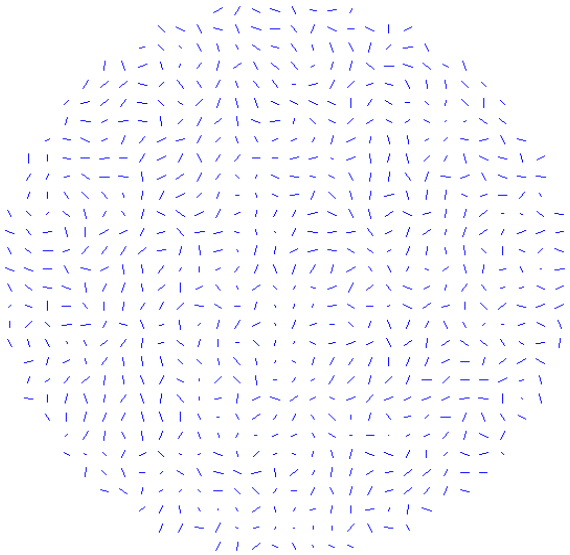

(b)

Fig C5: Director orientation with N=14328 at T^{*} = 0.2 (a) and 0.4 (b).

Appendix D

In the equal constants approximation, the total free energy of the system [Eq. 2.6] can be rewritten as

$$E = \frac{K\,l}{4} \sum_{\text{All lattices}} \sum_{\text{Six NN of i}} [1 - \cos^2 \theta_{ij}] + \frac{1}{2} \sum_{\text{Surface lattices}} W\,l^2 \sin^2 \varphi, \tag{D1}$$

which, because $l=R/R^*$, is equivalent to

$$E = \frac{KR}{4} \left\{ \frac{1}{R^*} \sum_{\text{All lattices}} \sum_{\text{Six NN of i}} \sin^2 \theta_{ij} \right\} + \frac{WR^2}{2} \left\{ \frac{1}{R^{*2}} \sum_{\text{Surface lattices}} \sin^2 \varphi \right\} \tag{D2}$$

where j is the nearest neighbor (*NN*) of i.

Now, we will prove that two bracketed quantities in the right hand side in Eq. D2 are constant.

For a perfectly radial orientation inside a sphere of radius R, the angle θ_{ij} between nearest neighbors i and j can be assumed to be small if the lattice cell containing the director is sufficiently far from the center of the sphere, i.e., $0 << r \le R$. Now, since $\theta_{ij} = \frac{l}{r}$, we can say that $\sin^2 \theta_{ij} \approx \frac{l^2}{r^2} = \frac{1}{r^{*2}}$, where r^* is the local linear radius with $N = \frac{4}{3}\pi R^{*3}$ [For a radial droplet the angle does not change along the radial direction, hence we assume that in a rectangular co-ordinate system only four out of six *NN* of i will

have $\theta_{ij} = \frac{l}{r}$, while rest two will take a zero value for θ_{ij}.]

Therefore $\sum_{\text{Six NN of i}} \sin^2\theta_{ij} = 4\sin^2\theta_{ij}$.

Now, we can write

$$\frac{1}{R^*}\sum_{\text{All lattices}}\ \sum_{\text{Six NN of i}} \sin^2\theta_{ij} \quad = \quad \frac{4}{R^*}\sum_{\text{All lattices}} \frac{1}{r^{*2}} \tag{D3}$$

The summation in Eq. D3 can be transformed into an integral over the total number of lattices (or R^*) in the following way:

$$\begin{aligned}\frac{1}{R^*}\sum_{\text{All lattices}}\ \sum_{\text{Six NN of i}} \sin^2\theta_{ij} \quad &= \frac{4}{R^*}\int_{R_x^*}^{R^*} \frac{1}{r^{*2}} 4\pi r^{*2}\, dr^* \\ &= 16\pi\left(1-\frac{R_c^*}{R^*}\right),\end{aligned} \tag{D4}$$

which is constant if $\frac{R_c^*}{R^*} << 1$. Here, R_c^* is the critical radius above which the assumption of small angle is valid. In fact the integral itself, multiplied with $KR/4$ [Eq. D2], gives the analytical expression for the energy for perfectly radial spherical droplets [Ref. Eq. 1.9a]. Similarly, for a perfectly uniform orientation (director orientation parallel to z-axis) inside a spherical droplet of radius R, the following calculations can be shown:

$$\begin{aligned}\frac{1}{R^{*2}} \quad \sum_{\text{Surface lattices}} \sin^2\varphi &= \frac{1}{R^{*2}}\int_{\varphi=0}^{\varphi=\pi} \sin^2\varphi\ \ 2\pi R^{*2}\sin\varphi\ \ d\varphi \\ &= \frac{8}{3}\pi,\end{aligned} \tag{D5}$$

which is a constant and, after being multiplied with $WR^2/2$ [Eq. D2], simplifies to the analytical energy expression for uniform droplets [Ref. Eq. 1.9b].

Thus Eq. D2) can be rewritten as

$$E = KR\left(\frac{C_1}{4} + \frac{WR}{K}.\frac{C_2}{2}\right), \tag{D6}$$

where C_1 and C_2 are constants. Thus, we observe that the only parameters are the product KR and the dimensionless group WR/K.

Bibliography

1. P. J. Collings, *Liquid Crystals, Nature's Delicate Phase of Matter,* IOP Publishing Ltd., England (1990).

2. S. Chandrasekhar, *Liquid Crystals,* Cambridge University Press, Cambridge (1992).

3. P. M. Chaikin and T. C. Lubensky, P*rinciples of Condensed Matter Physics,* Cambridge University Press, Cambridge (1995).

4. P.G. de Gennes and J. Prost, *The Physics of Liquid Crystals,* second edition, Oxford Science Publications, Clarendon Press, Oxford (1993).

5. P. S. Drzaic, *Liquid Crystal Dispersions,* World Scientific, Singapore (1995).

6. E. B. Priestley, P. Wojtowicz, and P. Sheng, *Introduction to Liquid Crystals,* second edition, Plenium Press, New York (1979).

7. A. M. Donald and A.H. Windle, *Liquid Crystalline Polymers,* Cambridge University Press, Cambridge (1992).

8. G. Friedel, *Ann. Physique.* **18**, 273 (1922).

9. T. Geelhaar, *Liq. Cryst.* **24**, 91-98 (1998).

10. C. W. Oseen, *Trans. Faraday Soc.* **29**, 883-900 (1933).

11. H. Zocher, *Trans. Faraday Soc.* **29**, 945 (1933).

12. F. C. Frank, *Disc. Faraday Soc.* **25**, 19-28 (1958).

13. R. D. Polak, G. P. Crawford, B. C. Kostival, J. W. Doane, and S. Žumer, *Phys. Rev. E* **49**, R978–R981 (1994).

14. H. Gruler, *Z. Naturforsch. A* **28**, 474 (1973).

15. P. P. Karat and N. V. Madhusudana, *Mol. Cryst. Liq. Cryst.* **36**, 51-64 (1976).

16. M. Kleman and O. D. Lavrentovich, *Soft Matter Physics,* Springer, New York (2003).

17. T. De'nève, M. Kleman, and P. Navard, *Liq. Cryst.* **18**, 67 (1995).

18. G. P. Crawford and S. Žumer, *Int. J. Modern Physics* **9**, 2469 (1995).

19. W. Maier and A. Saupe, *Z. Naturforsch. A* **15**, 815 (1960).

20. V. Frederiks and V. Zolina, *Trans. Faraday Soc*. **29**, 919 (1933).

21. R. Priest, *Mol. Cryst. Liq. Cryst.* **17**, 129 (1972).

22. J. L. Ericksen, *The physics of Fluids* **9**, 6, 1205-1207 (1966).

23. J. Nehring and A. Saupe, *J. Chem. Phys.* **54(1)**, 337{343 (1971).

24. N. Akino, F. Schmid, and M. P. Allen, *Phys. Rev. E* **63**, 041706 (2001).

25. A. Rapini and M. Papoular, *J. Phys. (Paris) Colloque* **30**, C4-54 (1969).

26. J. H. Erdmann, S. Žumer, and J. W. Doane, *Phys. Rev. Lett.* **64**, 1907–1910 (1990).

27. W. F. Brinkman and P.E. Cladis, *Physics Today* **35**, 48 (1982).

28. P. Candau, P. Le Roy, and F. Debeauvais, Mol. Cryst. Liq. Cryst. **23**, 283 (1973).

29. R. B. Meyer, *Phys.Rev.Lett*. **22**, 918 (1969).

30. M. Heppenstall-Butler, A. W. Williamson, and E. M. Terentjev, *Liq. Cryst.* **32,** 77 (2005).

31. T. Tixier, M. Heppenstall-Butler, and E. M. Terentjev, *Langmuir* **22**, 2365 (2006).

32. Y. W. Inn and M. M. Denn, *J. Rhology* **49**, 887 (2005).

33. P. K. Rai, M. M. Denn, and C. Maldarelli, *Langmuir* **19** (2003), p. 7370.

34. G. P. Crawford, D. W. Allender, and J. W. Doane, *Phys. Rev. A* **45**, 8693-8708 (1992).

35. M. P. Allen and D. J.Tildesley, *Computer Simulation of Liquids*, Clarendon Press, Oxford (1987).

36. A. Kilian and S. Hess, *Z. Naturforsch.* **44A**, 693 (1989).

37. J. Hobdell and A. H. Windle, *Liq. Cryst.* **23**, 157-173 (1999).

38. S. E. Bedford and A. H. Windle, *Liq. Cryst.* **15**, 31-63 (1993).

39. P. A. Lebwohl and G. Lasher, *Phys. Rev. A* **6**, 426 (1972).

40. U. Fabbri and C. Zannoni, *Mol. Phys.* **58**, 763 - 788 (1986).

41. C. Chiccoli, P. Pasini and C. Zannoni, *Physica A* **148A**, 298 - 311 (1988).

42. C. Chiccoli, P. Pasini, and F. Semeria, C. Zannoni, *Phys. Lett. A* **150**, 311-314 (1990).

43. C. Chiccoli, P. Pasini, F. Semeria, and C. Zannoni, *Mol. Cryst. Liq. Cryst.* **212**, 197-204 (1992).

44. C. Chiccoli, P. Pasini, E. Berggren, and C. Zannoni, *Mol. Cryst. Liq. Cryst.* **290**, 237 (1996).

45. J. Lu, H. Zhang, J. Ding, and Y. Yang, *Science in China B* **39**, 2(1996).

46. N.V. Priezjev and R.A. Pelcovits, *Phys. Rev. E* **63**, 062702 (2001).

47. E. Berggren, C. Zannoni, C. Chiccoli, P. Pasini, and F. Semeria, *Phys. Rev. E* **49**, 614-622 (1994).

48. T. Gruhn and S. Hess, *Z.Naturforsch* **51a**, 1-9 (1996).

49. P. J. Le Masurier, G.R. Luckhurst, and G. Saielli, *Liq. Cryst.* **28**, 769-778 (2001).

50. G. R. Luckhurst and S. Romano, *Liq. Cryst.* **26**, 871 (1999).

51. S. Kralj and S. Žumer, *Phys. Rev. A* **45**, 2461 (1992).

52. D. Frenkel and B. Smit, *Understanding Molecular Simulation*, Academic Press, New York (1996).

53. C. Zannoni, "Computer simulations," in *The Molecular Physics of Liquid Crystals*, ed. G.R.Luckhurst and G.W.Gray, Academic Press, New York (1979).

54. A. M. Smondyrev and R. A. Pelcovits, *Liq. Cryst*. **26**, 235-240 (1999).

55. S.V. Shiyanovskii, I.I. Smalyukh, and O.D. Lavrentovich, "Computer Simulations and Fluorescence Confocal Polarizing Microscopy of Structures in Cholesteric Liquid Crystals," *in Defects in Liquid Crystals: Computer Simulations, Theory and Experiment,* O.D. Lavrentovich, P. Pasini, C. Zannoni, S. Žumer, Eds., pp.229-270, Kluwer Academic Publishers: The Netherlands (2001).

56. R. Ondris-Crawford, E. P. Boyko, B. G. Wagner, J. H. Erdmann, S. Žumer, and J. W. Doane, *J. Appl. Phys*. **69**, 6380–6386 (1991).

57. F. Xu, H. S. Kitzerow, and P. P. Crooker, *Phys. Rev. A* **46**, 6535 (1992).

58. E. Berggren, C. Zannoni, C. Chiccoli, P. Pasini, and F. Semeria, *Phys. Rev. E* **50**, 2929-2939 (1994).

59. G. Fuller, *Optical Rheometry of Complex Fluids,* Oxford University Press, New York (1995).

60. S. Chandrasekhar, *Hydrodynamic and Hydromagnetic Stability,* Oxford University Press, London (1961).

61. S. Tomotika, *Proc. Roy. Soc. A* **150**, 322-337 (1935).

62. A. Rey, *J. Phys. II France* **7**, 1001-1011 (1997).

63. A. Cheong and A. Rey, *Continuum Mech. Thermodyn* **14**, 263-279 (2002).

64. A. Cheong, A. Rey, and P. Mather, *Phys. Rev. E* **64**, 041701 (2002).

65. A. M. Smondyrev and R. A. Pelcovits, *Liq. Cryst.* **26**, 235-240 (1999).

66. C. Chiccoli, P. Pasini, E. Berggren, and C. Zannoni, *Mol. Cryst. Liq. Cryst*. **290**, 237 (1996).

67. G. Rueda and M. T. Shaw, *SPE ANTEC Conf. Proc.* **37**:2005-7 (1991).